RICE UNIVERSITY

Environmental Response, Mechanisms, and Orientation of Diffusing Molecular Ions in Polyelectrolyte Thin Films

by

Carmen Geraldine Reznik

A THESIS SUBMITTED
IN PARTIAL FULFILMENT OF THE
REQUIREMENTS FOR THE DEGREE

Doctor of Philosophy

APPROVED, THESIS COMMITTEE:

Christy Landes, Norman Hackerman-Welch Young Investigator,
Assistant Professor of Chemistry

Anatoly Kolomeisky, Associate Professor of Chemistry and Associate Professor of Chemical and Biomolecular Engineering

Matteo Pasquali, Professor of Chemical and Biomolecular Engineering and Chemistry

B. Montgomery Pettitt , Adjunct Professor of Chemistry

HOUSTON, TEXAS

February, 2011

ABSTRACT

Environmental Response, Mechanisms, and Orientation
of Diffusing Molecular Ions in
Polyelectrolyte Thin Films

by

Carmen Reznik

New electrochemical storage and conversion materials hold promise as important additions to the world's energy supply, and the growing ability to control both sequestration and transfer of charge and matter via functionally responsive materials promises to transform the field. Already, new understanding of the role played by nano-scale morphology of materials in transport function has contributed to considerable material improvements, with functional polymers possessing specific chemistry and morphology playing a key role in the future of electrochemical material applications. However, many challenges to optimizing properties still exist due to incomplete descriptions of transport. In this work, fluorescence spectroscopy and single molecule spectroscopy experimental techniques and analysis are developed and employed to reveal details of the mechanisms underpinning ion transport in structurally ordered polyelectrolyte polymer-brush membranes. The studies reveal the existence and nature of heterogeneous transport mechanisms in these polymer films, and provide a description of the dynamic association of molecular ions with the brush. It is also shown that it is possible to tune charged ion transport characteristics in the thin films by controlling the solvent pH, with an effective switching of ion transport rates in these brushes past a threshold pH value. Additionally, Monte Carlo models designed to model molecular

scale interactions that give rise to experimental observables are developed to provide additional insight into the physical nature of transport processes in these materials. These models provide additional support for the conclusions of the experimental work.

This work is dedicated to my family, who embody the best: kindness, intelligence, humor, plain old fun, and best of all, love. Without them, I have nothing, and with them, I have everything. This work is a reflection of their support and unfailing confidence. Thank you Carter, Oliver, Jacob, Silas, and Dad. Thank you to all my family who are further afield as well.

And a special dedication to my Mother, who was strong, smart, and beautiful. I always knew I could do anything at all, because Mom and Dad never questioned it.

ACKNOWLEDGEMENTS

It has been a tremendous privilege to join Professor Christy Landes in her work in the challenging and rewarding field of Physical and BioPhysical Chemistry. Professor Landes' purposeful mentorship and leadership have been foundational in my development as a scientist. Professor Landes has always encouraged scientific independence and rigor, and is an exceptional model for these ideals. Moreover, I have had the privilege of working alongside Professor Landes at the start of her career. Even during this most busy of times, Professor Landes has shown unfailing dedication to those she leads, whether they are scientists or students in her classroom. Her tremendous example in mentorship, as well as in science, will always be a touch point for my own future career.

Additional thanks goes to Professor Edwin Carasquillo, an excellent teacher and mentor, for both scientific and personal guidance through the course of my academic endeavors; to Professor B. Montgomery Pettitt, also an outstanding teacher and scientist, for his considerable scientific mentoring; and to Professor Stephan Link, who has acted as a second advisor and advocate. Thank you!

I am also thankful for the first-rate scientists who surrounded me, with whom I could share ideas and the joy of science. These include all of my lab mates, particularly Charlisa Daniels, Qusai Darugar, and Alexei Tcherniak.

Also, thanks to my wonderful friends, who joined my family and stood in the (rather large) gap during the duration of this work, namely, Claire Mann and Jenny Frank. Where would I be without you?

And lastly, I acknowledge that fruitfulness is a blessing from God, who created both me and this astonishing and beautiful world I am privileged to study. It is my hope and prayer that the work of my hands be multiplied to the good things that God has most certainly planned.

TABLE OF CONTENTS

LIST OF FIGURES

LIST OF TABLES

LIST OF EQUATIONS

CHAPTER 1

INTRODUCTION

1.1 MOTIVATION

The ability to control the spatial and temporal distribution of mass and energy at the nanoscale drives a sea change in the world in which we live. A prevailing example of the dramatic effects this control already affords us is in the semiconductor industry, where the ability to sequester and direct electron transport on the nanoscale has provided the foundation for remarkable technological advancement.[1] Extension of this control by improving our ability to design yet more detailed nano-architectures on yet smaller scale, and to control the transport and spatial distribution of mass and light in addition to charge, promises transformation in a wide array of fields, including energy storage and delivery,[2-3] sensing,[4-5] communications,[6] and drug delivery.[7]

Innovation in the field of energy storage and conversion particularly, is recognized as a central world-wide need.[2] There is expectation that if the scientific and industrial community can realize significant gains in the performance of devices designed to efficiently collect, convert, and store energy from renewable sources, future energy scarcity pressures can be averted.[2-3] Projections with respect to world energy needs and supply are available from a number of sources. Figure 1.1 shows projections for world-wide energy demand through 2035, derived from values published by the U.S. Energy Information Administration. While timelines and numbers vary over the range of sources providing such projections, the trends are the same: world demand for energy continues

to increase dramatically. The projections shown here estimate a nearly 50% increase in consumption over current rates in the next 25 years.

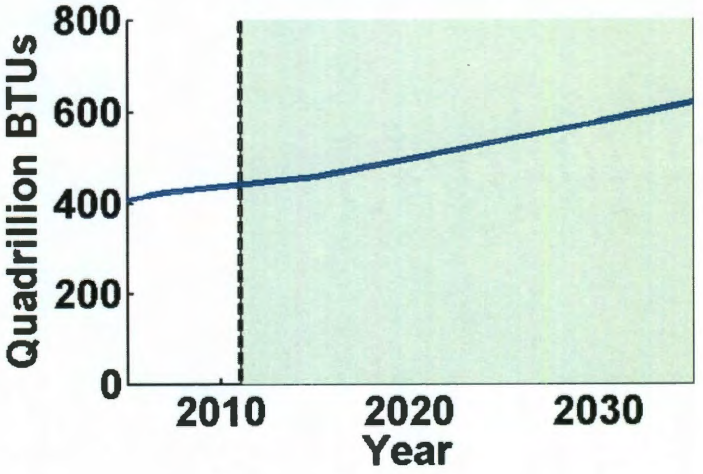

Figure 1.1: Projected world energy consumption, through 2035. Projected demand increases by ~50% over current demand. *Data obtained from U.S. Energy Information Administration Office of Integrated Analysis and Forecasting, U.S. Department of Energy.*

At the same time, there is general consensus that non-renewable energy sources that are currently the predominant source of energy driving our economies (Figure 1.2)[8] will become more difficult to find and access.[9] While the idea of a peak-oil model and

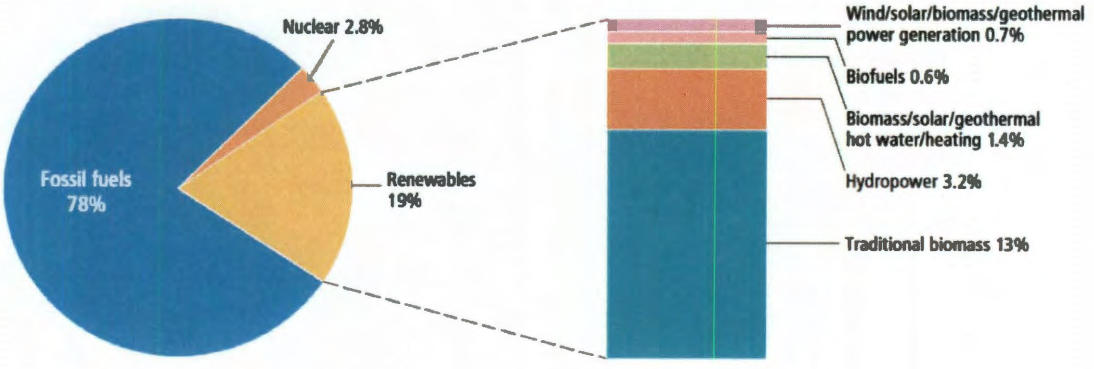

Figure 1.2: Profile of current energy sources. *Figure adapted from the Renewables 2010 Global Status Report, Renewable Energy Policy Network for the 21st Century*[8]

production time frame as proposed by Hubbert in 1959 is even more debated than estimates of future world energy consumption,[9-10] by definition, non-renewable resources are finite. Energy replacement will become an increasingly important concern.

An additional non-trivial consideration includes the significant impact that combustion based energy sources have on global climate,[11-12] along with the environmental impact associated with acquiring these energy sources. With respect to the environmental impact of acquiring fuels from reservoirs, coal mining may be considered the black sheep of the bunch, with extraordinary detrimental environmental consequences.[13-14] Although both technological and political interventions are being pursued to address climate impact in the context of combustion-based energy sources, growth of non-combustion based energy could promise a clean solution.

As will be discussed in detail in Chapter 2, recent advances in electrochemical storage and conversion technologies show compelling evidence that a combination of innovative materials and nanoscale architectures may provide a route to the significant improvements needed to make these technologies economical players in the energy industry. As yet, the evidence is promising, but substantial progress in performance is still required.

1.2 SPECIFIC AIMS

The goal of this work is to elucidate the fundamental, molecular level interactions and modes of transport underlying charged species transport in nano-structured, milieu-responsive polymer films that have an important role in the future of electrochemical conversion technologies. These films have the potential to provide efficient and clean

power from hydrogen sources. By providing deeper insight into the mechanisms by which molecular ions travel in these materials, and by contributing to advances in the analytical methods by which transport is evaluated, it is hoped that future material design efforts may be clearly focused on successful functional improvements.

Specific Aim 1

Combine the use of single molecule fluorescence spectroscopy techniques, including FCS and polarization resolved spectroscopy, in an investigation into molecular transport in polymer membranes with specific nano-scale ordering in their architecture. Using analytical and experimental advancements met through Specific Aim No 2, demonstrate the nature and extent of dynamic interactions between the brush membranes and charged molecular species, and explore the potential for switchable transport.

Specific Aim 2

Realize experimental improvements, and design improved apparatus and analytical procedures that promote deeper investigation into the properties of these systems. Define appropriate experimental procedures and analysis parameters for application of single molecule fluorescence techniques to heterogeneous thin-film systems.

Specific Aim 3

Utilize Monte Carlo based simulations to provide models of the experimental system that accurately describe observed transport characteristics, and provide insight into the physical basis for these observations.

1.3 OVERVIEW

Background with respect to the field of electrochemical storage and conversion is provided in Chapter 2, along with a description of the performance advantages associated with detailed molecular ordering in these kinds of materials. A review of recent advances in the design of materials with specific structurally based properties is included, along with a discussion regarding the contribution of single molecule fluorescence spectroscopy to the study of heterogeneous systems.

In Chapter 3, the chemical methods used for the work completed in this thesis are delineated. Due to the nature of the thin film system under investigation, there is particular focus on preparation and characterization of surfaces in this chapter. A discussion of confocal fluorescence scanning spectroscopy is provided in Chapter 4, along with details of the custom set-up utilized for these investigations.

The content of Chapter 5 presents work published in *Analytical Chemistry*[15] in 2009 that addresses important experimental and analytical parameters that impact analysis by Fluorescence Correlation Spectroscopy (FCS), which serves as one of the primary methods of analysis used in this work for determination of transport characteristics. The findings here quantify limits for several data analysis parameters inherent to FCS, and demonstrate the impact on accuracy of measured diffusion constants.

In Chapter 6, results from FCS studies on transport of fluorescent molecular ions within a poly(styrene sulfonate) polymer brush are reported. The work presented here was published in the *Journal of Physical Chemistry B* in 2008.[16] Transport rates are found to be pH dependent and switchable, and are also shown through random walk

Markov modeling to be determined predominantly by strong Coulomb interaction, rather than steric hindrance in this strongly charged and crowded environment.

By utilizing polarization resolved spectroscopy to monitor diffusive transport in the brush environment, heterogeneous modes of transport for these molecular ions are identified and characterized in Chapter 7. In addition, by evaluating the distribution of dwell-times for single molecules exhibiting either highly rotationally restricted motion, or rotationally averaged motion, kinetic rate constants for transition between strong and weak interacting states for molecular dyes are determined. The results of this work were published in 2009 in the *Journal of Physical Chemistry B.*[17]

In Chapter 8, a fluorescence detection scheme proposed in the literature that incorporates three single photon counting photodiodes to detect emission over three discrete polarization angles is utilized to determine spherical coordinates of transient molecular dipoles diffusing in the polymer brush thin film. The ability to discern the complete orientation of molecular dipoles, rather than only a projection of the 3D orientation onto a single x-y plane, allows identification of a global orientation preference for the diffusing probe molecules, and elucidates a mechanism of transport in the brush in which rotational and translational diffusion rates decouple, as evidenced by enhanced translation with respect to rotation. This work has been prepared for publication and is under review.

Chapter 9 contains the details of the Monte Carlo random walk simulations that were developed to provide a clearer picture of the physical mechanisms underpinning diffusive transport in the polymer brush matrix, and which support the conclusions of Chapters 6 and 8.

CHAPTER 2

BACKGROUND

The work presented in this thesis features investigation into the mechanisms underpinning molecular transport in ordered polymer membranes that have application to electrochemical energy storage and conversion, and to mass transport. The growing role of detailed structural and molecular ordering in design of these materials, and the potential for designing tunable materials that are responsive to environmental conditions, promises improvements to the fields of energy storage and delivery,[18] sensing,[19] and drug delivery.[7,20] While theoretical and experimental results have already demonstrated the potential for these materials, as discussed at greater length below, rational design of the next stage of materials with tailored dynamics requires detailed understanding of the heterogeneous processes contributing to observed charge and mass transport characteristics. To this end, concurrent development of sophisticated experimental techniques to provide this understanding is required. By incorporating a focus on identifying improved experimental analysis parameters, and fully developing proposed experimental methods in investigation of the dynamics of transport, the work of this thesis contributes to the basic understanding of transport mechanisms in these important materials.

2.1 Electrochemical storage and conversion

As briefly discussed in Chapter 1, there is significant interest in developing commercially viable electrochemical means to either generate useful forms of energy, or

to store energy and deliver it at useful times. This interest arises from the fact that these methods generate far less pollution than combustible energy sources[2,21] (sometimes none at all[22]), and enable collection and storage of energy from renewable sources like sun and wind.

The fundamental character of these methods lies in making use of the energy stored in chemical interaction. A familiar example of electrochemical storage and conversion is the faradic battery in which redox chemistry is responsible for generating electron flow (e.g. the lead-acid car battery). Some drawbacks exist with respect to faradic batteries, for which improvements are being sought.[23] For instance battery lifetime is limited due to irreversible side reactions, and structural stresses that occur upon charging and discharging, as is the speed at which charging and discharging can be executed.[3]

To complement existing technology, new functional forms of energy storage, release, and generation are being developed. An example is the electrochemical double layer capacitor (EDLC), for which function is based on storing electrostatic charge at the nano-scale interface of a high surface-area material via an electrical double layer. This kind of device is finding successful use in commercial aircraft[3] and a significant advantage of this design is inherently high specific power ratings (W/kg), which are indicative of high charge/discharge speeds.[24]

Utilizing the nano-scale interface concept of surface-mediated charge storage and delivery to improve specific power performance has been applied to redox-type chemical energy storage also, by structuring electrochemical capacitors such that redox reactions occur predominantly at or near the interface of high surface-area materials. Electrically

conducting polymers play a role in this version of surface area mediated charge storage and delivery.[25] It should be pointed out that the advantage of fast charge/discharge is also part disadvantage. As shown in Figure 2.1 high specific power ratings are related to low specific energy (J/kg) measures, which are an indicator of the duration of energy delivery. For this reason, hybrid devices in which both faradic and EDLC capacitive batteries are employed may provide the best answer to energy storage and delivery.[3]

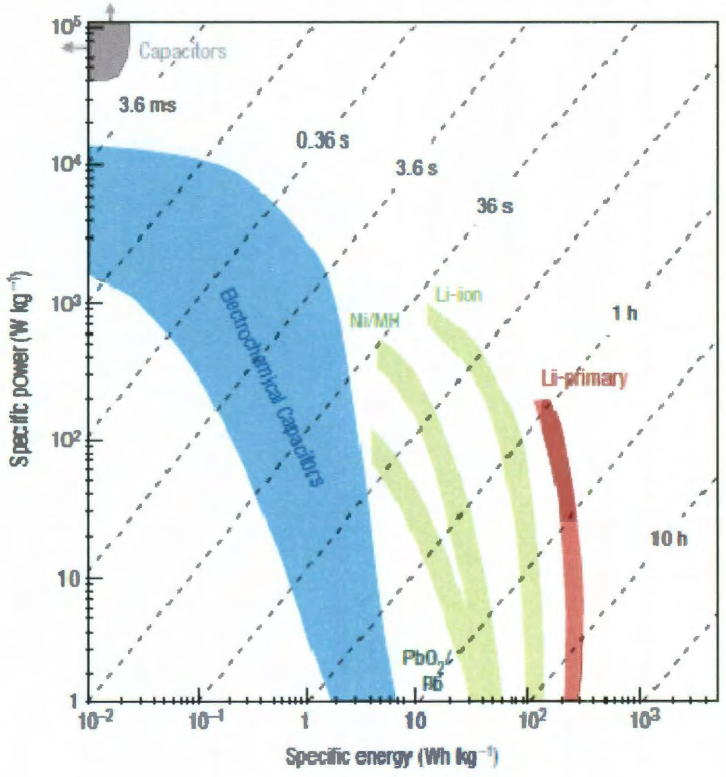

Figure 2.1: Specific power vs specific energy for various electrical energy storage devices. If a supercapacitor is used in an electric vehicle, the specific power shows how fast one can go, and the specific energy shows how far one can go on a single charge. Times shown are the time constants of the devices, obtained by dividing the energy density by the power.
Figure and caption reprinted by permission from Macmillan Publishers Ltd: Nature Materials,[3] copyright 2008.

With respect to electrochemical energy generation or conversion, fuel cell technology is attractive because of low maintenance requirements for these kinds of

devices, and the fact that fuel cells generate very low levels of pollutants. Fuel cell design is based on conversion of chemical energy into electrical current. To date, hydrogen fuel cells have proven to be commercially viable for some applications, and rely on hydrogen fuel, Pt catalyst, and a proton exchange membrane (PEM), typically Nafion (Dupont), a strong, fluorinated polyelectrolyte. Strong polyelectrolytes are characterized by complete ionic dissociation at low pH (e.g., for poly(styrene sulfonate), below a pH of 1). Figure 2.2 shows a schematic of a hydrogen fuel cell device, in which H_2 oxidation is catalyzed by Pt at an anode; resultant protons transit the proton exchange membrane to the cathode, and as a result, establish a flow of electrons through an external circuit; and then recombine at the cathode with O_2 to form water.

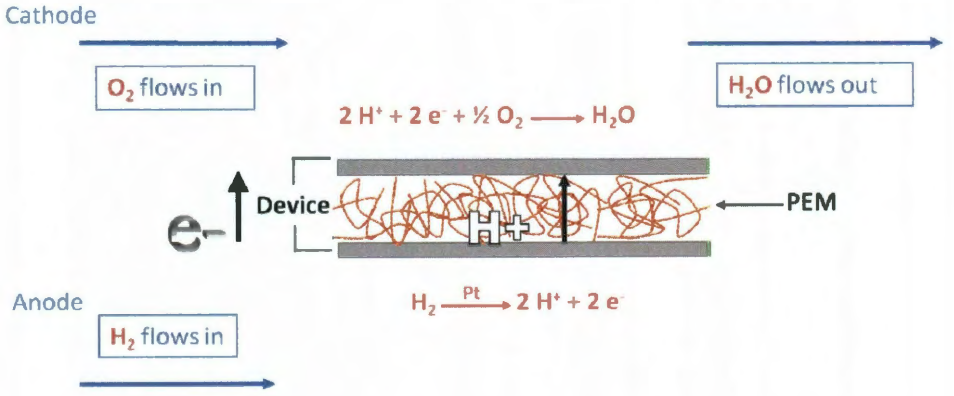

Figure 2.2: Schematic of hydrogen fuel cell design and operation.

A significant body of work has been focused on defining transport characteristics of protons within the PEM,[26-27] with evidence that local structural features of the membrane contribute to transport. Nafion is composed of a flexible hydrophobic fluorocarbon backbone and pendent hydrophilic side chains. In a 2006 article in

Advanced Functional Materials by Norsten *et.al,* the performance of a new PEM material designed to combine the rigid backbone characteristics of hydrocarbon based polyaromatic PEM materials, and the characteristics of fluorinated Nafion, is reported.[28] These show improved conductivity. The results from small angle X-Ray scattering experiments and supporting simulations[29] for Nafion's fluorocarbon material support the notion that naturally established structural order in the membrane, arising from phase separation of the hydrophilic and hydrophobic domains for these macromolecules, leads to creation of nanosized water channels through which proton transport occurs very efficiently. The rigid backbone and longer pendent side chains in the designed molecule by Norsten's group, help to form distinct aqueous regions. The chemical composition of the author's rigid polyaromatic fluorinated PEM is shown below in Figure 2.3, part a), with the composition of Nafion shown in part b).

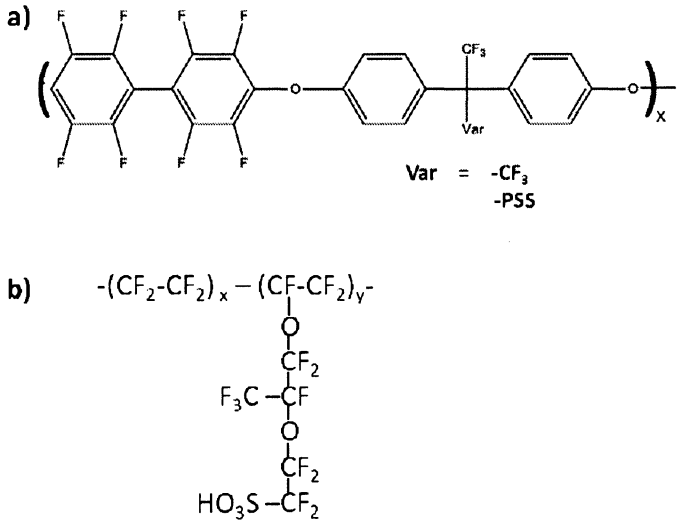

Figure 2.3: Chemical makeup of a) a rigid fluorocarbon based PEM material with long hydrophilic side chains composed of poly(styrene sulfonate), and b) Nafion, with a flexible fluorocarbon backbone.

The cost associated with production of the fluorinated Nafion PEM is still high,[30] limiting the wide use of fuel cells based on this proton exchange membrane. Additionally, there are some environmental concerns associated with PEM production, because of the reliance on Fluorine as a constituent.[30] As a result, alternative PEM materials with either better performance to help offset costs, or different chemical makeup to offset both cost and environmental concerns are being explored.[28,31-32] Alternative PEM materials tend to be less durable,[33] and frequently do not approach the performance characteristics of Nafion, however structural modifications to the materials, either via internal polymer cross-linking,[32] or co-production with various substrate matrices[18] have shown promising results.

2.2 The impact of nanoscale structure on transport

As touched on earlier, recent findings have demonstrated that movement of small molecules and charge through materials is heavily dependent on the molecular and nanoscale architectures extant in these materials. The presence of accessible active surfaces, molecular sized pores and channels, periodic structural features, and distinct molecular orientation all play a role in the rates and mechanisms of transport.[3,28,34-35] A number of recent examples highlight the importance of nanoscale architectures in transport dynamics. One example was published by Brauchle *et. al*, in which wide-field single molecule imaging techniques allowed observation of significant constraints imposed on diffusing molecules by varied host architectures of mesoporous materials,[36] with restricted rotational diffusion occurring in very small pore sizes.[37] Additional work by Granick, *et. al* demonstrates divergent diffusion behavior observed for colloidal

particles diffusing in constrained systems with specific bead radius to substrate size ratios.[35] With respect to proton transport, work by Jerker Widengren's group shows that structural features of biological membranes contribute to faster than expected diffusion of protons along membrane surfaces.[38]

Another study evaluated the diffusivity of both solvent and larger uncharged dye molecules in a swollen, amorphous polymer network of flexible, uncharged, nonpolar, poly(dimethyl siloxane) chains at different octane solvent concentrations and degree of crosslinking.[39] It was found for this system that diffusion of small solvent molecules is not influenced greatly by cross-links in the swollen systems, but that diffusion of larger dye molecules was dependent upon the extent of cross-linking in the polymer.

These and other observations with respect to structurally mediated processes driving charge and mass transport underlie the efforts to rationally design functional materials by using structural and chemical constructs that take advantage of detailed molecular ordering, interactions occurring at specifically designed interfaces, and selective molecular confinement.[3-4,34,40]

2.3 The role of polymer brushes and responsive surfaces

Polymer brushes are thin film membranes that possess nanoscale order. In Figure 2.4 are two representations of polymer thin films. In a), a typical isotropic thin film is depicted, and in b), a polymer brush is depicted. As illustrated, a polymer brush is a film in which polymer chains are end-grafted to the surface so that the chains tend to adopt a general orientation vector that is normal to the surface.[41] This is achieved by grafting the

polymer chains to the surface with the distance between grafting points on the substrate being much less than the radius of gyration of the polymer.

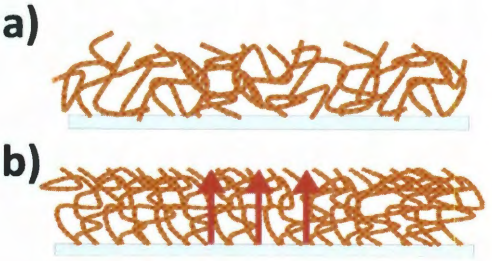

Figure 2.4: Polymer thin films: a) isotropic film, and b) polymer brush thin film. The arrows show the orientation of the polymer chains with respect to the surface.

Oriented polymer architecture generates interest with respect to transport occurring within and through these thin films for a number of reasons. One of the most intriguing findings comes from work done by Huck and his group out of Cambridge, that shows that orders of magnitude increase in charge transport efficiencies can be realized in strong polyelectrolyte brush films over anisotropic films.[42] Note that current fuel cell technology utilizes anisotropic films of Nafion. The Huck Group findings are another excellent indicator of the extent of influence that structural ordered imposes on material transport properties,[42] and of the potential for improved performance by incorporating such order.

Additionally, by combining design of chemical characteristics and the inherently ordered structure, structural and chemical properties of polymer brushes can be tailored to *respond* to various external stimuli such as temperature,[43] electric fields,[44] and ionic conditions of the solvent.[4,41] The responsiveness of both the brush architecture and functionality arises from swelling/shrinking of the polymer layer under good/bad solvent conditions.[41] This brush/solvent interplay can be manipulated by the physical means

listed above. As an example of the stimuli responsive functionality of polymer brushes, Liu *et al.* demonstrate pH switchable superhydrophobic adhesive/non-adhesive surfaces, for which a schematic is shown in Figure 2.5. This is achieved by combining engineered polymer brush chemistry with heterogeneous structural topography of the underlying substrate.[45] Transport of water droplets along the designed surfaces can be switched from a regime in which the droplets can slide across the surface at very low angles of < 15°, to a regime in which the droplets adhere even at surface angles of > 90°.

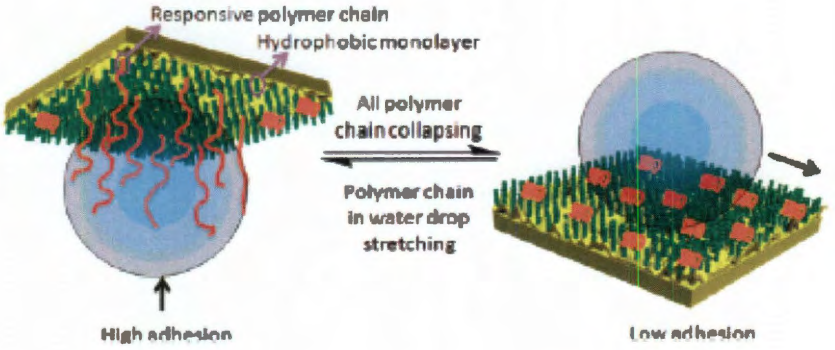

Figure 2.5: Demonstration of superhydrophilic/superhydrophobic surface transition based on pH switchable conformation of polymer brush architecture.
Figure reproduced with permission from Langmuir, 2010, American Chemical Society.

Because of the increased charge transport properties reported for strong polyelectrolyte brushes, and the indication that functionality can be switched on and off, the focus of this thesis has been on identifying physical modes of transport in these films, with the idea that deeper understanding will contribute to future design efforts that capitalize on structure and switchable functionality.

2.4 Single molecule rationale

The investigations herein were conducted using far-field fluorescence spectroscopy, and because the goal is to provide molecular-level insight into heterogeneous transport processes, studies were conducted in a single-molecule regime.

Traditional ensemble measurements report on average behaviors over many molecules, and this averaging can obscure the presence of multiple competing processes, often completely suppressing contributions from less dominant contributors.[46-47] In contrast, single molecule techniques provide an advantage, because chemical and kinetic information is compiled one molecule at a time and thus the full distribution of dynamics contributing to an ensemble of molecular behaviors becomes accessible.[46-51] This becomes a clear advantage when probing systems possessing heterogeneous environments or dynamics.

The number of single molecule investigations has increased dramatically since developing the ability to monitor single molecules at room temperature (~1995).[52] Examples of the systems and kinds of physical processes probed by single molecule spectroscopy are extensive. Conformations and conformational dynamics of proteins, DNA, RNA and polymers have been evaluated using single molecule FRET,[53-54] as well as have reaction rates.[54] Single molecule polarization resolved techniques have been used to evaluate orientational dynamics and preferences of molecules.[55-56] Single particle tracking has allowed evaluation of anomalous diffusion in heterogeneous biological[57] and synthetic materials.[35,37]

Because of the benefits for investigations into heterogeneous processes, the application of single molecule analytical methods to address the mechanistic bond-by-

bond progression underlying the functional properties of materials will play an important role in future informed-design efforts.

2.5 Spectroscopy

Evaluation of new classes of nano-materials in light of their attendant heterogeneity,[58-61] and refining the ability to direct and control their dynamic properties,[16,55,62] requires development of appropriate analytical methods. Far field spectroscopic techniques are attractive because they are non-invasive and can provide information about particle location, concentration, orientation, photo-physical and translational and rotational dynamics, conformation, and kinetics. In-depth treatment of fluorescence correlation spectroscopy (FCS) is provided in Chapter 5, and detailed discussion of polarization resolved spectroscopy is provided in Chapters 6 and 7, however a short summary of these methods is provided here.

2.5.1 Fluorescence correlation spectroscopy

FCS is based on correlation analysis of fluctuations in fluorescence intensity in a sub-femtoliter focal volume, that arise from diffusion of fluorescent entities into/out of the focal volume. By performing autocorrelation on a recorded fluorescence intensity trace, diffusion times, diffusion constants, and ultimately, molecule size or viscosity of the medium can be extracted.[63] Additionally, use of appropriate models for the correlation function can quantify passive and active transport,[64] adsorption,[65] and anomalous diffusion.[66] Furthermore, FCS is an attractive method for determining transport characteristics because the method can provide information about multiple

concurrent dynamic transport processes at once,[15] and in many cases, FCS can be utilized to probe processes in situ.[67-68]

By performing FCS, an averaging technique, in the single molecule regime, sampling of transport phenomena without significant chemical alteration of the environment is possible. Another advantage of FCS over methods such as dynamic light scattering, which can also provide diffusion constants, is that FCS is selective for fluorescence, eliminating background from signal arising from non-fluorescent entities in the sample.

The method has matured since its introduction in 1976, with novel adaptations in both optical and analytical techniques[15,65,68-75] to meet challenges inherent in application to increasingly heterogeneous systems. These adaptations have allowed increased understanding of and resolution of information garnered from materials exhibiting heterogeneity. FCS has been used extensively in biological systems,[67,76] and in the last several years, has seen increased use as a method to probe local internal transport conditions within specifically structured materials, polymer membranes, melts, and networks.[39,77]

As such, FCS is proving useful as a tool to evaluate the performance characteristics of new nanometer sized structures designed for specific functional purposes.[66,78-79] A nice recent example by De Santo, *et al.*, demonstrates the ability to observe and subsequently define laws governing the motion of molecules in structured materials by FCS.[66] The group employed FCS to address the effect on transport of nanoscale channels that approach the size of diffusing probe molecules in one dimension.[66] The authors evaluated the effect on diffusion for both flexible and non-

flexible molecules in the constrained environments, and found anomalous diffusion parameters are required to describe the diffusion of the large, flexible molecules through nanochannels of dimensions approaching that of the radius of gyration. They were able to show that under certain crowding conditions, the measured anomalous diffusion parameter approaches 0.5, which is descriptive of single-file diffusion of molecules through channels. As an example of the ability to extract information on heterogeneous processes, these authors also used an FCS fitting model that takes into account adsorption-desorption events. This allowed the group to evaluate the impact of the short range surface interactions that become significant in reduced dimensions, and evaluate the influence of molecular flexibility and channel wall interactions on the observed anomalous diffusion.

2.5.2 Polarization resolved spectroscopy

Polarization resolved spectroscopy provides a means by which to query molecular orientations and rotational diffusion characteristics. The photo-physical parameter that the method derives from is the polarization dependent absorption and emission of single fluorescent molecules.[80] Absorption of a photon by an individual molecule requires that the direction of polarization of the photon be matched to the direction of the molecular absorption dipole, with a $\cos^2\theta$ dependency on the angle between light polarization and absorption dipole orientation. The dipole direction is associated with the spatial oscillation of the molecular transition dipole. Likewise, emission of a photon is polarized along the direction of the emission dipole (see Figure 2.6).

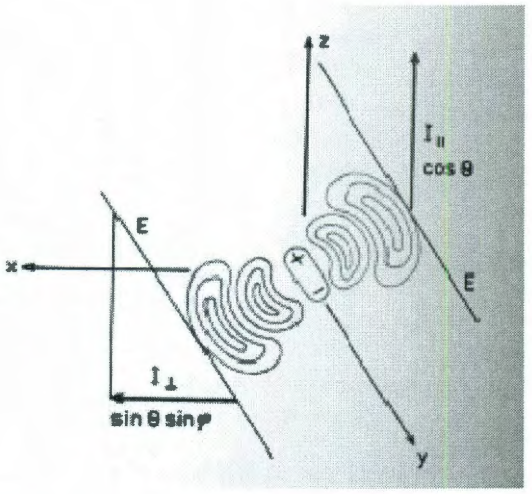

Figure 2.6: Emission dipole for an absorbing molecule, with associated fields. *Image reprinted from 'Principles of Fluorescence Spectroscopy, Third Edition,' Joseph R. Lakowicz, Springer, 2006.*

When the orientation of this oscillation revolves in space as a result of molecular reorientation, preferential absorption of certain linear polarized light directions, or preferential emission of particular linear polarized light directions can be monitored. As one example of the utility of this method, Schob, *et.al* have observed dynamic heterogeneity in reorientation rates in polymer thin films as the glass transition temperature of the polymer is approached.[81]

CHAPTER 3

CHEMICAL METHODS

As discussed in Chapter 2, the work of this thesis is predominantly concerned with transport and associated mechanisms of transport occurring in conjunction with supported polymer thin films. These thin films function as soft interfaces, and thus, surface preparation, chemistry, and characterization are important. These topics, as well as a description of the materials used for the spectroscopic techniques used herein are covered in the following sections.

3.1 Surface Chemistry

Preparation of polymer thin films was accomplished via two methods: Poly(styrene sulfonate) polymer brushes were prepared using surface initiated polymerization, and anisotropic PMMA thin films were prepared by spin coating.

3.1.1 Surface Preparation

The surfaces used for spectroscopic studies and surface characterization were No. 1 borosilicate coverslips (Fisher Scientific), and 1-1-1, p-boron, 10-20 ohm silicon wafers (SQI). Prior to use, all surfaces were rinsed thoroughly in Molecular Biology grade water (Thermo Scientific), dried in a N_2 stream, and plasma cleaned in oxygen plasma for 1 to 2 minutes. An additional step was introduced in surface preparation for brushes and PMMA thin films used for the studies detailed in Chapter 8. This consisted of washing in 80° C TL1 solution for two minutes[2] prior to rinsing in Molecular Biology grade H_2O. TL1 solution is composed of 1:1:6 NH_4OH:H_2O_2(30%):H_2O (molecular biology grade).

3.1.2 Polymer Brush Synthesis

Surfaces modified with PSS polymer brush were prepared from cleaned coverslips via surface initiated polymerization (SIP)[82-83]. SIP relies on polymerizing directly from a reactive monolayer covalently bound to a surface, and yields very high grafting densities in comparison to 'grafting to' techniques in which full-formed polymer chains are grafted to the surface[41,84]. Asymmetrically modified azo-iso-bisbutyronitrile (AIBN) (Figure 3.1), synthesized by collaborators in the Advincula laboratory at the University of Houston, was used as the initiator for polymerization[85]. AIBN covalently bonds to the borosilicate glass surface via the chlorosilane group to form the reactive monolayer.

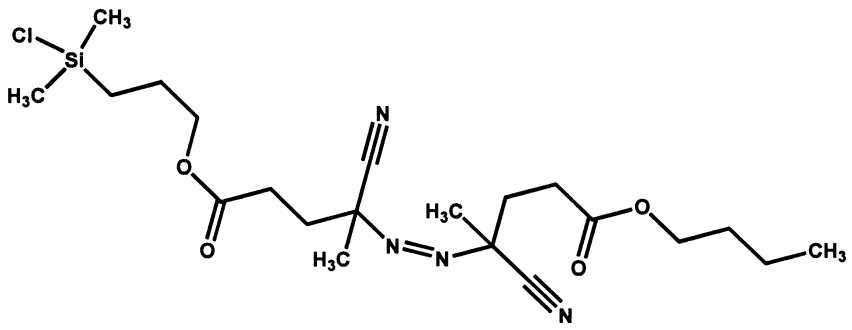

Figure 3.1: Chemical structure of asymmetrically modified azo-iso-bisbutyronitrile for surface initiated polymerization.

Binding of AIBN to the surface was achieved by dissolving 35 mg of AIBN in 15 mL of dry toluene with 150 μL of triethylamine added as a hydrocholoric acid scavenger, and then submerging coverslips in the solution for 24 to 48 hours. After treating the coverslips with the initiator, they were rinsed with MeOH and dried in a N_2 stream. Coverslips could be stored in MeOH if not used immediately.

Monomer solution, sodium 4-vinylbenzenesulfonate (Aldrich), (0.32 M) was prepared and degassed via a series of three freeze/pump/thaw cycles. Removal of dissolved oxygen is necessary because oxygen interferes with the polymerization reaction through termination of the free-radical process. AIBN modified coverslips were placed in an air-free schlenk flask (Chemglass) that was purged with N_2 and then evacuated. Degassed monomer solution was transferred to the coverslip chamber using a cannula to avoid exposure to air.

Polymerization was initiated at 63°C in a constant temperature oil bath. The polymerization reaction was allowed to proceed for 12-48 hours. After polymerization, the coverslips were removed and continuously rinsed with water for 12 hours in a soxhlet extractor to clean the brush matrix of free polymer. The chemical structure of the PSS brush is shown in Figure 3.2.a.

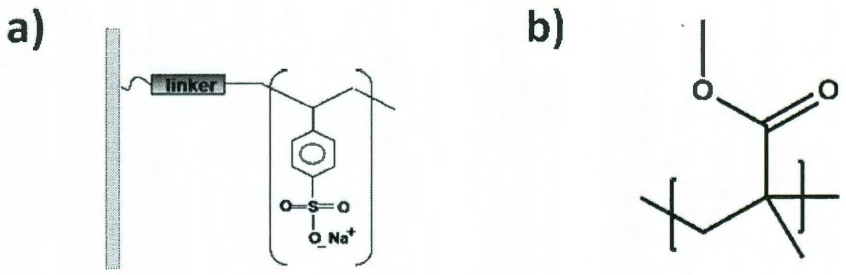

Figure 3.2: Chemical composition of a) poly(styrene sulfonate) polymer brushes, and b) poly(methylmethacrylate).

3.1.3 PMMA Thin Film Preparation

PMMA thin films were prepared from a concentrated solution of PMMA made of 10 g of PMMA (Acros) dissolved in 10 mL of dry toluene. This solution was allowed to

sit for two days by which time the PMMA was completely dissolved in solution. The PMMA solution was spin cast onto clean coverslips or cleaned silicon wafers with a single stage spin at 3000 RPM for 40 s.

R6G (in MeOH) was mixed into PMMA prior to spin casting at an approximate concentration of 100 pM.

3.2 Surface Characterization

Surfaces roughness, degree of coverage of the coatings, thickness of films, and fluorescence background levels were characterized using AFM, ellipsometry, and fluorescence spectroscopy techniques.

3.2.1 AFM and Ellipsometry

Shown in Figure 3.3 are 1 x 1 μm AFM images of two of the 4 batches of dry PSS modified coverslip surfaces and a clean coverslip substrate. Also shown, in b) is a line scan across a portion of the surface shown in part a). The average surface roughness is approximately 4 nm, with a maximum valley to peak variance of ~12 nm in a. In comparison, AFM of the blank coverslip shows an average surface roughness of approximately 3 Å, and a valley to peak variance of 10 Å for the same size region. The AFM surface scans showed complete coverage with polymer brush, with a qualitatively uniform coverage profile across multiple regions.

Ellipsometry data was acquired for each of the synthesis batches, assuming a refractive index of 1.59 for the PSS thin film. Silicon wafers were treated within the same synthesis batch as the coverslips for the ellipsometry measurements. Table 3.1

tabulates the associated surface rms roughness as determined via AFM, and the brush thickness via ellipsometry for the all of the brush batches studied.

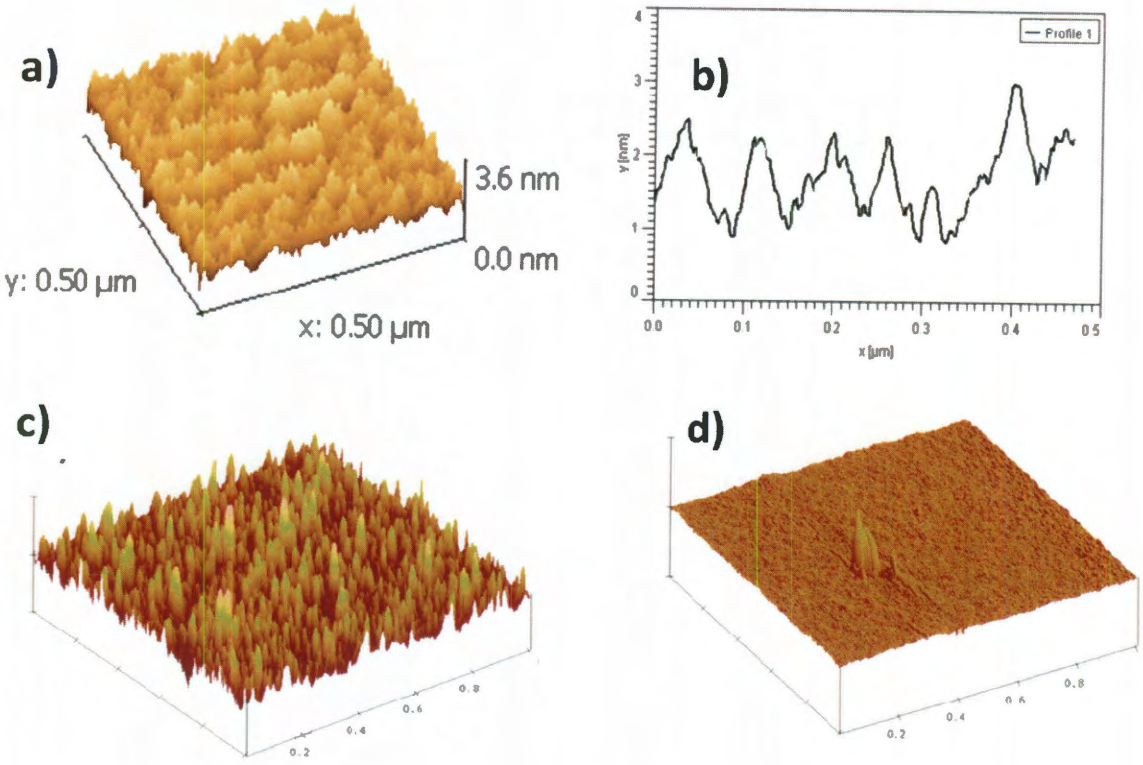

Figure 3.3: AFM of the surface of the polymer brush thin films: a) Brush batch 1 (Chapter 6), b) line scan across the surface of Brush batch 1, c) Brush batch 3 (Chapter 8, batch 1), d) clean glass surface. All images were acquired at 1 µm x1 µm in x and y, with 10 nm scale in z.

Synthesis batch	Surface roughness	Film Thickness
1	4.0 nm	49 nm ± 3 nm
2	2.1 nm	38 nm ± 4 nm
3	1.5 nm	5.1 ± 0.4 nm
4	1.6 nm	5.7 nm ± 0.5 nm

Table 3.1: Rms surface roughness and thickness as measured via ellipsometry for the polymer brushes used for these investigations. Batch 1 was investigated in Ch. 6, Bach 2 in Ch. 7, and Batches 3 and 4 in Ch. 8.

3.2.2 Confocal Fluorescence Scanning

A detailed discussion of confocal fluorescence scanning methodology is found in section 4.3. In this section, confocal fluorescence scanning is used to characterize the fluorescence character of a blank polymer brush surface (with water only), and a polymer brush with R6G dye included in solution. Scanned images of the surfaces for these two conditions are shown in Figure 3.4, a) and b) respectively. All scanning images were acquired from two detectors receiving orthogonally polarized components of emission light. The images shown in Figure 3.4 are taken from the 90° polarization detector.

These scans are taken over a 30 μm area at a power of ~ 700 W/cm^2. The intensity scale for the image labeled b) is ~ 3.5 times that in a). These scans demonstrate that the polymer brush surface is clean of fluorescent background from contamination or auto-fluorescence, and that dye can clearly be seen in the brush when loaded. Sequential imaging of the brush surface reveals that the bright fluorescence spots change from frame to frame, as expected for diffusing fluorescent entities (not shown).

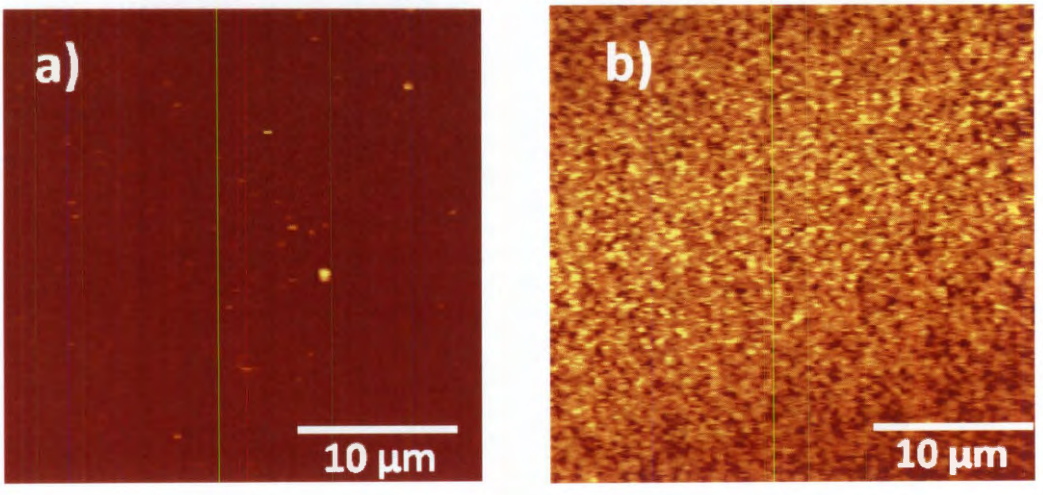

Figure 3.4: 30 μm x 30 μm scanning confocal images of the surface of polymer brush Batch 1. a) shows the surface with a water blank, and b) shows the surface with R6G loaded. The image in a) is scaled to an intensity of 70 kHz. The image in b) is scaled to 240 kHz.

3.3 Materials

Orange fluorescent carboxylate modified beads (Invitrogen), 100 nm, were used for calibrating the focal volume characteristics for the optical system. Rhodamine-6G (max abs/em: 530/549 nm), Figure 3.5.a,[86] diluted to ~ 100 pM in water, was used as a molecular probe of the diffusion environment (Invitrogen).

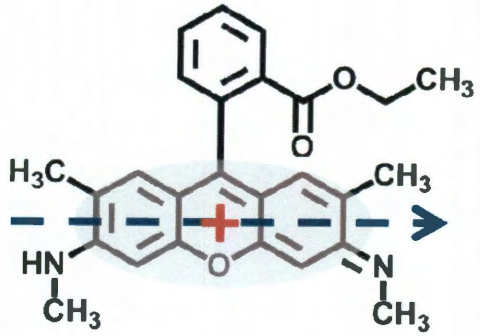

Figure 3.5: Chemical composition of R6G with orientation of emission dipole shown.

Sample chambers were constructed from squares of pliable silicone (Grace Biolabs) with a central cavity. Silicone squares were placed atop cleaned or sodium PSS treated coverslips, forming a leak-proof seal between the silicon and the glass. Solution containing R6G was placed within the central cavity and a second clean coverslip was placed over the filled chamber.

All pH adjusted solutions were prepared via dilution of spectroscopic grade H_2SO_4 into Molecular Biology grade water. Figure 3.6 shows R6G emission spectra as a function of solution pH. These emission spectra are corrected for the instrument response. R6G shows slightly reduced relative yield at lower pH, but no change in spectral position to indicate changes to structural features. At pH values greater than 10, the spectral position begins to blue-shift. All studies conducted herein were conducted at pH 7 or lower.

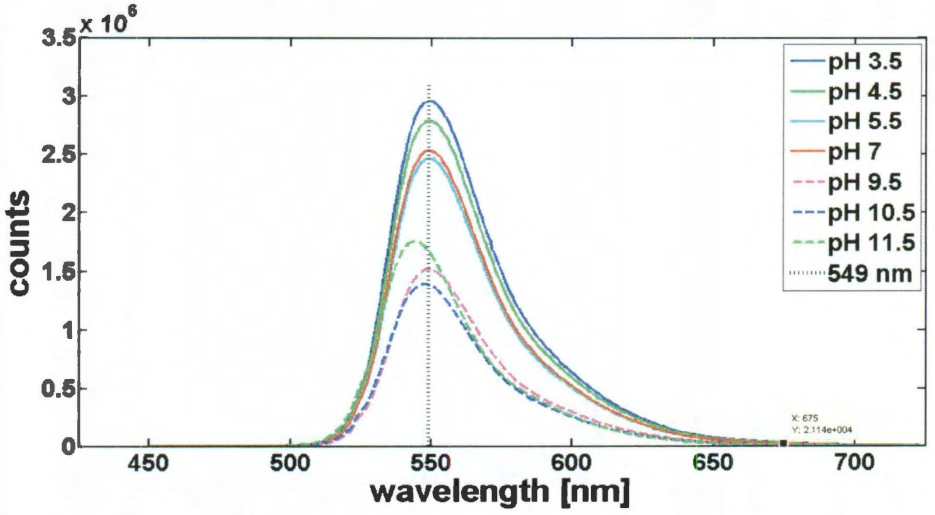

Figure 3.6: R6G spectra as a function of pH. For pH values of 3.5 to 9.5, the emission maxima are at 549 nm. At pH 10.5, the maximum has shifted to 548, and at pH 11.5, the maximum is shifted to 544 nm.

CHAPTER 4

EPIFLUOURESCENCE CONFOCAL SCANNING SPECTROSCOPY

4.1 Introduction

The primary methods of inquiry utilized for the work of this thesis involve fluorescence spectroscopy. Fluorescence spectroscopy is typically conducted on auto-fluorescent materials, materials labeled with fluorescent tags, or materials doped with fluorescent molecules[80]. For this line of investigation, fluorescent probe molecules were doped into the material we queried, and the characteristics of transport of these fluorescent probes were followed. All investigations herein were conducted using pico-molar concentrations of fluorescent dyes in the materials investigated. The low concentration of these fluorescent probes establishes conditions such that on average, only a single molecule is in the laser focal volume at a time. The use of sensitive single photon counting modules based on avalanche photodiode technology (SPCM-AQR, Perkin Elmer), makes it possible to detect the fluorescence from these individual molecules. The ability to use very low concentrations of fluorophore allows querying materials without affecting the materials properties by the presence of high levels of the probe molecule.

As discussed in Chapter 2, an important additional advantage of single molecule techniques is that recording information for one molecule at a time can uncover distributions of behaviors the molecules may exhibit. In a homogeneous material with simple processes, this does not provide an advantage. However, the case is much different for systems exhibiting heterogeneity. Recording single molecule behaviors and

building histograms of these behaviors can reveal the existence and nature of divergent processes, details of which are lost in the ensemble averaging inherent in traditional experimentation.

Generally, this chapter describes experimental parameters that are common to the techniques used in the following chapters. Further considerations regarding optical set-up that are specific to the studies detailed in later chapters are addressed in those chapters.

4.2 Confocal Epifluorescence Spectroscopy

For all experiments, I used home-built epifluorescence confocal scanning microscopes. A schematic for this equipment is provided in Figure 4.1. 532 nm solid state continuous wave lasers (VERDI, Coherent, and Compass 315M-100SL, Coherent) were used for sample excitation. Light was attenuated using neutral density filters (Thor

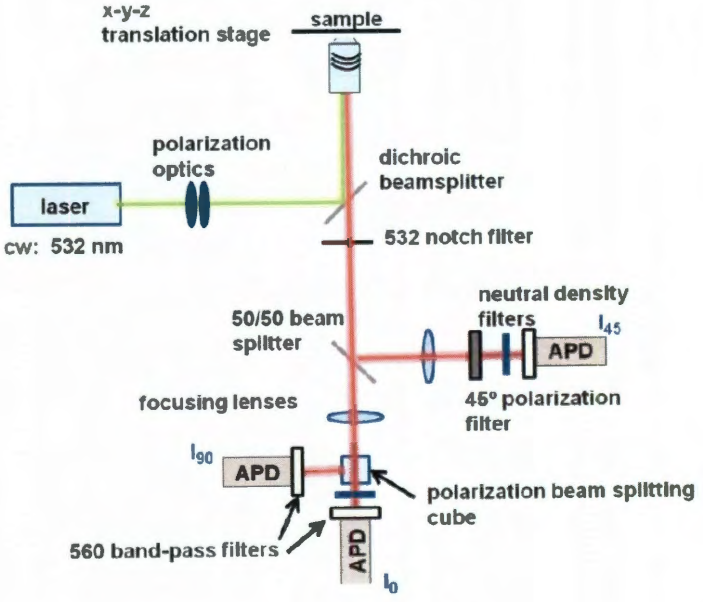

Figure 4.1: Homebuilt FCS/polarization microscope.

Labs), and circularly polarized via a polarizing filter (069-0120, 400-740 nm, Optosigma) and quarter wave plate (qwp0-532-05-04-R10, CVI laser).

Because derivation of expressions for the autocorrelation function in FCS assumes a Gaussian intensity profile for the propagating laser light, spatial profile cleaning of the excitation light was necessary to remove higher order transverse modes. Figure 4.2 shows the spatial profiles of six transverse intensity profile distributions for propagating laser light. These transverse electromagnetic (TEM) modes arise from the geometry of the laser resonator cavity. The fundamental TEM_{00} mode has a Guassian intensity profile, which is desired for excitation, while the higher order modes have a more complicated spatial arrangement[87]. Beam profile cleaning to remove these modes was achieved either within a Keplerian beam expansion path, by passing focused light through a 10 μm pin-hole, or by launching propagating laser light into a fiber optic.

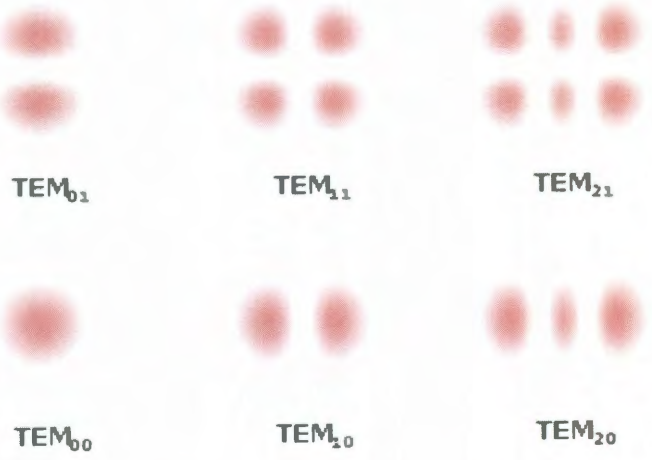

Figure 4.2: Transverse intensity distribution for six laser resonator modes. This figure was adapted from the Encyclopedia of Laser Physics and Technology web-site (downloaded 11-16-2010).

After profile cleaning, laser light was reflected at a dichroic mirror (z532rdc, Chroma Technology) to the microscope objective. To achieve a Gaussian beam profile at the focused laser volume within the sample along the z direction (the propagation direction of light) excitation light was expanded to overfill the back aperture[88] of a FLUAR 100x 1.45 or 1.3 NA oil immersion microscope objective (Carl Zeiss, GmBH). The profile of focused laser light along z is best fit by a Lorentzian function for underfilled conditions[89], however, Hess and Webb have shown that the focal volume profile for a high NA, overfilled optical set-up using a confocal pin-hole aperture is nearly Guassian in z over the $1/e^2$ intensity range, and has half length dimensions of ~ 1 μm which agrees with our estimated focal volume $1/e^2$ dimensions[88]. Our $1/e^2$ beam radius and ½ height were ~200 nm and ~1 μm, respectively. Power at the sample was maintained at ~ 75 W/cm^2 for FCS measurements and ~ 750 W/cm^2 for single molecule trajectories. Sample position in z is critical to accurate measurements when conducted on thin films,[90-91] and thus the stability of the sample position in z over the course of measurements was checked and recorded after every sample. In the event of focal drift, data was resampled.

In the detection pathway, fluorescence was collected and refocused by the same objective[92], and separated from excitation light via the dichroic mirror (z532rdc, Chroma Technology), and a notch filter (NHPF-532.0, Kaiser). Signal was then further directed through a detection pathway that was dependent upon the study. For both FCS and 2-D polarization resolved studies, light was refocused by an achromat focusing lens (achromat dblt, 026-1115, d25.4FL 69.93, 400-700, Optosigma), and passed through a polarizing beam splitting cube (PBSH-450-1300-050, CVI Laser) to two avalanche photon detectors

(SPCM-AQR-15, Perkin Elmer) operating in Geiger mode. This detection path leads to the I_o and I_{90} detectors shown in Figure 4.1, and did not pass through a 50/50 beam splitter. All detectors and focusing lenses were arranged to maintain 4F geometry[93]: the focusing lens was placed in the detection light beam path at 2x the 70 mm focal length of the lens, and all detectors were placed at a distance of 2x the focal length after the lens. This geometry images objects without resizing. For FCS studies, a 50 μm confocal pin-hole was placed at the first focal plane outside the microscope, prior to the notch filter.

For the 3-D polarization resolved studies discussed in Chapter 8, fluorescence emission was directed to a 50/50 beam splitter after the 532 notch filter. The split light on both paths was focused by achromat focusing lenses and passed through either a polarization filter (069-0120, 400-740 nm, Optosigma) set at 45°, or a polarization beam splitting cube (pbsh-450-1300-050, CVI laser), as shown in Figure 4.1. For these 3D studies, variable neutral density filters were used at the 0° and 45° detectors to equalize signal obtained from orange-fluorescent 100 nm polystyrene beads (Invitrogen), which have an isotropic polarization profile.

For all experiments, additional band-pass filters in the light path were utilized to improve signal-to-noise ratios (NHPF-532.0, Kaiser). TTL output from the detectors was augmented and split via a fan-out buffer (PRL-414B, Pulse Instruments) to two separate computer boards. One of the split signals was sent to a 2D imaging system (SPM 1000, RHK Technology). The other was sent to one of two photon counting boards for single photon counting trajectories. For FCS and 2D polarization measurements a Becker Hickel PMS-400-A board with two channel input and < 10 μs time resolution was used (Boston Electronics Corporation). For 3D polarization

measurements, a National Instruments 6602 counterboard combined with a National Instruments 2121 BNC unit with 1 ms time resolution was used. This unit allows acquisition of data over more than two input channels at once. A simple data collection program was written in LabVIEW to record the data acquired via the National Instruments equipment.

4.2 Scanning Confocal Imaging

For sample positioning over the focal volume, a closed-loop xyz piezo stage (P-517.3CL, Physik Instrumente) with 1 nm specificity was used and controlled by an SPM 1000 (RHK Technology). The SPM 1000 allowed raster scanning of sample areas as large as 100 μm over the laser focal volume, with consequent fluorescent imaging of the surfaces. Figure 4.3 shows an example of an image from a scan of a fluorescent 100 nm polystyrene bead drop cast on the surface of a cleaned coverslip. Imaging of these beads was conducted daily as a quality control measure to monitor the point spread function of the microscope. With the confocal pin hole, the bead image dimensions were ~ 390 nm in diameter (1.7*FWHM).

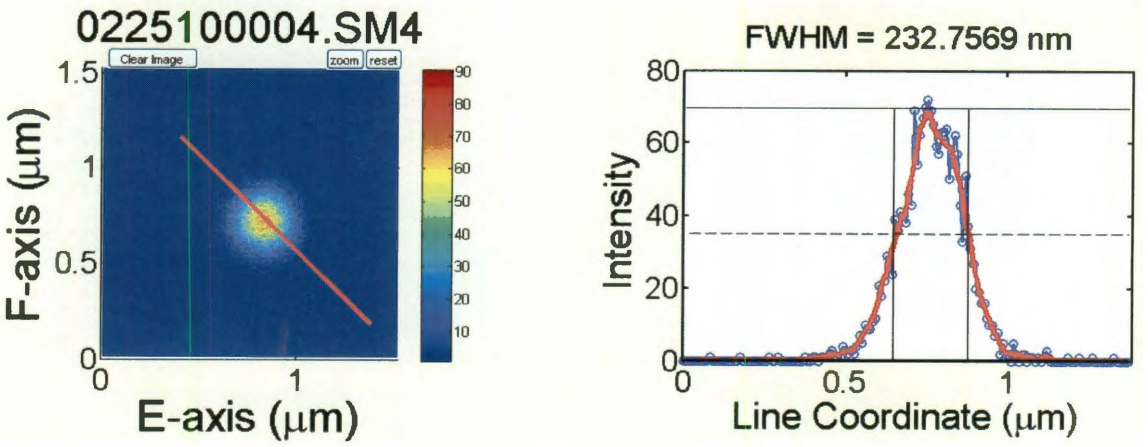

Figure 4.3: Confocal scanning image of 100 nm polystyrene bead standard, drop cast on a glass coverslip.

For an ideal, diffraction limited, optical set-up, the size of the diffraction limited spot, d, is equal to $\lambda/(2\eta\sin\alpha)$. Here, λ is the wavelength of light, η is the refractive index of the medium, and α is the angle over which the objective collects light. The numerical aperture of the objective is equal to the quantity $\eta\sin\alpha$, which is 1.3 for the bead scans shown in Figure 4.3. For our system, this fundamental limit in spatial resolution, then, is equal to 205 nm.

CHAPTER 5

FLUORESCENCE CORRELATION SPECTROSCOPY: CRITERIA FOR ANALYSIS IN MULTI-SPECIES SYSTEMS*

5.1 Abstract

This work evaluates the effect of varying three key parameters critical to accurate analysis by Fluorescence Correlation Spectroscopy, first in the context of a one species/one environment system, and then in a system composed of two species, or conversely, two environments. Experimentally appropriate settings for the 1) minimum lag time, 2) maximum lag time, and 3) averaging times over which an autocorrelation is carried out, as a function of expected diffusion decay time for a particular solute, are established in the published work. It is shown that use of appropriate settings plays a critical role in recovering accurate and reliable decay times and resulting diffusion constants. Both experimental and simulated data were used to show that for a binary system, in order to extract accurate diffusion constants for both species, decay times must be bounded by adequate minimum and maximum lag times as dictated by the fast and slow diffusing species respectively. It is also demonstrated that even when constraints on experimental conditions do not permit achieving the necessary lag time limits for both of the species in a binary system, the accuracy of the recovered diffusion constant for the one species whose autocorrelation function is fully time resolved is unaffected by uncertainty in fitting introduced by the presence of the second species.

*Contents from this chapter have been published in the following journal article: Tcherniak, A., Reznik, C., Link, S., Landes, C.F. Fluorescence correlation spectroscopy: Criteria for analysis in complex systems. *Analytical Chemistry.* 81, 746-754 (2009).
The first two authors contributed equally to the published work.

5.2 Introduction

Fluorescence Correlation Spectroscopy (FCS) is an important tool for measuring diffusion, transport, and dynamics in both homogeneous and heterogeneous systems, with its use to characterize transport in heterogeneous systems becoming increasingly important. This is witnessed by the use of FCS to probe diffusion conditions in a variety of media. In biological applications, this includes diffusion in the presence of crowded biological environments[94-95], at membrane interfaces,[91,96-97] and within confined cellular structures.[98] Outside of these biological applications of FCS, the technique has been used to profile flow characteristics in microchannel structures,[99-100] to evaluate diffusion in bulk and thin films,[16,101-103] and to characterize particle diffusion in highly constrained host environments.[35,37] Extracting an accurate description of the multiple dynamic processes occurring in these heterogeneous systems from an FCS experiment is not trivial. This is because the FCS experimental autocorrelation curve can be convoluted by a number of different optical and experimental conditions.[88,104-106] In addition, for a multi-species system, the relative diffusion rates contribute to the autocorrelation function, often over a wide range of time scales.

In spite of the challenges, FCS is an attractive method for monitoring the dynamics of diffusion and diffusion mediated processes because the method is selective for fluorescence, and can be applied to a wide range of physical systems in situ, at low volumes, and at low concentrations.[64,69] There exists an extensive body of literature covering FCS theory,[63,107] ideal optical parameters,[88,106] and appropriate experimental conditions.[104-105] Successful implementation of FCS requires attention to each of these arenas. And finally, accurate analysis of an experimental FCS autocorrelation curve

requires attention to several key parameters within the autocorrelation function itself.[15,108-110] This is particularly true with respect to analysis of systems with multiple diffusion processes. In the published work we show that even for a single species diffusing in a homogeneous environment, the autocorrelation function is dramatically affected by the choice of minimum and maximum lag-time limits, with direct effects on the accuracy of recovered diffusion coefficients.[15,110-111] Considering, then, a multi-species system, the development of an accurate treatment of multi-species fits with an eye on defining appropriate autocorrelation lag time regions is important.

In the *Analytical Chemistry* paper, we present systematic guidelines by which to define the appropriate limits for these parameters for a system composed of multiple diffusing species (or multiple diffusion environments).[15] We show that as a rule, minimum lag times (τ_{min}) need to be 2/3 or less the value of the shortest characteristic diffusion time. Maximum lag times, must be on the order of 5,000 times the longest characteristic diffusion time, before observed diffusion constants converge to expected values. Additionally, we show that in the single molecule regime it is necessary to establish a combination of chosen concentration and averaging time for each experimental system that is sufficient to recover an accurate diffusion constant. Each of these parameters is also evaluated and quantified for an experimental system composed of multiple diffusing species. To build a clear picture of multi-species autocorrelation performance, we also utilize a 3D random walk simulation to complement the experimental data. Using the experimental and simulated data, we also demonstrate the effect on ability to recover accurate diffusion constants for two diffusing species in the case when an autocorrelation function is not fully time resolved for the second species.

We establish that the accuracy of the recovered diffusion constant for the first, fully time-resolved, species is unaffected by the behavior of the autocorrelation function in the lag time region exhibiting decay due to the second species. This is true in spite of the uncertainty in fitting that arises in this lag time region.

As my thesis contribution, the following discussion covers the findings on the behavior of recovered diffusion constants as a function of particle size (solute viscosity) as minimum lag-times are varied for both a homogeneous and heterogeneous solution.[110-112]

5.3 Methods

5.3.1 Autocorrelation Analysis

Autocorrelation analysis of the fluctuations in intensity in a tightly focused laser volume, as per equation (5.1) below, provides information about characteristic diffusion rates, fast photophysics, photochemistry, and any extant chemical reactions:[64]

$$G(\tau) = \frac{\langle \delta F(t) \cdot \delta F(t+\tau) \rangle}{\langle F(t) \rangle^2} . \qquad (5.1)$$

Here, $\langle F(t) \rangle$ is the average of the fluorescence signal over time, and $\delta F(t)$ is the signal at time t, minus the average signal: $\delta F(t) = F(t) - \langle F(t) \rangle$.

Building on the work of Elson and Madge, who derived the analytical autocorrelation expression for 2-dimensional fluorophore diffusion within a focused laser spot (equation (5.2)), Aragon and Pecora derived the expression for an open detection volume with Gaussian intensity profile in x, y, and z, (equation (5.3)).[63,107]

$$G(\tau) = \frac{1}{V_{eff}\langle C\rangle} \cdot \frac{1}{\left(1 + \frac{\tau}{\tau_D}\right)} \tag{5.2}$$

$$G(\tau) = \frac{1}{V_{eff}\langle C\rangle} \cdot \frac{1}{\left(1 + \frac{\tau}{\tau_D}\right)} \cdot \frac{1}{\left(1 + \left(\frac{r_0}{z_0}\right)^2 \left(\frac{\tau}{\tau_D}\right)\right)^{1/2}} \cdot \tag{5.3}$$

In these equations, τ_D is the characteristic diffusion time for a species, and in the 3D expression, r_0 is the focal volume radius and z_0 is one half the distance along the optical axis. Both r_0 and z_0 are taken as the distance at which the intensity has fallen to $1/e^2$ times the maximum value. Diffusion time is related to the diffusion coefficient by the relation:[64]

$$\tau_D = r_0^2/4D \ . \tag{5.4}$$

Autocorrelation curves and the fits for the curves for diffusing fluorescent polystyrene bead samples of different diameter are show in Figure 5.1, along with a curve for R6G, a fluorescent molecular dye.

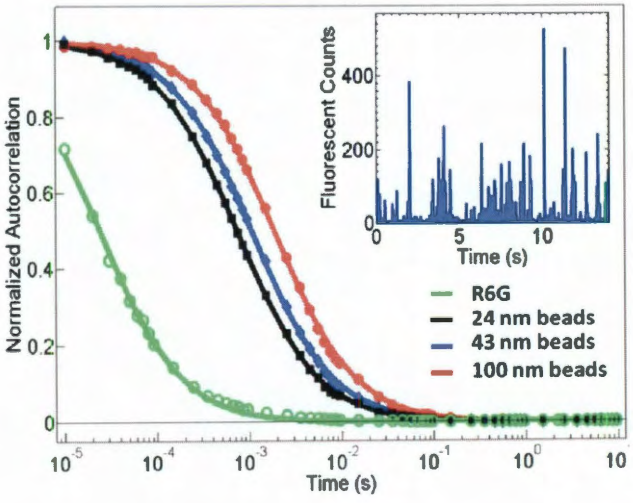

Figure 5.1: Autocorrelation curves for R6G, and 24, 43 and 100 nm polystyrene beads diffusing in water. The dots are the logarithmically binned data (discussion below), and the solid lines are fits to the data. Inset: Binned photon counting trajectory.

5.3.2 Correlation Parameters

FCS autocorrelation analysis can be performed using either hardware autocorrelator boards or by performing software autocorrelation analysis directly on fluorescence signal trajectories collected with a photon counting board. While hardware autocorrelation can reduce analysis time significantly,[108] software autocorrelation performed directly on fluorescence signal trajectories as in equation (5.1) allows for extensive data manipulation and provides the ability to make comparisons over the same exact data set while varying analysis parameters. Therefore we have used software autocorrelation throughout this paper. Additionally, in all cases, we choose to carry out autocorrelations over all possible lag times, rather than via a multi-tau algorithm.[108,113-114] This avoids introduction of additional analysis variables to our autocorrelation function that may arise from shifting lag time distributions. All analysis programs were written in Matlab (R2006a). Comparisons made by Gell *et al.* for autocorrelation analyses done by both software and hardware methods have demonstrated comparable performance in determining diffusion coefficients.[110]

All data were acquired with a minimum photon binning time of 10 μs. Signal trajectories were averaged over 5 minutes or more. Signal trajectories collected this way could be modified after acquisition using Matlab programs to bin photon counts further (for example, to 100 μs bin times and up). By this means, the minimum lag times were adjusted as noted in the following sections.

The autocorrelation functions for the minimum lag time studies were carried out on signal trajectories using equation (5.1), with a τ_{max} of 12 seconds. Multiple autocorrelation functions were averaged together to bring the total experiment time to

five minutes. These values for τ_{max} and total averaging time were established as sufficient for accurate analysis within the published work.

5.3.3 Data Fitting and Logarithmic Binning

The final averaged autocorrelation function was then subjected to a logarithmic binning algorithm, which averages all values within successive logarithmically defined decades. This results in a final autocorrelation curve that is composed of individual points that are logarithmically spaced. The final curve resembles an autocorrelation curve obtained using a multi-tau algorithm, however all lag times contribute to the curve. The primary affect of this binning algorithm is to equalize the relative data weights across the logarithmic decades for the subsequent fitting. The affects of logarithmic binning on curve fitting are discussed at more length below. All fitting was done post logarithmic binning via nonlinear least squares, using the Levenberg-Marquardt algorithm with data weighting as described by Wohland, *et al.*[108] This data weighting is achieved by calculating the standard deviation at each lag time for the individual autocorrelation curves that are ultimately averaged together, and sending this standard deviation vector to the Matlab fitting algorithm.

A comparison of fitting performance for 1) raw data, 2) weighted data, 3) logarithmically binned data, and 4) both logarithmically binned and weighted data is provided in Figure 5.2, where autocorrelation curves for 100 nm polystyrene beads and the various fits for these curves are shown. Autocorrelation functions for raw data (the solid black line), and logarithmically binned data are shown in part a) of Figure 5.2. Part b) shows that an un-weighted fit for the raw data deviates from the experimental autocorrelation function at short bin times (solid green line), while the fits made for raw

weighted data and logarithmically binned data coincide (solid black and red dots, respectively). Returned diffusion times were: 2.40 ms for raw data; 2.68 ms for weighted fits of raw data; 2.74 ms for logarithmically binned data ; and 2.79 ms for logarithmically binned and weighted data. There is less than 3% difference between values returned for weighted data and logarithmically binned data, while there is a 10% difference between fits of raw data and the weighted data. From this analysis, it is clear that logarithmic binning of the autocorrelation data provides an advantage in fitting the autocorrelation curves by providing a second means by which to equalize the data weight across the logarithmic lag time scale.

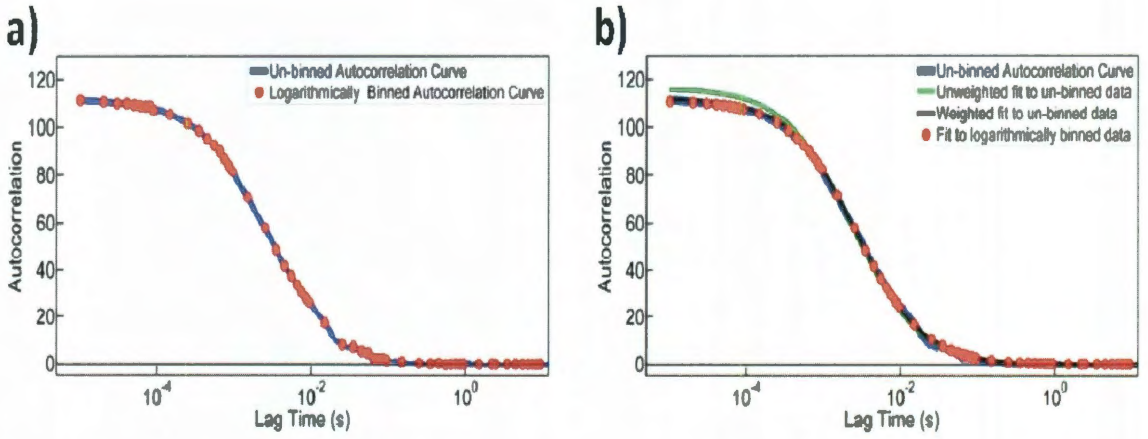

Figure 5.2: Logarithmic binning, and effects on the autocorrelation fitting. a) Logarithmically binned correlation data is shown in red, and raw data is shown in blue. b) Fits of the data (data shown in blue) with logarithmically binned autocorrelation curves (red) yield agreement within 3% of fits performed with data weighting (black). Fits performed without weighting or logarithmic binning have a poor match to the data, with 10 % difference in measured diffusion times.

5.4 Results and Discussion

5.4.1 Single Species Minimum Lag Time Parameter, (τ_{min})

The minimum autocorrelation lag time is the first lag time value for which the autocorrelation function $G(\tau)$ is calculated. This is usually the binning time at which a

photon counting board acquires data, or the smallest bin width selected for an autocorrelator board.

The limit of practical τ_{min} settings for autocorrelation analysis is dictated by several considerations. When performing software autocorrelation, although photon counting boards can acquire data with bin times (and therefore effective τ_{min} times) in sub-microsecond time scales, we have found that τ_{min} times lower than 10 μs are not practically attainable due to the volume of data produced, which can approach several gigabytes in just minutes. Storage and processing times become untenable. Hardware autocorrelator boards, on the other hand, are able to provide autocorrelation data with τ_{min} times as low as 25 ns. However, diffusion processes occur on a sub millisecond time scale and slower, while fast chemical kinetic[97] and photophysical processes (e.g. triplet state dynamics) occur on a submicrosecond time scale.[64] To achieve separation of these processes, practical τ_{min} times of 1 to 10 μs are recommended and often used for characterizing diffusion.[107]

The characteristic diffusion time for R6G in water, with a beam waist radius of ≤ 250 nm, as is currently achievable with modern equipment, is ≤ 55 μs.[110] This approaches the 1-10 μs limit for τ_{min} resolution for diffusion. Diffusion characteristics for this small molecule are often characterized under these conditions, where the full autocorrelation curve is not resolved (see Figure 5.1). Gell *et al.* reported a decrease in recovered diffusion coefficient for another small fluorescent molecular dye as time resolution was decreased by increasing τ_{min} values.[110] This raises a question as to the limits required in time resolution to accurately and consistently resolve a given decay time from the fitting of the autocorrelation curve. Not only do we see resolution limits

approached in fast diffusion, but this becomes a greater issue on the faster time scales of kinetics and photophysics that are becoming an analytical target for FCS analysis. Because the characteristic decay times measured in FCS analysis are used in very quantitative ways,[115] it is critical to understand the limits of resolution required for accurate function fitting and decay time determination.

To address the question of time resolution limits, we evaluated the behavior of recovered values for the diffusion constant not only as a function of τ_{min} but also as a function of expected decay times, by running a τ_{min} analysis for 24, 43 and 100 nm fluorescent polystyrene beads. Figure 5.3.a shows the deviation between recovered

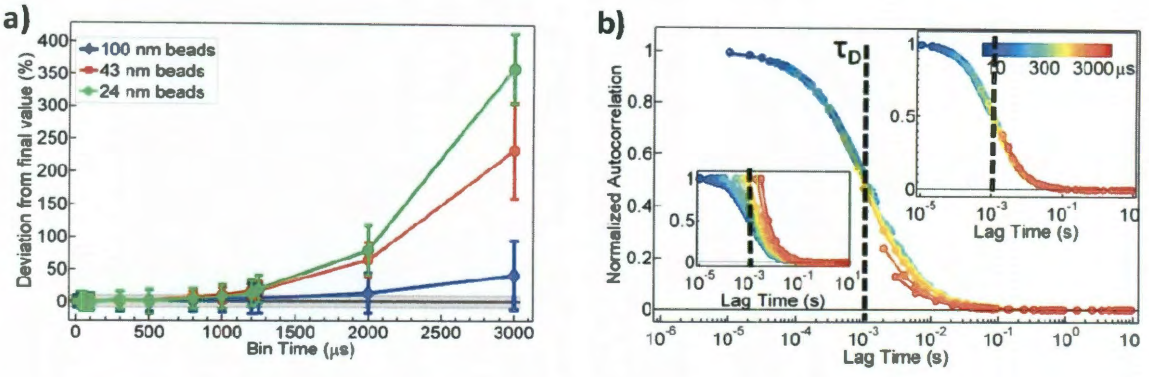

Figure 5.3. **a)** The calculated value of the diffusion coefficient is dependent on τ_{min}, and is a function of the expected value of τ_D. As minimum lag time approaches the expected value of τ_D for each species, the retrieved value of D increasingly deviates from the expected value, and the standard deviation in sequential measurements increases. The grey bar region in the graph shows the 10% deviation boundaries. **b)** The position of the autocorrelation curve is shown for 43 nm beads, for a fitted normalization, a correct normalization (upper inset), and for normalization to 1 (lower inset), as τ_{min} values approach and surpass the τ_D value. The vertical dashed line indicates the position of the characteristic decay time, τ_D, which is 0.98 ms for the 43 nm beads. Note that the dark circles on the curves mark the start of each of the successive minimum lag times evaluated.

values and the known value of the diffusion constants for the series of beads as τ_{min} (or 'Bin Time') is increased. Clearly, both the accuracy and precision of the recovered diffusion constant degrade as τ_{min} increases. For smaller species with faster diffusion,

significant deviations occur at lower values of τ_{min}. The origins of this phenomenon are demonstrated in Figure 5.3.b where we show the behavior of the autocorrelation function fitting using different normalization procedures. Fitting a measured autocorrelation function with equation (5.3) typically involves finding at least two parameters: the amplitude, and τ_d^{-1}. The amplitude is the theoretical value of the autocorrelation curve at lag time 0, $G(0)_{theo}$, with the subscript indicating that this is the value of $G(0)$ in the absence of experimental shot noise.[116] The theoretical value of $G(0)$ is the factor by which an autocorrelation curve should be normalized, and if the full curve is resolved, $G(0)_{theo} \sim G(1)$, which is experimentally accessible. The second term, τ_d^{-1}, gives us the diffusion constant, as shown in equation (5.3). When τ_{min} is increased and the full autocorrelation curve is no longer resolved, fitting for the amplitude becomes increasingly less reliable. This is demonstrated in the main body of Figure 5.3.b where we see curves normalized with the recovered fit value for the amplitude. The fitting errors in the autocorrelation are evidenced by the shift of the shorter curves (shorter curves indicate larger τ_{min} values, and in the figure, the start of each new curve is indicated by a solid black circle) away from the actual position of the fully resolved curve. This error directly impacts the recovered value of τ_d^{-1} and thus the calculated diffusion constant. We can see in the upper inset that when the amplitude is known, the fit for τ_d^{-1} is unaffected even when τ_{min} becomes very large. Note here that because we perform the autocorrelation analysis for different bin times on precisely the same data sets, we are able to use the actual value of the amplitude at short τ_{min} in the upper inset. This is because we have access to the fully resolved curve at low values of τ_{min}.

Note that over several sets of data reproduced on two experimental set-ups, we did not find a consistent monotonic trend toward longer diffusion times and smaller diffusion constants with increasing τ_{min} as reported by Gell *et al.*[110] Our data do, however, show a trend toward large uncertainty that creeps into the autocorrelation as a result of reduced quality and reliability of fitting for the amplitude. A consequence of the fact that large uncertainty is introduced into the autocorrelation fitting at too high values of τ_{min}, is that under these conditions, recovered diffusion constants cannot be correlated from one run to the next.

From the analysis, we have found that over the range of characteristic diffusion times observed, once a minimum lag time of less than approximately 2/3 the expected diffusion time was achieved, estimates of the amplitude from the fit became sufficiently good to bring recovered values of the diffusion constant to within 10% of the expected value. When this limit is surpassed in experimental environments, additional care must be taken to assure that acquire data is both reproducible and un-biased. Applying a rule of thumb of $\tau_{min} = (2/3)*\tau_D$ to measurements of R6G with a characteristic decay time of 55 μs, a minimum lag of at most 35 μs is required to achieve good estimates of D. This verifies that the current practice of using 1-10 μs values for τ_{min} with small laser focal volumes is acceptable. On our system, we see a characteristic decay time of 49 μs for R6G, allowing a τ_{min} of up to 33 μs.

There is one last point in regard to representation of normalized autocorrelation curves. Normalizing a fully resolved curve by the first point obtained in the autocorrelation function, *G(1),* provides a good visual estimate of the true normalization because in this case $G(1) \sim G(0)_{theo}$. However it is common practice to also represent

partial autocorrelation curves with the same *G(1)* normalization, rather than a fitted, $G(0)_{theo}$, amplitude normalization. In the lower inset for Figure 5.3.b, we have demonstrated the visual effect of normalization by the first point of a curve that is not fully resolved. The curve appears to migrate to longer diffusion times. This is a visual artifact of the normalization. If curves are to be compared on the same axes, and as long as enough of the autocorrelation function is resolved to return a good estimate of the value of the amplitude, it is better practice to normalize the curve to the fitted amplitude value rather than to the first point.

5.4.2 Heterogeneous Systems – Two Species

For a system in which there are two or more diffusion processes, the measured autocorrelation function consists of contribution from all diffusing species as shown in equation (5.5):[64]

$$G(\tau) = \frac{\sum \eta_i^{\,2} \langle C_i \rangle^2 G_i(\tau)}{\left(\sum \eta_i \langle C_i \rangle\right)^2}, \qquad (5.5)$$

where η_i is brightness and C_i is the concentration of species *i*.

The brightness term in equation 5.5 weights the summed autocorrelation function significantly for the well-characterized experimental system composed of polystyrene beads of known size. The relative fluorescent brightness of polystyrene beads scales as r^3 (FluoSpheres Fluorescent Microsphere Product Information, Molecular Probes, Paisley, PA). In a heterogeneous system composed of equal parts beads of radius = r and 2*r, the presence of the smaller bead is obscured in the autocorrelation data. We find that the presence of only ~0.6% of larger beads significantly affects reproducibility.

Because of the strong effect of brightness on the experimental system, as a means to clarify the effects that τ_{min} has on the recovered diffusion constants for a mulit-species system, we have examined a simulated system composed of two diffusing species, with the *same* relative brightness. The details of the simulation are discussed in Chapter 9,

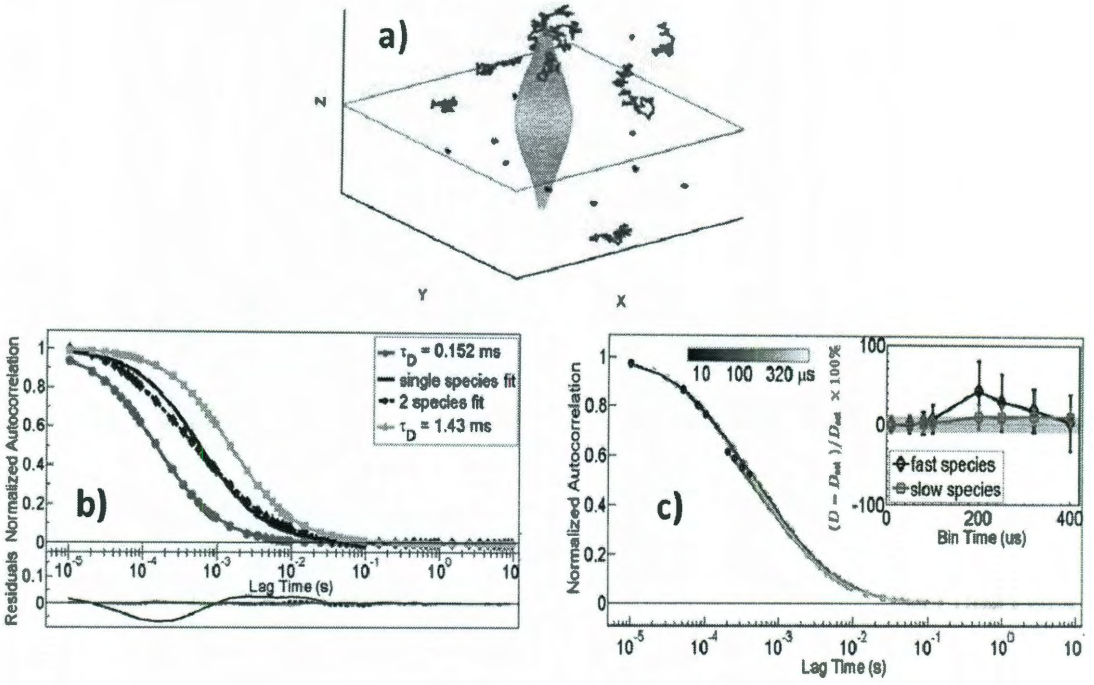

Figure 5.4: FCS for heterogeneous systems: simulation results a) A sub region of the simulation diffusion volume, centered on the focal volume, with two species, showing the first 100 steps: large lighter walks are due to a fast diffuser, small darker walks (spots) are due to a slow diffuser. **b)** Autocorrelation curves for each of the single species), and for a run with both slow (light gray, maximum step size of 25 nm), and fast (dark gray, maximum step size of 79 nm) species combined (black). **c)** Behavior of the two species autocorrelation curve (normalized to the fitted amplitude) as a function of τ_{min}, with two species fits. The inset shows the deviation of retrieved diffusion constants for each of the two species.

section 9.3[15]. Simulations of random walk processes have been established as an excellent model for real world diffusion processes,[108-109,117-118] and in this case, the use of

simulations to evaluate the effect of minimum lag time on fitting for a heterogeneous system provides an effective model of the system.

In Figure 5.4 we show a representation of a small region of a simulated sample volume, centered on an FCS focal volume comprised of excitation light with a Gaussian intensity profile. The first 100 steps of a two species simulation are shown. Note that for visual representation, the particle number in the figure is increased in comparison to the simulation conditions in which 10 particles total were placed in the sample volume. The diffusion constant for the particles shown in lighter gray is 10 times larger than that for the darker particles. The focal volume of the laser is depicted in the center of the figure (variations in color are due to graphical visualization and carry no information). The autocorrelation curves for the individual species as well as a 50/50 mix of the two are shown in Figure 5.4b. The subset of the figure shows the residuals for both single and two species fits of the mixed run.

Figure 5.4.c shows the effect of increasing τ_{min} on recovery of the diffusion constants for both the slow and fast diffusing species in the modeled multi-species system. The inset shows that while increasing τ_{min} affects both the accuracy and reproducibility of the recovered diffusion constant for the fast diffusing species just as is seen in a single species system, it is interesting to note that the reduced reliability of fitting for the fast species does not affect the reliability of the recovered diffusion constant for the slow species. This demonstrates that fitting for slower processes in the presence of fast processes that are not fully resolved will still return reliable estimates of the decay times, as long as τ_{min} limits are met for the slower process.

5.5 Conclusions

Establishing an adequate minimum lag time-to-diffusion coefficient ratio when quantifying diffusion occurring on time scales close to the time resolution of the hardware is extremely important. Through evaluation of experimental data, it is demonstrated that as τ_{min} is increased and approaches the characteristic decay time for a single diffusing particle, fitting for the autocorrelation curve becomes less accurate and the deviation increases dramatically. To recover reproducible diffusion constants, τ_{min} should not exceed 2/3 the value of the characteristic decay time.

Simulated data sets were used to show that for a binary system, in order to extract accurate diffusion constants of both species, the minimum lag times must be set with respect to the faster diffusing species. Furthermore, in a system with a multi-species autocorrelation curve, if one of two decay times is not fully resolved within the curve, the diffusion constant retrieved from two species fitting can still provide a good estimate for the remaining species as long as the autocorrelation parameters defined above are sufficient for that second species.[15]

CHAPTER 6

DIFFUSIVE TRANSPORT IN POLY(STYRENE SULFONATE) POLYMER BRUSHES*

6.1 Abstract

Diffusive transport within heterogeneous environments is a critical piece of the chemistry occurring in diverse membrane systems including proton exchange membranes and bi-layer lipid membranes. In the present study, fluorescence correlation spectroscopy was used to evaluate charged molecules diffusing within a strong polyelectrolyte polymer brush. Rhodamine-6G, a fluorescent cation, was used as a counterion probe molecule, and the strong polyelectrolyte, poly(styrene sulfonate) served as the polymer brush. Because of the role strong polyelectrolyte brushes play in electrochemical storage and conversion applications, it is important to understand and tune their transport efficiencies. Herein, preferential solvation of the probe counterion by the polymer brush as compared to the aqueous solvent phase is reported, and it is demonstrated that diffusion within the polymer brush is strongly inhibited, as evidenced by a decrease in diffusion constant of four orders of magnitude. In these studies, it also proved possible to tune transport characteristics for R6G in the brush by controlling the solvent pH, and thus the ionic strength of the solvent. The diffusion characteristics within the charged brush system depend on the brush density as well as the effective interaction potential between the probe ions and the brush. In response to changes in ionic strength of the solution, it was found that these two properties act in opposition to each other within this strong polyelectrolyte polymer brush system. A stochastic random walk model was developed

*Contents from this chapter have been published in the following journal article: Reznik, C., Darugar, Q., Wheat, A., Fulghum, T., Advincula, R., Landes, C.F. Single Ion Diffusive Transport within a Poly(styrene sulfonate) Polymer Brush Matrix Probed by Fluorescence Correlation Spectroscopy. *J. Phys. Chem. B.* 112(35), 108990-10897 (2008).

to simulate interaction of a diffusing charged particle with a periodic potential, to show the response of characteristic diffusion times to electrostatic field strengths. More generally, these results support the use of FCS to evaluate local charge transport properties within polyelectrolyte brush systems, and demonstrate that the technique shows promise in the development of novel polyelectrolyte films for charge storage/transport materials. The combined results of the experiments and simulations demonstrate that responsive diffusion characteristics in this brush system are dominated by changes in Coulombic interactions rather than changes in brush density.

6.2 Introduction

Advances in the measurement and theoretical description of ion/polyelectrolyte interactions[119-122] have contributed to a growing understanding of the dynamics of polyelectrolyte thin films. Ultimately, a detailed characterization of ion transport properties and solvation response within these thin films will advance applied technologies that utilize associated switchable surfaces,[19,123] and charge storage and transport properties of the films[42]. Arenas in which these kinds of properties will play a role include biosensing[19] and fuel cell technologies[32,124]. Already, the charge transport behavior of polyelectrolyte thin-films has led to the successful commercial adoption of the fluorinated synthetic polymer, NaFion® (Dupont), as a fuel cell proton exchange membrane (PEM)[125].

Both polyelectrolyte nanostructure and local solvation dynamics affect ion transport efficiencies[126], and several recent studies suggest that modifications to thin film nanostructures could lead to potential PEM design improvements[28,31]. Specifically, poly(styrene sulfonate) (PSS) membranes that exhibit favorable transport properties have been observed to degrade over time. Improvements to membrane lifetimes, however, have been achieved by the inclusion of cross-linked resins within the PSS PEM matrix[32]. Additionally, as discussed in Chapter 2, it is possible to increase charge transfer capacities by orders of magnitude by using polymer brush architecture, which has higher internal order compared to an isotropic thin film architecture[42].

At a high grafting density the polymer chains tend to extend in the direction normal to the surface[127]. In the case of strong polyelectrolytes such as NaFion® and PSS, additional inter-chain Coulombic repulsion due to the presence of fixed charges along

the polymer chain gives rise to further extension of the chain[128]. Increase in charge transfer seen in an oriented PB system is attributed to transport of charges along the length of the oriented polymer chains rather than via chain hopping through the disordered arrangement present in an isotropic membrane[42].

Polymer brush membranes provide an intriguing polyelectrolyte system for transport study: first, because of the response of charge transport performance within this type of oriented system to tunable brush internal nanostructures; and second, because of the degree of control over bulk morphology that is possible by tuning the environmental (solvation) conditions. Numerous theoretical treatments of the characteristics of polymer brushes in response to solvation conditions have been reported for both neutral[127] and charged[128] brush systems, and recently several groups have begun to address the dynamics of PB systems. For example, Fytas, et. al., have used evanescent-wave dynamic light-scattering to probe polymer chain dynamics[129], Choi et. al. have used cyclic voltammetry to measure rates of electron transfer in a polyelectrolyte brush[126] and Limpoco et. al. have used friction force measurements to characterize shear forces in various solvent subphases for polystyrene brushes[85]. Additionally, several studies using fluorescence correlation spectroscopy to look at diffusion of various mobile polymer macromolecules in association with polymer brush systems have been reported[103,130].

In this work, I contribute a detailed description of the competing processes that drive internal transport characteristics of a strong polyelectrolyte brush system by using Fluorescence Correlation Spectroscopy (FCS) to characterize ion mobility within a PSS polymer brush membrane. I report on the diffusion of R6G, a positively charged fluorescent ion, as it interacts with a negatively charged polyelectrolyte brush, and

resolve the response of diffusion characteristics to changes in the polymer brush ionic environment as controlled via solvent pH. Lastly, I present a simple 2-D random walk model for the motion of a charged particle experiencing a periodic potential field. Through the experimental results and this model I show that responsive diffusion characteristics are dominated by electrostatic interactions between the probe molecule and the strongly charged polymer brush.

6.3 Data Acquisition and Analysis

6.3.1 Acquisition Parameters

All autocorrelation functions were calculated directly from signal trajectories as seen in the inset in Figure 5.1, using programs written in Matlab (R2006a). All autocorrelation curves shown in this paper are normalized. Data was acquired with a bin time of 10 μs. To optimize computing performance, the data was further binned during analysis to 1 ms for all data with long diffusion times. The maximum lag time, τ_{max}, was set at 12 seconds for all standards diffusing in water, and at 300 seconds for all diffusion processes occurring in the presence of polymer brush, so as to cover the appropriate lag-time range. All data was averaged over an acquisition period of 5 minutes, either directly within the AC calculation in the case of samples analyzed with a 300 second τ_{max}, or via post AC function averaging in the case of standards diffusing in water with a τ_{max} of 12 seconds.

Focal volume parameters were fit using AC curves for 40 nm beads diffusing in water and equation (5.3). Experimental reproducibility of standards was within 8%.

Agreement between the fitted and experimental autocorrelation curves is good, with a root mean square error of below 0.02% for this set-up.

6.3.2 Application to the Thin Film System

The application of FCS to a thin film system requires consideration of the placement of the sample with respect to the focal volume[91]. Figure 6.1.a represents the physical system investigated, and the positioning of the polymer brush sample within the focal volume. Note that the figure in 6.1.a is not to scale. The focal volume z_0 distance was fit at 1 μm[106], giving a total focal volume height of 2 μm. The thickness of solvated

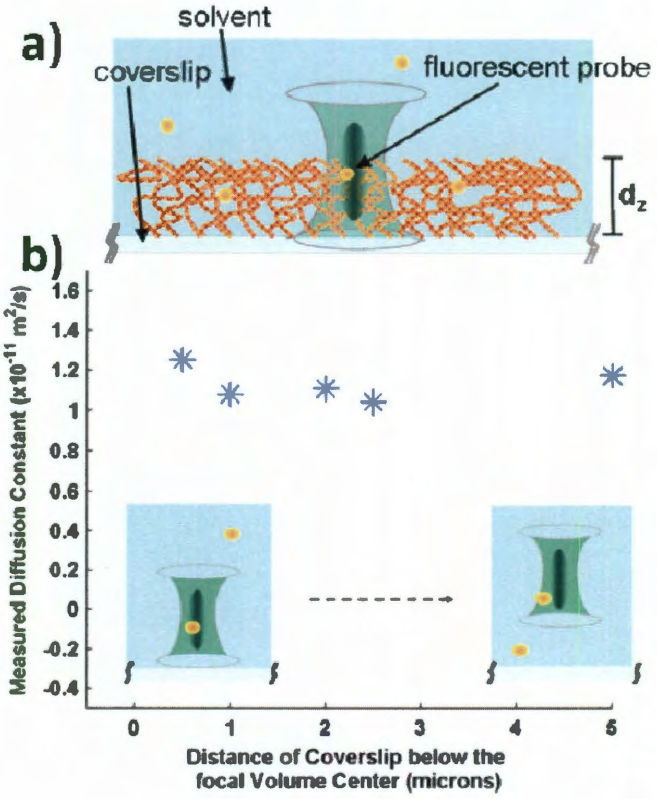

Figure 6.1: Placement of thin film sample within focal volume. a) Representation of the physical system. b) Independence of the autocorrelation function on depth for a homogeneous environment. Shown are diffusion constants for 40 nm beads diffusing in water at different positions of the coverslip/sample relative to the focal volume. The inset is a cartoon image of two possible positions of the coverslip with respect to the focal volume. The standard deviation of the diffusion constant over these measurements was <8%.

polymer brush thin films synthesized by free radical polymerization can range from tens to hundreds of nanometers depending on synthesis conditions and solvent quality[84-85,131]. After setting the visual focus at the coverslip, the piezo-stage controller was used to position the coverslip 500 nm below this point, so that the entire $1/e^2$ focal volume rested just at the coverslip surface, as is depicted in Figure 6.1.a. Within the focal volume, then, this geometry encompasses polymer thin film and the water solvent.

It should be noted that polymer brush thin film characteristics such as density and chain dynamics vary in z, along the optical axis[131]. The FCS measurements provide an average diffusion response over the z axis. To assure that the measured AC function was not dependent on relative placement of the sample chamber over the focal volume due to factors other than the geometry of the thin-film sample itself, the AC functions for 40 nm beads diffusing in water (constituting a homogeneous environment) were measured with the sample at various positions with respect to the focal volume. The diffusion constants obtained at different positions of the coverslip below the beam waist are shown in Figure 6.2.b. For a homogeneous sample within a range of positions applicable to the experimental conditions, the data show that the instrumental set-up does not impart a bias to the AC function as a function of sample positioning in the z direction.

All reported data was taken from PSS brush surfaces which were allowed time to equilibrate upon introduction of the solvent with dye to the surface.

6.3.3 Data Treatment

The geometry of the thin-film system also needs to be addressed when applying the standard FCS fitting equations given in 5.2 and 5.3. In conjunction with studies on bio-membrane systems, Gennerich and Schild have shown that when FCS is applied to an

environment with restricted geometry, modification of the diffusion model may be required[74]. In the case of a system restricted in geometry along the optical axis only, the authors show that the AC expression approaches the 2D diffusion equation, (5.2), for values of $d_z < z_0$ (see Figure 6.2.a for d_z), and approaches the 3D diffusion equation, (5.3), for values of $d_z > z_0$. In this case, fitting of data obtained in the presence of the polymer thin film with both the 2D and 3D equations yielded less than 2% difference in both the diffusion constant, D, and the normalized root mean square error for the fits. This difference is well within the experimental standard deviation, therefore, all data reported herein was fit with equation (5.3).

6.4 Results

6.4.1 Interaction of the Fluorescent Probe and the Brush

Figure 6.2 illustrates that R6G diffusion within the PSS polymer brush can be distinguished from diffusion in water. The presence of the PSS polymer brush in the FCS focal volume markedly slows the diffusion of the fluorescent probe. Calculated diffusion times increased by 4 orders of magnitude, from an average τ_D of 57 ± 5 μs in water to a τ_D of 300 ± 9 ms in the brush, with associated diffusion constants of $4.0 \pm 0.9 \times 10^{-10}$ m^2/s and $7 \pm 2 \times 10^{-14}$ m^2/s respectively. Additionally, preferential interaction between the R6G counter ion and the brush is evident, as opposed to R6G and the solvent. This preference is evident when comparing the experimental AC curves at short times (Figure 6.2 inset) with the AC curves of a simulated system that has both fast and slow diffusers (Figure 6.3). Signal trajectories for the simulated system shown in Figure 6.3 were

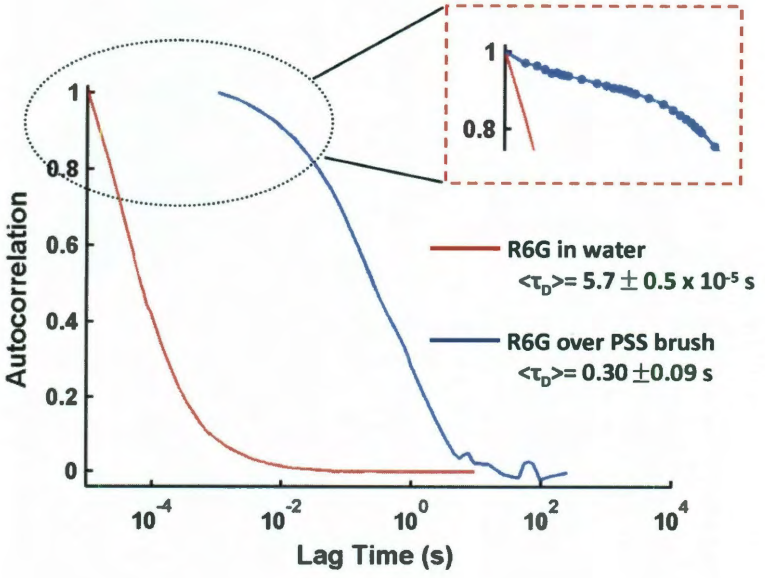

Figure 6.2: Autocorrelation functions shown for R6G diffusing in water over a clean coverslip with a characteristic diffusion time (shown in axes) and an associated diffusion constant of $4.0 \pm 0.3 \times 10^{-10}$ m^2/s, and also in water over a coverslip modified with PSS brush, with $D = 7 \pm 2 \times 10^{-14}$ m^2/s. The PSS diffusion curve is an average over 3 runs. Inset shows extension of the AC function to the time resolution necessary to pick up diffusion events with decay times on the order of R6G in water.

generated with contribution from two Gaussian signals with an order of magnitude difference in diffusion times. The simulated curves demonstrate the convolution of diffusion decay times evident in the AC function when there are both slow and fast diffusers contributing to a signal trajectory. Note that these convolution features remain clear for diffusion constants differing by up to four orders of magnitude in this model (data not shown). As seen in the inset of Figure 6.2, the experimental data do not show evidence of significant water-like fast diffusers despite that fact that the FCS focal volume encompasses both brush and a significant volume of the water environment. Recall that a 1 μm dimension is estimated for the focal volume z_o, with a brush height of << 1.0 μm. Thus, we can conclude that the R6G is preferentially solvated by the polymer brush. This is not surprising given the electrostatic environment that provides

opportunity both Coulomb attraction and π-π interactions[132] between the PSS and the R6G. The favorable electrostatic environment contributes to making PSS a better solvent for R6G than water.

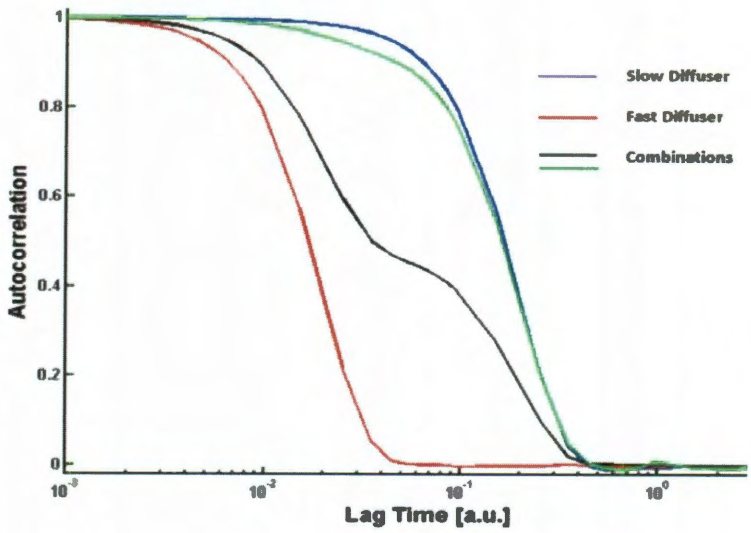

Figure 6.3: AC curves for modeled signal trajectories showing a fast and slow diffuser with an order of magnitude difference in diffusion constants, along with two curves generated from a mix of the slow and fast signals at different modeled relative concentrations of: 1:1 (black) and 20:1 (green) (slow:fast).

As noted in Chapter 5, parameter choices such as selection of minimum and maximum lag times[133], particularly in combination with AC functions calculated over multiple diffusing components can affect the absolute values of measured diffusion constants and must be selected carefully. Another factor impacting the value of diffusion constants measured by FCS is existence of a differential in refractive index of the sample medium in comparison to the medium in which the focal volume was calibrated. Because the refractive index of the medium affects the focal volume size, characteristic diffusion times can be impacted. However, this effect on the focal volume is dependent on the path length of the probe light through the medium, and it has been suggested that

refractive index mismatch errors in FCS can be minimized by keeping the laser path length through mismatched sample media to less than 10 microns[104]. In this experimental environment, the polymer medium is at least an order of magnitude below the suggested standard. Therefore, it is expected that under these conditions the absolute refractive index differential is small, and that any deviations fall well within the existing experimental error.

6.4.2 Polymer Brush Characteristics

The experimental data also provide a measure of the distribution of nanoscale diffusion environments within the brush. The standard deviation achieved for diffusion constants for R6G diffusing in the presence of the polymer brush surface is 22%. This standard deviation was calculated from diffusion constants evaluated over eight separate analyses taken in sequence at the same location in one sample. For reference, the standard deviation in diffusion constants measured for 40 nm beads diffusing in water with the FCS system is 8%. Part of this spread of achieved values can be attributed to heterogeneity in the brush environment, both in z, as mentioned earlier, and laterally. It should be noted that part of the increased deviation in measured diffusion constants must be attributed to the nature of the AC function as characteristic diffusion times approach the maximum AC lag time for a trajectory, as is observed is the case with the much slower diffusion of R6G in the presence of the brush. The autocorrelation function effectively averages over hundreds of single molecule diffusion events through the focal volume and many of the effects of small local heterogeneities in an environment are averaged out during analysis. However as the maximum lag time is approached, less averaging is possible and this contributes to noise in the AC curve that can be seen at

long times in Figure 6.4, where the function decays toward zero[111,133]. This noise can affect the calculated diffusion constant through distortion of both the slope and position of the decay curve.

The standard deviation for AC functions obtained at several different positions on the modified brush surfaces was obtained as well, and these results are shown in Figure 6.4. Three separate replicates of the AC functions from three different positions are graphed, two of which were taken on one surface, and the other from a second surface

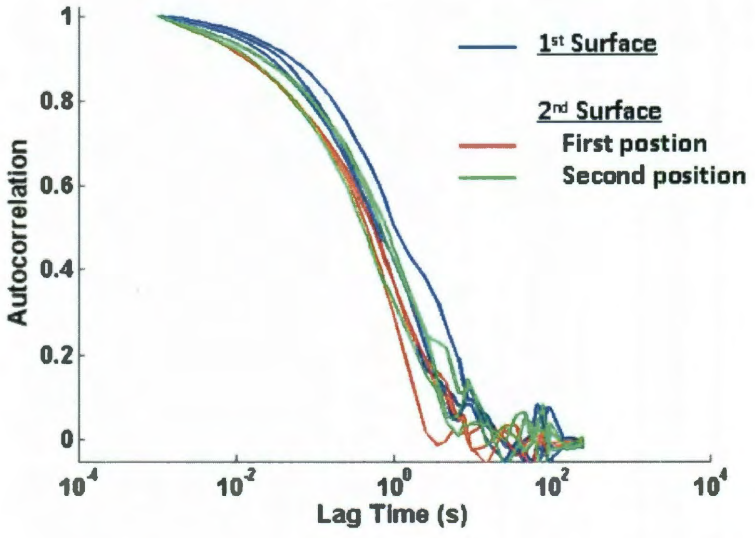

Figure 6.4. Uniformity of the autocorrelation functions obtained from diffusion of R6G over PSS brush modified surfaces. AC curves are shown for diffusion measured at three separate positions on PSS surfaces, including data from two separate PSS surfaces from the same synthesis batch. Analysis conditions were comparable, and three replicate readings were obtained for each sample.

from the same synthesis batch. The two surfaces were evaluated on different days. The standard deviation for the diffusion constant was 29% for the nine AC functions obtained over these three regions. This is just 7% higher than the standard deviation obtained at one location. Considering that AC for diffusion in water, a purely homogeneous environment, shows standard deviations of 8%, the data shows that diffusive behavior

over macroscopic regions of the PSS modified surface is reasonably constant. The FCS data from varied regions on the brush surfaces, combined with data from AFM images taken at several locations on the brush surface indicate uniform coverage of the surface, while the variation achieved from FCS analysis at a single position indicates that there is a fairly uniform distribution of diffusion landscapes available to the R6G probe molecule as it traverses the polymer brush environment.

6.4.3 pH Response of the Diffusion Constant

Polystyrene sulfonate is a strong polyelectrolye, and as such is fully ionized within the pH range evaluated. Adjustments in pH, therefore, have the effect of changing ionic environment within the brush by changing the concentration of free H^+ ions available. Figure 6.5 shows that upon a reduction of pH from neutral to a pH of 3.5, the characteristic diffusion time of R6G in the presence of the polymer brush decreased from

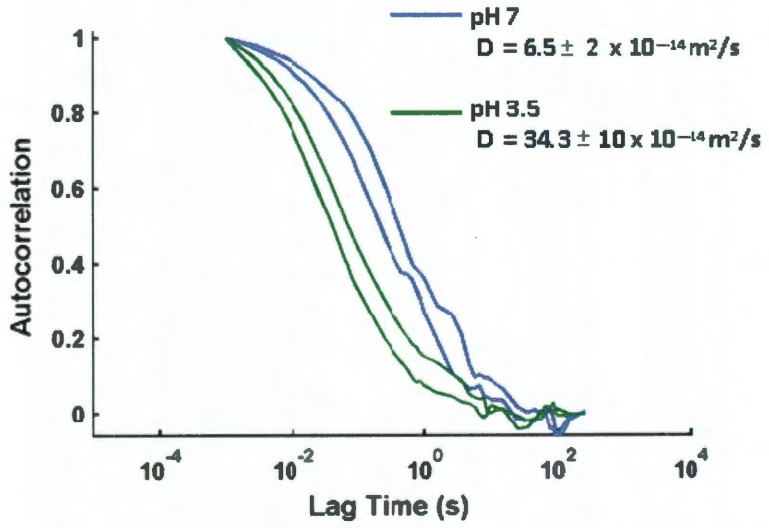

Figure 6.5: The range of AC functions obtained for R6G diffusing over PSS brush modified surfaces in solutions of pH 7 and 3.5. Average D: at pH 7 is $6.5 \pm 2 \times 10^{-14}$ m^2/s; and at pH 3.5 is = $34.3 \pm 10 \times 10^{-14}$ m^2/s.

an average value of 0.30 ± 0.09 seconds to 0.07 ± 0.02 seconds. Shown on the graph are the AC functions at the 29% standard deviation boundaries for both the neutral and pH 3.5 measures. pH dependence of diffusion of R6G on a clean coverslip was evaluated as well. R6G diffusion rates did not show a dependence on pH. Figure 6.6 shows autocorrelation curves for diffusion of R6G in bulk solution at pH 7 and pH 3.5. Diffusion times obtained from a fit of the data return 42 μs and 39 μs respectively. This demonstrates that in the absence of the PSS polymer brush, the diffusion of R6G is not dependent upon pH in this pH range.

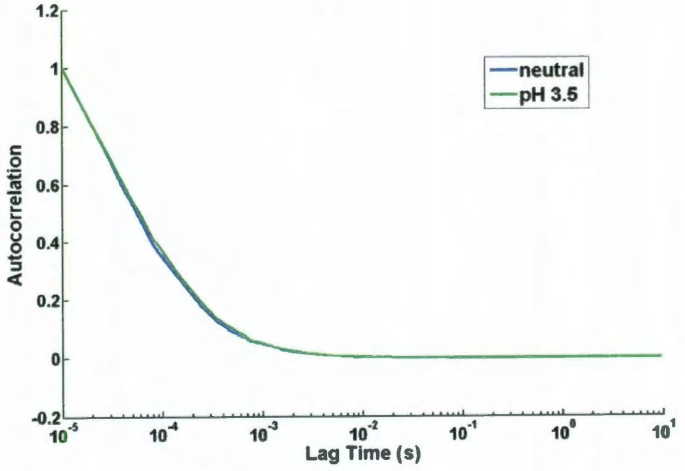

Figure 6.6: pH dependence diffusion of R6G in aqueous solution. Diffusion times are 42 μs ± 3 μs at neutral pH, and 39 ± 4 μs at pH 3.5.

In Figure 6.7, data extending the pH range, on a different brush synthesis (synthesis batch 2) is shown. It should be noted that fitting of the autocorrelation curves

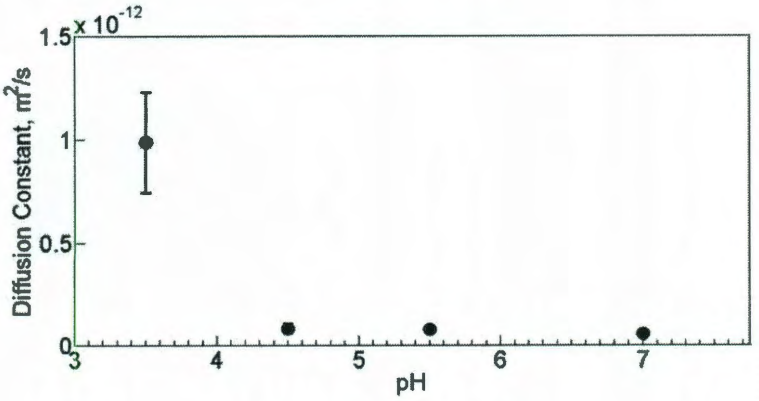

Figure 6.7: pH dependence of the diffusion constant.

obtained for translational diffusion of the fluorophore was done using a two component diffusive transport fit in each case.[108] Curves were typically well fit by the two component fitting, and revealed the existence of a second, long-time decay region in many cases, which had a time scale of seconds. The long-time decay may be attributable to the adsorption events evident in the single molecule traces.[17,65] Quantitative evaluation of the long-time component was not possible due to limitations to the total experiment time, and the long time requirements to resolve these quantitatively in an FCS experiment.[15,112]

As can be seen in Figure 6.7, transport rates were effectively constant over a change of 3 orders of magnitude in H^+ concentration, followed by the strong jump in rate from $5 \pm 1 \times 10^{-14}$ m^2/s to $9 \pm 2.4 \times 10^{-13}$ m^2/s at an H^+ concentration of 0.0025 M (corresponding to a pH of 3.5). As discussed below, it is known that completely ionized, strong polyelectrolytes such as sodium PSS exhibit only slight changes in brush height upon change in pH, which can be attributed to the fact that the sulfonate groups do not begin to undergo significant protonation before pH values of close to 1 are reached ($pK_a \sim$

1).[120,128,134-135] Although the theoretical and experimental characterization of strong polyelectrolyte brushes indicates there will be little change in this morphological characteristic, the abrupt switch in transport rates nevertheless suggests that there is a dramatic and abrupt switch in the nanoscale environment experienced by the molecular probe. As discussed in Chapter 3, to verify that this change in measured diffusional behavior does not arise from changes to the dye at low pH, the spectral response of R6G at the solution pH values used in this study was measured, and no shift in the emission wavelength over this pH range was observed to indicate changes to the structure of the molecule (Figure 3.6). Note that changes evident in the measured intensity for R6G as pH is varied do not affect the diffusion constant measured by FCS for a single species (see equation (5.3)).

6.5 Discussion

The primary experimental results are summarized as follows: First, the diffusion of the R6G probe slows dramatically when it is solvated by the polymer brush in comparison to water. Second, when additional positive charge is present in the form of protons, the diffusion constant of the cationic probe increases. We can start a discussion of the first result in the simple terms of the Stokes-Einstein equation (5.4), and note that in this case, with the temperature held constant, the only physical factor that contributes to the slowed diffusion is increased viscosity. It is consistent that a polymer brush, with its higher mass density compared to water, would have a higher effective viscosity.

Understanding, further, how viscosity of a polyelectrolyte brush changes as a function of electrostatic conditions, is a more complex matter. This is because both the

brush density and the counterion/electrolyte Coulombic potential interaction depend on the ionic conditions in the co-solvent, water. Brush thickness due to swelling has been shown both experimentally and theoretically to depend upon solvent governed interactions that include electrostatics; steric and entropic effects; and for polyelectrolyte brushes, a Donnan potential giving rise to swelling induced by osmotic pressure arising from the localization of counter ions within the brush.[119-121] For the polyelectrolyte brush, the key contribution to these interactions is the presence of fixed periodic charges along the polymer chain. It is this distributed periodic charge that causes the polyelectrolyte to adopt a more extended conformation at relevant brush densities[136] as repulsive Coulombic interactions and entropic elasticity contributions to the overall free energy of the system are balanced[120].

Generally, for a strong polyelectrolyte brush in the osmotic brush regime and at the strong stretching limit, the degree of brush extension (and thus the brush density and viscosity) depends directly on the degree of charging of the monomer:

$$h \approx Na\frac{f}{1+f}, \tag{6.1}$$

with h being the extension of the brush, N being the length of the chain, a being a monomer size parameter, and f being the degree of charging[120]. The osmotic brush regime is obtained under conditions of low to moderate ion concentrations and at experimentally relevant brush densities. In contrast, at high ionic concentration, a salted brush regime is obtained, in which height scales with ion concentration as a weak inverse power law.

Equation (6.1) provides a relation between the brush height of the strong polyacid polymer brush, and the degree of charge shielding provided by protons. As proton

concentration, and therefore the effective ionic concentration around the strong polyacid, is increased, charge shielding leads to increased brush density as repulsive forces between the chains are diminished. Slight scaling of brush length with changing ionic concentration in the osmotic brush regime is demonstrated in experimental work on a poly(styrene)-b-poly(styrene sodium sulfonate) block copolymer colloidal brush system by Mohanty et. al.[134] An incremental increase in brush density should correlate with incrementally higher viscosity and, if it were the only factor at play in this system, would result in *slower* diffusion of a probe molecule. As can be observed in Figure 6.6, however, diffusion behavior changes in the opposite direction. Thus a more complicated model is needed.

Charge shielding contributes an additional factor to the overall dynamics of the system by affecting electrostatic coupling. Debye screening lengths for the charged brush system in water at neutral pH are estimated to be ~ 17 to 30 Å, dependent upon the estimated distance between grafting points, establishing relatively short distances over which charge separation can occur.[128] As solvent conditions are adjusted, charge shielding by the solvent increases, and the strength of electrostatic coupling interactions between individual counterions and PSS decreases. Lifson and Jackson made connections between the diffusion times of counter ions and field electrostatic coupling strengths, through the derivation of analytical expressions for the diffusion times of ions within several different charged polymer geometries[137]. These expressions considered diffusion of a counterion within a single, untethered polymer, and showed exponential dependence of diffusion times on field strength.

To address the effect on diffusion times of a periodic potential field, I constructed a simple random walk simulation in a 2-D periodic field, with an embedded signal generating region as a model for the FCS focal volume. The autocorrelation analysis measured on signal trajectories created in this model shows a change in the position of the autocorrelation function along the time axis for random walks in periodic, electrostatic fields with varied strengths. Shown in Figure 6.8 are depictions of the periodic electrostatic field used, built from a Coulomb potential of the form:

$$u(r_{ij}) = \begin{cases} \xi_i \dfrac{Z_j}{r_{ij}}, r_{ij} \le r_{\text{lim}} \\ \\ 0, r_{ij} > r_{\text{lim}} \end{cases} \tag{6.2}$$

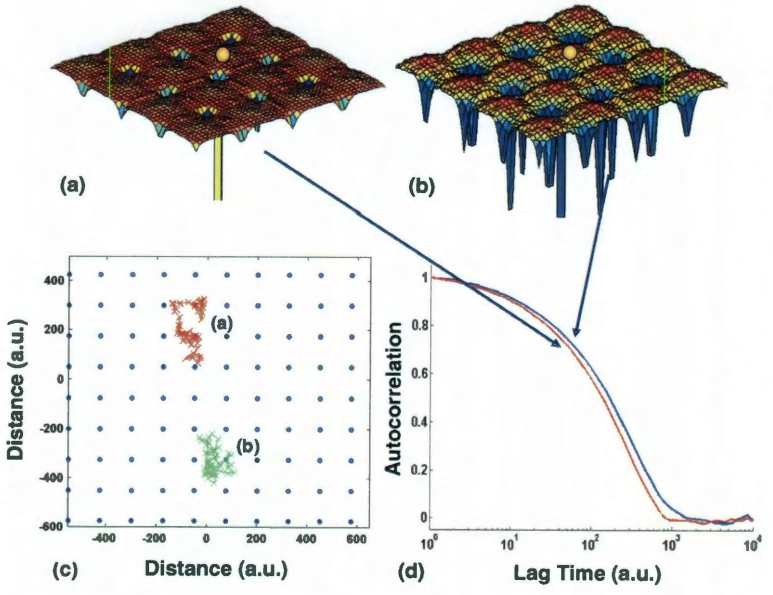

Figure 6.8. Effect of potential field strength on the AC function calculated from the modeled trajectory of a particle diffusing in 2 dimensions. Parts (a) and (b) represent the potential fields. The interaction potential term in field (b) is ten times stronger than for the field shown in (a) (the scale is the same for both images). In (c), a representative random walk trajectory is shown for each field. In (d), the AC curves obtained from a random walk in the indicated fields is shown.

where ξ is an interaction constant that includes charge on the diffusing particle, solute dielectric constant and a temperature term; Z is the variable field strength; and r_{lim} is a cut-off radius limiting the electrostatic field due to point charges far away from the regions through which the counterion diffuses. Note that excluded volume effects have been neglected in this simulation. Further details of the simulation conditions are discussed in Chapter 9.

The strength of field b) in Figure 6.8 results from an order of magnitude change in the variable Z from that of field a), corresponding to a 10 times stronger field in b). As we can see, stronger electrostatic interactions shift the AC decay to longer times, and contribute to slower characteristic decay times. The random walk model shows this effect across several orders of magnitude.

6.6 Conclusions

FCS was used to evaluate the diffusive transport behaviors of a positively charged counterion (the fluorescent probe) in the presence of a strong polyelectrolyte brush. These studies demonstrate that FCS is able to clearly resolve charge transport characteristics within the strongly charged polymer brush thin film. Two competing mechanisms are shown to contribute to diffusional dynamics within the strong polyelectrolyte brush, and undoubtedly to the macroscale charge transfer efficacy. In considering charge transport performance of a PEM, it is necessary to consider the effects of an interaction potential on the AC function as predicted by the model, as well as the effects of the corresponding brush density. Because the fluorescent probe, R6G, functions as a counterion in this system, and because FCS can be used to measure the ion

transport directly in the brush, it should be possible to use this technique to optimize macroscale charge transport properties towards the goal of obtaining better polyelectrolyte membranes. Additionally, an effective switching of ion transport rates in the brush is observed when pH is lowered to a value of 3.5, providing support for the goal of developing polymer brush thin films as smart surfaces[5] in charge and ion transport applications by utilizing this inherent switchable functionality.

6.7 Acknowledgements

For collaboration in this work, I thank the following individuals: Alexei Tcherniak (Rice University, Dr. Stephan Link) for discussions contributing to FCS application and analysis; Dr. Bittner and Dr. Lubchenko (University of Houston), for helpful discussion regarding the random walk model; and to Nicel Estilore, Jin Young Park, and Guoqian Jiang (University of Houston, Dr. Advincula) for polymer brush characterization. Additionally, I thank both the Texas Center for Super Conductivity, and the University of Houston for generous funding of this work.

CHAPTER 7

SINGLE MOLECULE SPECTROSCOPY REVEALS HETEROGENEOUS TRANSPORT MECHANISMS FOR MOLECULAR IONS IN A POLYELETROLYTE POLYMER BRUSH*

7.1 Abstract

Single molecule polarization and fluorescence correlation spectroscopy were used to evaluate heterogeneous transport mechanisms of molecular ions within supported polyelectrolyte brushes. Observed modes of diffusive transport include periods of significantly restricted rotational motion, often maintained over tens of milliseconds; periods of fast molecular rotation; and occasional adsorption of fluorescent probe molecules in the brush. The studies reveal rapid switching between orientational states during each observed mode of motion. Through quantitative analysis of state occupation times, the rate constants for transitions from weakly associated to strongly associated states were extracted. These single molecule studies demonstrate the presence of dynamic, anisotropic interactions between the charged molecular probe and the polymer brush.

*Contents from this chapter have been published in the following journal article and accompanying on-line supporting information: Reznik, C., Estillore, N., Advincula, R., Landes, C.F. Single Molecule Spectroscopy Reveals Heterogeneous Transport Mechanisms for Molecular Ions in a Polyelectrolyte Polymer Brush. *J. Phys. Chem. B.* 113(44), 14611-14618 (2009).

7.2 Introduction

Theoretical and experimental studies show a clear relationship between material transport properties and specific nano-scale structural and chemical characteristics for a variety of materials important to both biological and materials engineering processes.[28-29,138-142] As the quest for cheap, effective alternative energy sources intensifies, it is important to clarify this nano-scale structure-function relationship in polymeric materials with energy conversion/storage applications. In particular, the structure-function relationship is of interest in polymer brush thin film architecture because the polymer brush structure possesses fundamental properties that are highly advantageous: 1) a tunable nano/chemical structure as a result of controlled polymer synthesis and grafting techniques,[143-146] 2) specific orientation,[41] and 3) stimuli responsiveness.[5,19,42,128,147] Because of these characteristics, a major focus of current polymer thin film materials research is the rational synthetic development of functional brush thin-layers through incorporation of nanostructural characteristics that contribute to increased performance.[28] The goal would be to combine tuned functional behaviors with specific stimuli responsive conformational change to generate functional changes on demand.[5,143-144,148] As discussed in Chapter 2, the application of single molecule analytical methods to address processes underlying the functional properties of these materials will play an important role in future informed-design efforts.

Specifically, single molecule fluorescence techniques that can resolve the orthogonal components of polarized fluorescent light provide a window into molecular orientational states within a given chemical system.[149-152] These techniques have been used successfully by several investigators to probe the rotational behavior of single,

translationally stationary molecules embedded in melt materials near the glass transition temperature, where rotational diffusion is quite slow (on the order of hundreds of milliseconds to tens of seconds), and significant translational diffusion is not observed.[56,149,153-155] The extent of local environment stability/ heterogeneity in time and space,[56] and both short and long-range interactions between the host environment and a molecular probe have been reported in these works.[151,153,156] Broadly speaking, single molecule techniques are advantageous because chemical and kinetic information is compiled one molecule at a time and thus the full distribution of heterogeneous dynamics that contribute to an ensemble of molecular behaviors becomes accessible.[48-51] The ability to resolve underlying heterogeneous processes has revealed the molecular level mechanisms and associated dynamics of, for instance, charge transport along a surface and into bulk solution,[139] and within highly structured environments, such as within networks of nanochannels as shown by Jung, *et al.*[16,55,60]

Here, I report on investigations into single molecule orientation states in a polymer brush membrane solvated in aqueous solution. This study extends previous molecular orientation studies to a polymer brush thin film environment, and to a regime in which translational diffusion is observed.[55,157] Single molecule polarization trajectories of these freely diffusing particles are evaluated[158-159] to extract quantitative information about the freedom of both the rotational and translational movement of a probe molecule in an oriented and charge-rich environment. These single molecule transport studies reveal that several distinct modes of motion are sampled by Rhodamine 6G (R6G), a diffusing cationic and anisotropic molecular dye, as it interacts with a polyanionic sodium poly(styrene sulfonate) (PSS) polymer brush. Additionally, periods

of significantly restricted rotational motion, often maintained over tens of milliseconds, and slowed translational diffusion are apparent, along with occasional adsorption of the probe molecules to the polymer brush. Quantitative evaluation of polarization state occupation times shows that R6G spends a majority of time strongly associated with the polymer brush at neutral pH. Also observed is rapid switching between two distinct polarization states. This rapid orientational switching is observed even during apparent surface adsorption. The existence of long-lived molecular orientations along with discrete and repeated jumps in polarization state between two orientations indicates fast rotational transitions from one long-lived low energy conformation to another within the polymer matrix, with relatively stable orientation of the molecule between jumps. Overall, these single molecule studies demonstrate dynamic, anisotropic interactions between the charged molecular probe and the polymer brush.

7.3 The Experimental System

Recall that in this system there is a positively charged molecular dye (long dimension of 13.8 Å, see Figure 3.5)[86] diffusing within a highly charged and oriented thin film environment. The dry polymer brush thickness was measured via ellipsometry to be 38 nm ± 4 nm (using an estimated refractive index of 1.59 for the PSS brush) for the synthesis batch evaluated in this study. All experiments were carried out at room temperature (20.7° C ± 1° C). As discussed in Chapter 6, and illustrated in Figure 6.1, the diffusion volume in which fluorescence is excited and collected includes both polymer brush thin layer and aqueous sample regions, so that it is possible to detect diffusion events in both kinds of environment. In fact, the polymer brush occupies <<

10% of the height of the focal volume. However, for this highly charged Na PSS/R6G system, our previous findings demonstrate that R6G dye molecules locate preferentially at or within the polymer brush, rather than in the aqueous portion of the sample volume,[16] and the majority of the events that are recorded are those showing slow diffusion within the polymer brush. In the previous chapter, the nanoscale heterogeneity of the polymer brush surface is discussed, and the remarkable reproducibility of diffusion measurements given this heterogeneity is demonstrated. All of the analyses presented in the present work, including data reproduction and error bars, were performed on samples from a single brush synthesis batch. Inter-batch reproductions confirm trends but are not used for quantitative comparisons, because their inclusion potentially broadens the data heterogeneously due to differences in brush height/density rather than due to distinct differences in transport mechanisms. In the current study, all measurements were performed with multiple repetitions and at multiple locations (from two to three locations) on each polymer brush surface. The errors given in the reported data reflect the deviations seen across the brush surface, and from one run to the next.

7.4 Single Molecule Polarization Set-up

The experimental detection scheme used is shown in Figure 7.1. Circularly polarized light is used for excitation, and because of this, all molecules entering the focal volume are excited without respect to their orientation in the x-y plane. Subsequent to excitation, fluorescence emission from a molecule occurs along the molecular emission dipole in some propagation direction, **k**. The x-y perpendicular components of polarized fluorescence emission in the image plane are then resolved using a polarization beam

splitter and two orthogonal detectors labeled in Figure 7.1 as the 's' and 'p' detectors. Note that s and p polarized light, as indicated in the Figure, are identified as such with respect to the orientation of the polarization beam splitting cube.[151]

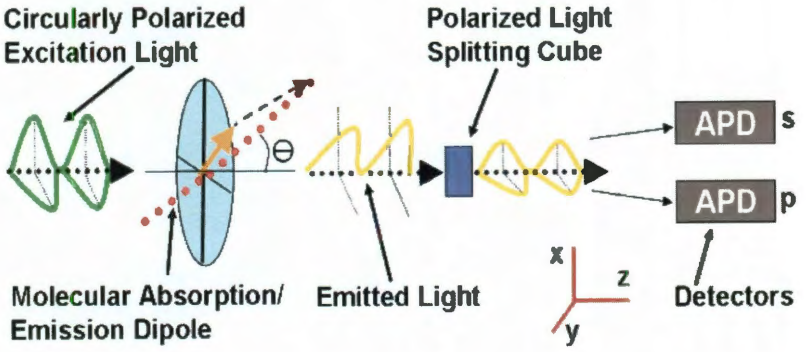

Figure 7.1: Detection scheme for polarized light emitted along a molecular emission dipole. Here, the absorption and emission dipoles are collinear. Theta is the angle adopted by the dipole with respect to the propagation direction of the excitation light (z axis). The azimuthal angle, Φ is the angle made with respect to x by the projection of the molecular dipole (orange vector) onto the x-y plane (phi is not drawn in the figure because of crowding).

From the measured orthogonal fluorescence intensity time traces recorded at the s and p detectors, the reduced linear dichroism, given by *A(t),* can be calculated as a function of time as in eq. (7.1) below:[80,150,152,160-163]

$$A(t) = \frac{I_p(t) - I_s(t)}{I_p(t) + I_s(t)}. \qquad (7.1)$$

A(t) provides a measure of relative change in time of single molecule orientation as projected onto the x-y plane.[56] Significant work has been published with respect to the use of time autocorrelation functions of the linear dichroism to quantify rotational diffusion rates.[111,163-164] In the work presented here, however, the autocorrelation of the linear dichroism function is complicated by the relatively short burst events over which

an autocorrelation can be calculated, due to translational diffusion of the fluorophores into and out of the focal volume.[112,164] Thus the burst event analysis presented in the results and discussion draws conclusions about dye/brush interactions based on the distribution of measured occupation times for highly oriented states, rather than from an autocorrelation of the linear dichroism.

It needs to be noted that while all orientations in the x-y plane are equivalently excited by the circularly polarized excitation light, molecules orient in three dimensions and the absorption efficiency for any particular z-orientation is governed by photoselection rules convoluted with the high numerical aperture (NA) optics in use (NA = 1.45).[161-162] The high numerical aperture (NA) objectives typically used for single molecule fluorescence studies afford collection of photons by the objective over a wide range of incident angles of light, and are thus a means for collecting significantly increased light from what are inherently low light single molecule conditions.[161-162] The angle over which light is collected from the object plane is given by the NA of the objective and the refractive index of the experimental medium as: $\alpha = \sin^{-1}(NA/\eta)$.[161] The effect of the high NA optics is to rotate light propagation vectors, **k**, that are not entirely aligned with the optical axis in object space (polar angle $\Theta \neq 0$), to full alignment with the optical axis in image space ($\Theta = 0$). Axelrod and Forkey show that this process affects the expected $cos^2\Theta$ dependence of the measured intensity and that the mixing of z-component emission into x and y polarization intensities through this use of the high NA optics introduces significant changes to the linear dichroism function, which must be understood when drawing conclusions based on values of $A(t)$.[164]

Figure 7.2.a shows the dependence of the measured intensity on the fluorophore dipole orientation in 3-dimensions, based on the equations derived by Forkey:

$$I_x = K\left(C_1 \sin^2\theta\cos^2\varphi + C_2 \sin^2\theta\sin^2\varphi + C_3 \cos^2\theta\right),$$
$$I_y = K\left(C_2 \sin^2\theta\cos^2\varphi + C_1 \sin^2\theta\sin^2\varphi + C_3 \cos^2\theta\right). \qquad (7.2)$$

In these equations, K is a constant that includes terms that take into account the emission intensity (dependent upon such things as excitation intensity and quantum yield), and efficiency of the detectors. C_1, C_2, and C_3 are terms that account for the mixing of intensity components that results from rotation of the propagation vector as it is passed through the objective.[161-162]

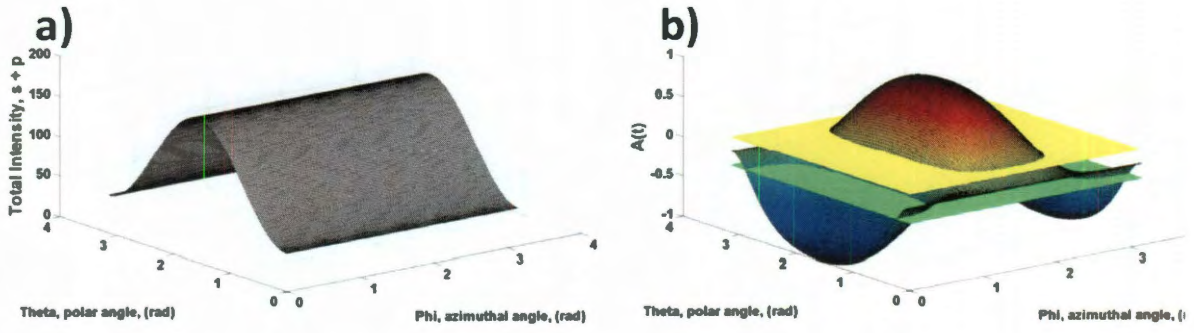

Figure 7.2: a) Measured intensity across 2 orthogonally separated detectors as a function of the orientation of an emission dipole in 3 dimensional space. NA = 1.45, η = 1.5. b) The linear dichroism function, *A(t)*, as a function of polar and azimuthal angle of the emission dipole in 3-D space NA = 1.45, η = 1.5.

Because the measured intensity is a function of the polar angle for these conditions, the linear dichroism expression (equation (7.1)) becomes a function of Θ in addition to Φ. Figure 7.2.b shows the dependence of *A(t)* on Θ for NA = 1.45 optics as used in this experimental system. One effect of the high NA optics is to equalize the

measured intensity across x and y over a range of angles of Θ, and to thus cause the linear dichroism function to approach a value of zero over a range of oriented dipole positions that extends beyond the case at which $I_x = I_y$.

An occupation-time kinetics analysis presented later in this chapter rests upon the assumption that when the linear dichroism function is close to zero, (between -0.18 and + 0.18, marked in the figure via the green and yellow planes, respectively), a molecule is rapidly rotating with a time scale faster than the data collection time resolution. This is because a rapidly rotating molecule will emit many photons in randomized directions within a single data bin-time, and thus signal on both detector channels becomes approximately equal. Because there are also actual orientations that a dipole can adopt for which the linear dichroism is close to 0, it is important to quantify the extent of these values in the linear dichroism function, considering the additional effects imparted by the high NA optics. In this way a measure of the extent of orientated states that are effectively hidden and underestimated in the analysis presented later due to the fact that they present a linear dichroism value near zero are acquired. Integrating the function shown in Figure 7.2.b over both phi and theta for the 1.45 NA optics in use, 43% of oriented states present a calculated value of $A(t)$ that is within $\pm$ 0.18.

7.5 Single Molecule Trajectory Analysis for the Reduced Linear Dichroism

For single molecule trajectory analysis, trajectories of 5 minutes or longer were collected at an excitation power of ~ 750 W/cm^2. These trajectories show a profile typical of a system of diffusing single molecules, with photon burst events separated by periods during which the number of photon counts falls to background levels (see Figure

7.3.a). Trajectories were collected using a photon counting board (Becker & Hickl, PMS400A), at a time resolution of 10 μs. All trajectories were subsequently binned up to 1 ms for event identification. During a 5 minute trajectory a typical number of fluorescence events identified would be 8000 events of varied duration for the dye concentrations and excitation power used. An automated burst analysis software algorithm (MATLAB, R2006a) was built to efficiently sift through the collected data, identify these fluorescence events, and perform calculations. Single molecule conditions were reached by adjusting the dye concentration to a level so that on average, fewer than one molecule were in the focal volume at a time (~ 0.06 particles/focal volume). This was confirmed by ascertaining that at the concentration used for these experiments, the intensity is at background levels (defined as below 5 times the standard deviation of the background signal; the standard deviation was typically close to 1) between 70 and 80% of the time. Following the argument presented by Osborne et al., Poisson statistics predicts that for a 1 fL focal volume, and the ~ 100 pM concentrations used, the focal volume will be occupied by one molecule ~ 6% of the time, by 2 molecules ~ 0.2% of the time, and by no molecules ~ 94% of the time.[165] The likelihood that observed photon bursts arise from only a single molecule is 97% for the system evaluated here.

For the purposes of evaluating single molecule trajectories, an 'event' was identified within the software algorithm as a fluorescence intensity signal of above 20 total counts summed over both detection channels. The signal threshold of 20 counts was established to ensure adequate resolution for the ratiometric reduced linear dichroism expression (equation (7.1)).[159] The excitation power was selected so that a significant number of events at 1 ms binning would reach the required intensity threshold. Note that

at the power necessary for single molecule trajectory analysis, photobleaching of R6G is significant and affects measured diffusion times for the slow diffusion observed at pH 7 within the brush. For this reason, FCS translational diffusion rates are always measured at 10 times lower power density than the burst analysis power used, where effects from photobleaching are no longer evident. The measured event frequency is dependent upon the diffusion rates and the excitation power density.

Background levels within a long trajectory were automatically determined from the trace of each detector channel by an automatic algorithm that calculates the mean of the signal trace after excluding all signal events. The background was subtracted from the signal trace before computing the reduced linear dichroism. Additionally, a correction for polarization differences between the two detector channels arising from the optical system and relative detector efficiencies was introduced to the intensity term for one of the signal channels. This correction was determined from diffusion of polystyrene beads in water, for which a histogram of the reduced linear dichroism should be centered at zero because the measured signal arises from multiple dyes in multiple orientations within freely rotating beads which should result in equal intensity measurements on both channels. This correction factor was calculated daily, and was between 0.885 and 0.960 for all data presented here.

7.6 Results and Discussion

7.6.1 Multiple Modes of Transport in the Polyelectrolyte Thin-Film

a. Diffusion

Figure 7.3 displays several single molecule trajectories, each showing events in which dyes diffuse into the focused laser volume and then exit either through diffusion or irreversible photo-bleaching. Figure 7.3.a shows a trajectory for R6G diffusing in water, and Figures 7.3.b and c show fluorescent burst events for R6G diffusing in the Na PSS polymer brush. The traces shown are for diffusion in neutral solvent conditions.

It is immediately apparent from the fluorescence trajectory that the time spent by an R6G molecule in the focal volume when it is interacting with the polymer brush is significantly longer than the average event times seen in Figure 7.3.a. This is consistent with the measured characteristic diffusion times for the two systems, which are 55 ± 4 μs for R6G in water, and $\sim 300 \pm 60$ ms for R6G in the polymer brush. Note that the traces shown in Figures 7.3.b and c are selected because they are representative of the common characteristics of fluorescent burst events for R6G/PB systems, where thousands of these events are identified and evaluated via the automatic photon burst analysis algorithms. The top panel in each of Figures 7.3.a, b and c shows total photon counts in black. This trace is obtained by summing the signal over both detector channels. The bottom panel displays the signals obtained on the two individual orthogonal polarization detectors. In the summed trace for Figure 7.3.b, a continuously changing intensity profile is evident. Over the experimental time scale, this intensity profile signifies translation diffusion. Because the laser focal volume possesses a Gaussian intensity distribution in x, y, and z,

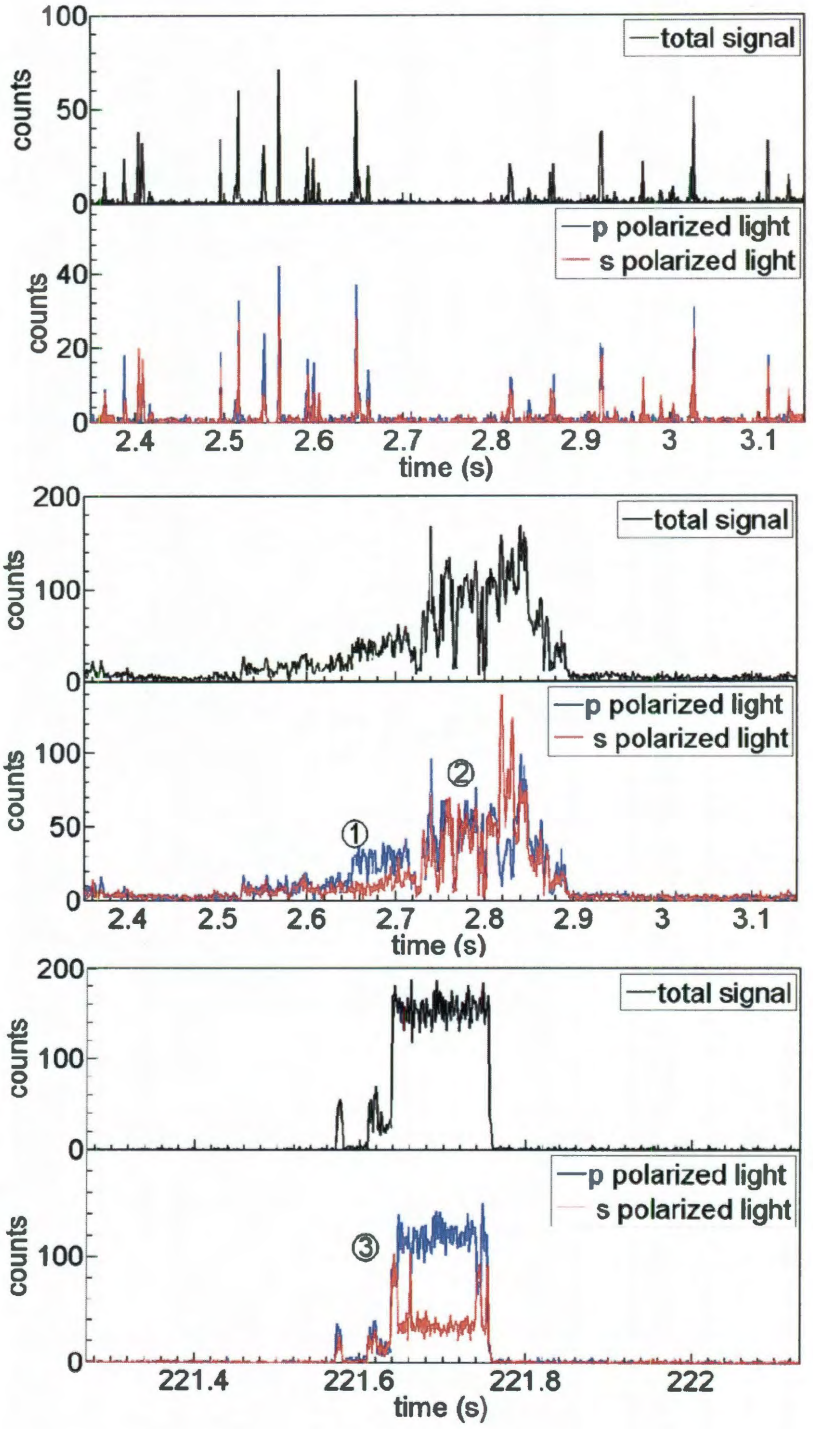

Figure 7.3: Polarization traces for a) R6G diffusing in water, and b) & c) R6G diffusing in the polymer brush at pH 7. The regions labeled 1 and 3 show regions of restricted rotation, and region 2 shows diffusion with non-restricted rotation.

translational diffusion of a fluorophore within the focal volume on the diffusional time scales observed for our system will result in a continuously changing excitation, and therefore emission, intensity profile.

The noise in the short time details of the intensity profile arises because the measured intensity is subject to the randomly distributed location of the fluorophore, both in 3 dimensions and with respect to orientation, inherent to the stochastic nature of the random walk, and because of the expected Poisson distribution for photon arrival times. In Figure 7.3.b, the trends mapped by the total intensity indicate translational diffusion of the probe molecule from the fringes of the focal volume toward the center and away again. In contrast, Figure 7.3.c shows an event in which the total intensity remains steady, indicating adsorption of a dye molecule in the focal volume, followed by probable photo-bleaching.

b. Restricted Rotation

The traces shown as examples in Figure 7.3.b and c show that when R6G interacts with the Na PSS brush there are long periods of time, tens of milliseconds, where rotation of the dye molecules is highly restricted. Clear instances of restricted rotation are seen in the labeled regions 1 and 3, where there is a significant and long lived separation of the measured intensity on the two detector channels. The mean values of $A(t)$ for these two regions are 0.466 ± 0.009 and 0.451 ± 0.009, respectively. For a small molecule rotating faster than the time scale of the data collection, the polarization state would show approximately equal intensity on both channels due to averaged orientation as mentioned earlier (see region 2), with a resulting mean $A(t)$ near zero. For example, at region 2 in Figure 7.3.b, the mean value of $A(t)$ is 0.079 ± 0.009.

For our system, based on translational diffusion times measured by FCS, an estimate of the expected rotational diffusion time for a translationally diffusing molecule in the polymer brush can be made using the Stokes-Einstein-Debye equation:[166]

$$\tau_r = \frac{S}{\lambda}\left(\frac{\eta V_m}{kT}\right) \tag{7.3}$$

Here, S takes into account the rotor shape ($S = 1$ for an ellipsoid), λ is a slip factor, and V_m is the molecular volume. Using the Stokes-Einstein equation and the measured value of the diffusion constant of R6G in the brush at pH 7 (D = 5.5e-14 m^2/s, via FCS) an effective viscosity of the polymer brush of 3.25 Pa s is calculated. For an estimation of the magnitude of the rotational time scale (setting S and $\lambda = 1$,[166] with the molecular volume = 3.29 x 10^{-28} m^3), a rotational time scale of ~ 300 ns is calculated. The fact that rotation is occurring in a highly charged environment means that there are also contributions to rotational diffusion rates from electrostatic interactions, expressed through a dielectric friction term that is additive to equation (7.3).[167] Even for a 100 fold increase in rotational diffusion times, however, the rotational diffusion will be on the order of 10 μs, which is below the time resolution of our data. The recorded intensity at each bin-time can be expected, therefore, to be an average over multiple orientations for molecules that can reorient on this time scale, and thus produce equal intensity. The existence of the highly restricted and long lived rotational modes, then, suggests the presence of local, significantly low energy orientational conformations for R6G in the polymer brush host.

On close examination of Figure 7.3.b a class of interaction for the dye/PB that is of particular interest is observed. During diffusion of R6G in the sodium PSS brush over the period from ~ 2.65 s to 2.71 s (region 1), the total intensity profile is changing, but the

polarization state of the molecule remains highly conserved. The existence of this class of events can arise from two physical motions of the molecule while diffusing in the brush. The first motion that may give rise to changing intensity profiles is slow rotational diffusion with respect to the optical axis (z) occurring on the time scale of the data in question. Because molecular absorption and emission rates are governed by the rules of photoselection,[80] rotation of an absorption/emission dipole with respect to the z axis on this time scale will affect the intensity profile.

The second possible physical cause for the trajectory characteristics observed in region 1 is translational diffusion accompanied by a restricted rotation of the dye molecule. This kind of motion could arise from translational diffusion of dye molecules within regions of bulk solution that are confined to aqueous microdomain channels formed between polymer chains[28,168] where free rotation of the planar R6G molecule is restricted by restricted volume considerations, or from a surface mediated transport of the cationic dye along the length of tethered anionic sodium polystyrene sulfonate polymer strands.[168]

For both cases, a quasi-adsorption state is indicated, characterized by a strong interaction that lies between complete adsorption as seen in Figure 7.3.c where a dye molecule is essentially both translationally and rotationally stationary, and free translation with free rotation, as evidenced in multiple regions of Figure 7.3.b.

c. Polarization State Switching

Another feature exhibited within the polarization trajectories is rapid switching between polarization states during single molecule events, as shown in Figure 7.3.c and Figure 7.4. In Figure 7.4 the switching behavior is highlighted in a plot of the linear

dichroism in the center panel. While the total intensity in these figures indicates that the molecules are essentially stationary, the linear dichroism is observed to switch in discrete

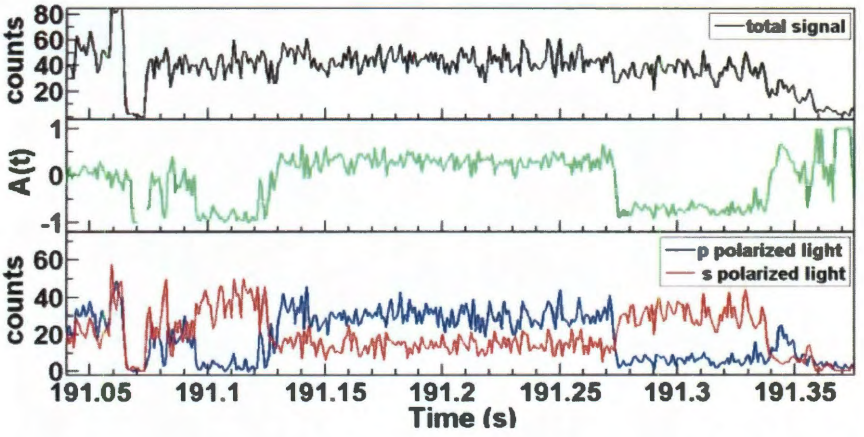

Figure 7.4: Intensity and *A(t)* trajectories for R6G on brush at pH 7, showing repeated polarization state switching of an absorbed molecule.

steps from one polarization state to another, and back again. This behavior suggests that the adsorbed molecule releases from a bound orientation and rotates on a fast time scale below the 1 ms time resolution of our system to a new orientation to 'stick' again. This behavior provides evidence of transitions back and forth between two or three favored low energy orientations.

It bears consideration that not all single event trajectories show smooth or continuously changing intensity trajectories. Many show photoblinking, an instance of which is seen in Figure 7.3.c at about ~ 221.59 seconds, and also discontinuous jumps in intensity at the 1 ms binning employed here, as seen in Figure 7.3.c at approximately ~ 221.64 seconds. A release/rotate/stick model for molecular behavior provides physical grounds for the observed discontinuous jumps in total intensity, where rapid intermittent rotations with respect to the z-axis will give rise to this feature.

d. Summary: Three Modes of Diffusion

In total, the characteristics of the single molecule trajectories presented in Figures 7.3 and 7.4 demonstrate three possible kinds of molecular associations/motions within the polymer brush. These are labeled in Figure 7.3.b and c, and can be classified as: 1) quasi-adsorption consisting of restricted rotation (slow or stationary) with or without translational diffusion, where a trend in total intensity is observed, 2) translational diffusion with fast rotation (faster than the 1 ms time scale), and 3) full adsorption, in which neither translation nor rotation is observed at the time resolution of the data, as indicated by constant total intensity.

7.6.2 Quantifying the Brush-Dye Association

a. Linear Dichroism

To quantify the strong association evidenced in the brush in regions 1 and 3 as periods of highly slowed/restricted rotation, interspersed by free diffusion and rotation (Figure 7.3.b and c), I used a burst analysis algorithm to evaluate the linear dichroism time function.

Figure 7.5 shows histograms of the linear dichroism obtained over all event bin-times in a 5 minute trace of R6G diffusing in water (a), and R6G diffusing in the polymer brush (b). In both cases, there are thousands of focal-volume events evaluated in one 5 minute trace. These histograms are composed only of the values of $A(t)$ during burst events – background is excluded. The width of the histogram provides a measure of how frequently non-zero linear dichroism states are recorded over an entire 1 ms bin-time. To restate, values of $A(t)$ near zero arise from two physical sources when using high NA

optics. $A(t)$ will average to zero for molecules that show rotational diffusion on a time scale faster than the bin time, and will also be near zero for certain orientations of the

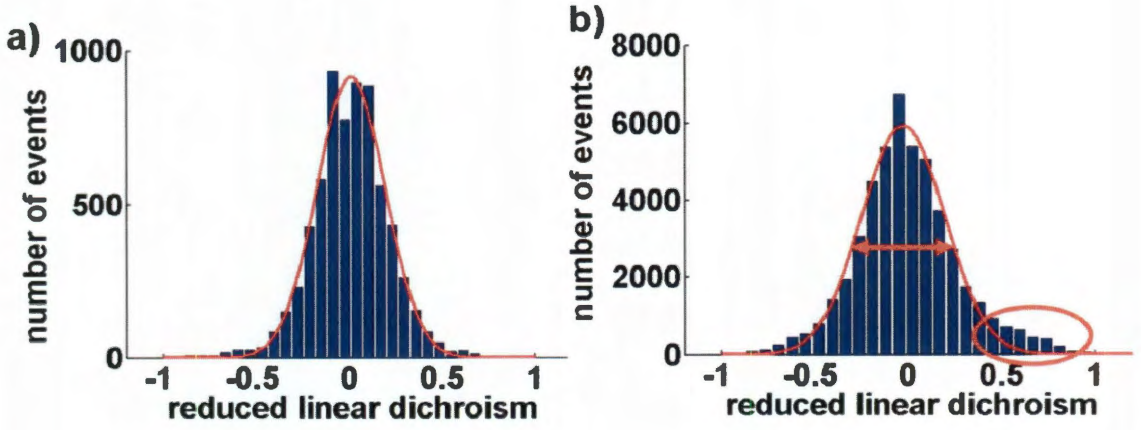

Figure 7.5: Histograms of the linear dichroism across a 300 second trace for a) R6G diffusing in water, and b) R6G diffusing in a polymer brush at neutral pH. The width of the Gaussian fit for histogram a) and b) is 0.203 ± 0.007 and 0.260 ± 0.009 respectively.

molecule in three dimensions, namely orientations in the x-y plane with Φ close to 45° and orientations along z with Θ approaching 0°. As also stated previously, the non-zero values of $A(t)$ reflect the occupation of a highly oriented state over the entire data bin-time. A Gaussian fit of the histogram in a) for R6G in water, gives the spread of values due to noise that can be expected for our system for a single dye molecule with fast rotational diffusion (on the order of 80 ps for R6G in water, via equation (7.3)). This spread is 0.203, with ± 0.007 standard deviation over six 5 minute trajectories. A significant increase in the width of the histogram to 0.260 ± 0.009, and frequently an excess of counts at the wings of the histogram is observed for R6G diffusing within the polymer brush, indicating substantial occupation of highly oriented states. Asymmetry in the histogram, as highlighted in Figure 7.5.b arises from rare strong adsorption events, which are sampled infrequently within the 5 minute time window evaluated.

b. Oriented State Occupation Times

An automated burst dwell analysis of thousands of events was performed to evaluate the focal volume occupation times for oriented and non-oriented states. In Figure 7.6 a distribution of these oriented and non-oriented state occupation times obtained over a 60 minute experiment window is plotted for R6G in the polyelectrolyte brush, using an algorithm that evaluates successive values of the linear dichroism calculated over successive bin-times. For this analysis, oriented states are defined as regions in time over which the linear dichroism is $\geq \pm 0.18$ units from zero. Non-oriented, or freely rotating, states are defined as regions for which the linear dichroism is within 0.18 units of zero. To distinguish distinct orientations, only regions where the linear

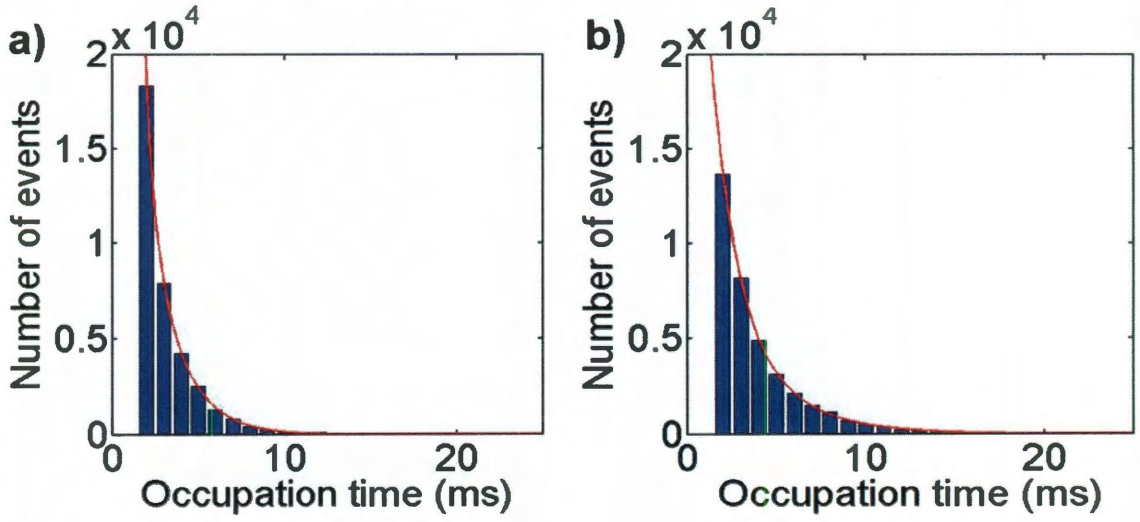

Figure 7.6: Histograms of the occupation times of oriented (in a, values of $A(t) > \pm 0.18$ units from zero) and unoriented (in b, values of $A(t) \leq \pm 0.18$) states of single R6G molecules. A single exponential fit to the data in a) gives a $k_d = 0.6 \pm 0.1$ ms^{-1}, and in b) a double exponential fit gives a $k_{a1} = 0.8 \pm 0.4$ ms^{-1}, and $k_{a2} = 0.27 \pm 0.05$ ms^{-1}.

dichroism is significantly different from zero ($\geq \pm 0.18$ units away) are identified as such because although values at zero reflect a mix of states that are rotationally diffusing and

~43% of the states that are oriented, these two cases cannot be distinguished from the traces of *A(t)*. Figure 7.7 illustrates the algorithm.

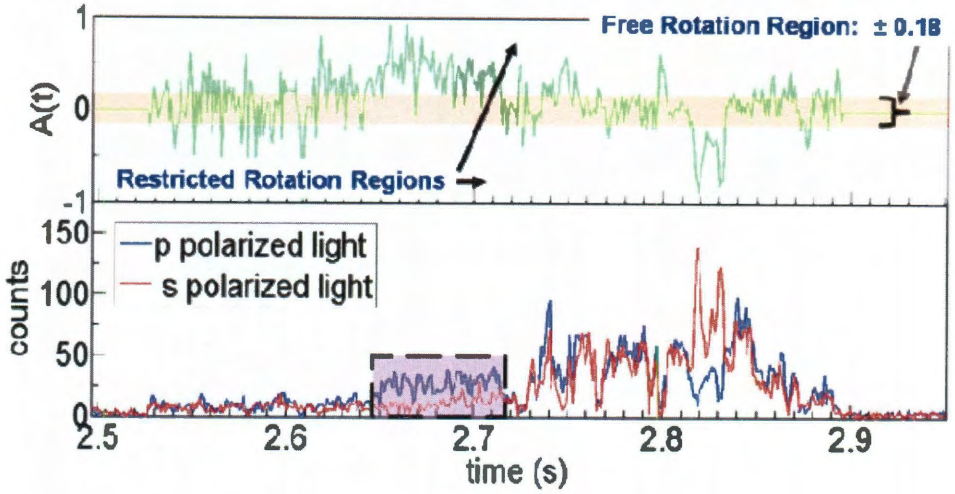

Figure 7.7. Depiction of the oriented state identification algorithm.

Using the algorithm, the occupation times for the two states were established by evaluating the change in the value of the linear dichroism at each time step: if the change in value was less than ± 0.18 from one step to the next, the step was marked as having maintained the previous state, thereby extending the occupation time of the state. The 0.18 metric is taken from the standard deviation of the noise of the linear dichroism for regions in which the linear dichroism averages to zero. The histogram in Figure 7.6.a reports the restricted orientation state occupation times. In the analysis that follows I make the assumption that a state with restricted orientation is a strong association state for R6G and the polymer brush, consisting of either full adsportion or 'quasi adsorption' as defined earlier. The histogram in Figure 7.6.b) shows the occupation times of all free rotation states, which are assumed to reflect weak association states for the dye and polymer brush, where both rotational and translational diffusion within the brush is

observed. I propose that these states are indicative of the reaction scheme in Figure 7.8 below.

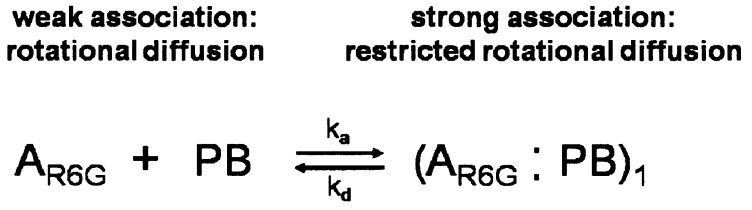

Figure 7.8: Reaction scheme for Dye:Brush interactions.

Performing an exponential fit of the orientation state occupation time histogram in a) returns a single exponent of magnitude 0.6 ± 0.1 ms^{-1}. This gives the associated state k_d, or dissociation rate constant, for this reaction scheme.[169-170] The data in b) is best fit by a double exponential, here giving association rate constants, of $k_{a1} = 0.8 \pm 0.4$ ms^{-1}, and $k_{a2} = 0.27 \pm 0.05$ ms^{-1} ($R^2 = 0.9999$). Given that this distribution contains both non-oriented states, and 43% of the possible oriented states, the rate constants may be assigned as k_{a1} being a measure of the k_d obtained in histogram a, and k_{a2} being the association rate constant for the reaction scheme. The resulting K_{eq} for the reaction scheme is ~ 2, showing that a majority of interactions occurring during transport in the brush are strong associations with restricted rotational motions.

7.7 Conclusions

These single molecule studies reveal heterogeneous modes of transport for charged R6G ions within a strong polyelectrolyte polymer brush matrix, and highlight the dynamic association of the dye molecules with the brush. Significantly restricted

orientation over long periods of time is observed. These restricted orientations, along with the occurrence of rapid switching between polarization states suggests the existence of local low energy non-specific binding conformations available to R6G upon interaction with the polymer brush. Quantitative analysis of state occupation times allowed extraction of rate constants for transitions from weakly associated to strongly associated states for R6G with the polymer brush. It is expected that these characteristics may be selectively enhanced in future informed design efforts for charge storage and bio-mimetic device applications, by adjusting brush parameters such as grafting density, molecular weight, and chemical composition.

7.7 Acknowledgements

I acknowledge Dr. Stephan Link and his group at Rice University, in particular Alexei Tcherniak, for productive, ongoing collaboration and discussion in relation to this work. And I thank both the Texas Center for Super Conductivity and the University of Houston for generous funding of this work.

CHAPTER 8

TRANSIENT 3-DIMENSIONAL ORIENTATION OF MOLECULAR IONS IN AN ORDERED POLYELECTROLYTE MEMBRANE*

8.1 Abstract

The ability to sequester and transfer charge and matter via functionally responsive materials promises to transform the field of electrochemical storage and conversion[3-4,171]. A detailed understanding of mechanisms driving efficient transport in functional materials is growing, and this understanding has already contributed to considerable material improvements[3]. Functional polymers possessing specific chemistry and morphology play a key role in the future of these material applications[28,40,171-172], however, many challenges to optimizing properties still exist due to incomplete descriptions of transport[3-4]. Here, a new single-molecule fluorescence technique is used to reveal the 3-dimensional details of the mechanisms underpinning ion transport in an ordered polyelectrolyte polymer-brush, details that could not be resolved using the more common polarization resolved technique of linear dichroism that tracks changes in orthogonal polarization emission from single molecules, as discussed in Chapter 7. Resolving fluorescence emission over three discrete polarization angles instead,[152] reveals the extent to which these materials impart 3-dimensional orientation to charged guest molecules diffusing in the film. The experiments, supported by simulations, report a global orientation parameter for transport within the films, track coherent dipole angle progressions over time, and confirm the hypothesized existence of significant decoupling of translational and rotational motions for molecules diffusing in the brush.

*This chapter was submitted for publication to *Nanoletters* on December 20th, 2010.

8.2 Introduction

Movement of small molecules and charge through materials is heavily dependent on the molecular and nanoscale architectures extant in these materials. The presence of accessible active surfaces, molecular sized channels, and general orientational vectors, all contribute to transport characteristics[3,28,34-35]. As mentioned in Chapter 2, recent examples highlighting the importance of nanoscale architectures with respect to transport behavior have been published by the groups of Brauchle and Granick, in which divergent diffusion in constrained systems is observed[35-36]. These and other observations inspire the rational design of functional materials to exploit structurally mediated sequestration, transport, and release of charge and matter[3-4,34,40]. Combined with growing understanding of the stimuli responsive, switchable functional properties demonstrated by certain soft surfaces, especially polymer brushes[4], a powerful tool-kit for building functional and tunable materials is being assembled.

Strong polyelectrolyte thin-films are likely to be part of the stimulus-responsive tool kit. While it is known that incorporating nano-scale structural order in polyelectrolyte membranes via polymer brush architecture leads to orders of magnitude increase in charge transport[42], the specifics of the transport mechanisms within these thin films are still sought. By employing 3-angle polarization resolved detection, it is possible to provide a 3-dimensional description of the transport occurring within poly(styrene sulfonate) (PSS) brushes.

John Fourkas first proposed a three component detection system in 2001 as a way to exploit the angle collection properties discussed earlier for high numerical aperture (NA) objectives used in emerging confocal single-molecule techniques[152]. The strength

of this proposed technique, in contrast to 3-D orientation imaging methods[149], is improved time resolution, making the method ideal for evaluating oriented modes of molecules with significant translational diffusion. That it is only now being applied to a translating experimental system is likely because the system under analysis must have sufficiently ordered motion to be distinguished by the analytical algorithms. In this work, millisecond time resolution is achieved, enabling discernment of orientation during transport within the brush. Because model experimental systems with known orientation, diffusion rates, and time scales do not exist[173], demonstrating the inherent information available and limits of this method requires use of simulations to model the physical dynamics of the system. To this end, I developed a Monte Carlo rotation/translation random walk simulation of diffusion, incorporating kinetic state transitions and the ability to define a preferred molecular orientation, to fully describe the experimental milieu and generate model data.

8.3 The Method

The detection scheme used here is shown in Figure 8.1, along with a representation of the molecular environment, the spherical coordinate scheme used, and AFM imaging of a clean coverslip and a PSS treated coverslip from one of the synthesis batches used in this study. In considering the spherical coordinate scheme, the polar angle, Θ, is equal to 0 for a dipole that is oriented along z (the excitation and

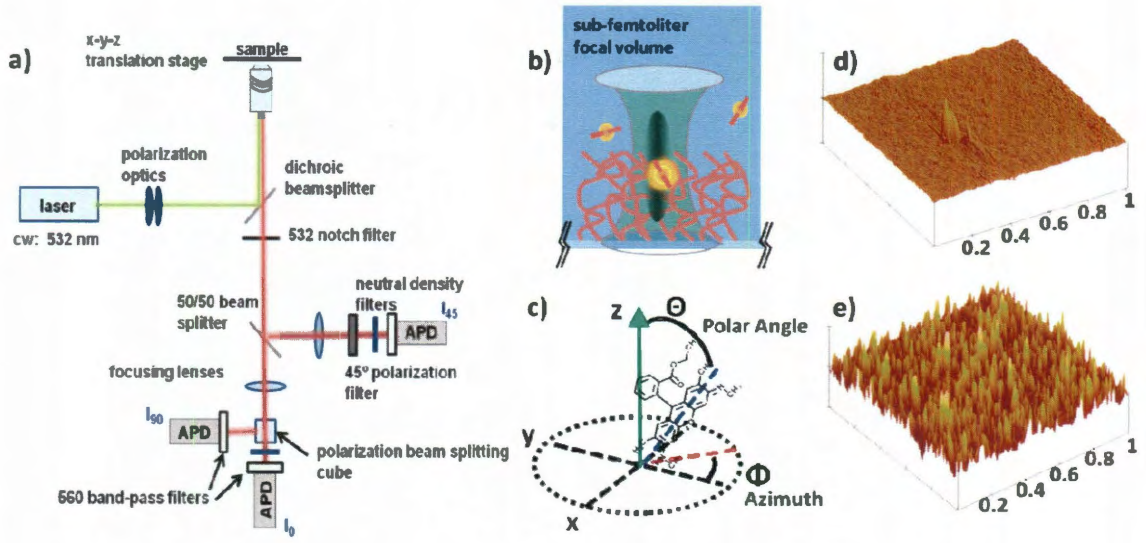

Figure 8.1: Experimental set-up. a) Schematic of epiflourescence microscope with three angle polarization detection. b) Cartoon showing the intersection of the laser focal volume with a polymer brush, and diffusing molecules with emission dipoles depicted (not to scale). c) Coordinate scheme, with R6G and emission dipole (in blue), Capital Θ and Φ, as shown, are the *actual* polar and azimuthal angles, respectively, adopted by a dipole. d) and e) AFM images of the surface of a clean coverslip (d), and a polymer brush modified coverslip (e). The scale in z is 10 nm for the AFM images, and in x and y is 1 μm.

observation axis of the microscope), and Φ represents the azimuthal angle, which is the angle in the x,y plane perpendicular to the propagation of excitation light.

8.3.1 High Numerical Aperture Optics

The premise of the 3-D orientation technique is that high numerical aperture (NA) optics allow determination of the spherical coordinates associated with a molecular dipole. Objectives possessing a high numerical aperture (NA) collect light over a wide range of angles of incident light as discussed in Chapter 7. To briefly review, the maximum angle of collection, α, is determined by the relation $\alpha = sin^{-1}(NA/\eta)$, where η is the refractive index of the experimental medium. High NA optics rotate light vectors that are propagating at high angles (up to the value of α) to align with the optical axis of the microscope/objective[152,161-162].

Absorption of light by a molecular dipole is a function of both the intensity of excitation light, and the orientation of polarization of excitation light with respect to the absorption dipole. With regard to orientation, photoselection rules dictate that $I(\theta) \propto I_o \cos^2 \Theta$, with Θ being the angle describing the difference in orientation of polarization of excitation light to the orientation of the molecular dipole[80]. When a dipole is oriented with $\Theta = 0$ with respect to the polarization of incident light, absorption goes to zero. However, because of the rotation of high angle light caused by high NA optics as described above, molecular dipoles always experience some excitation, even when oriented along the optical axis.

8.3.2 3-D Intensity and Angle Expressions

As a means to exploit this effect, expressions for the intensity measured at three detectors as a function of dipole orientation were derived, in which fluorescence emission is detected over three discrete polarization angles as depicted in the detection path in Figure 1[152]. These intensities are given by:

$$I_0(\Theta,\Phi) = I_{tot}(t,t+\tau)\left(A + B\sin^2\Theta + C\sin^2\Theta\cos 2\Phi\right) \tag{8.1}$$

$$I_{45}(\Theta,\Phi) = I_{tot}(t,t+\tau)\left(A + B\sin^2\Theta + C\sin^2\Theta\sin 2\Phi\right) \tag{8.2}$$

$$I_{90}(\Theta,\Phi) = I_{tot}(t,t+\tau)\left(A + B\sin^2\Theta - C\sin^2\Theta\sin 2\Phi\right) \tag{8.3}$$

The factors A, B, and C are a function of the angle over which a high NA objective collects light, α, and are given by[152]:

$$A = \frac{1}{6} - \frac{1}{4}\cos\alpha + \frac{1}{12}\cos^3\alpha \tag{8.4}$$

$$B = \frac{1}{8}\cos\alpha + \frac{1}{8}\cos^3\alpha \tag{8.5}$$

$$C = \frac{7}{48} - \frac{1}{16}\cos\alpha - \frac{1}{16}\cos^2\alpha - \frac{1}{48}\cos^3\alpha \tag{8.6}$$

Algebraic rearrangement of these derived intensity functions nets equations (8.7) to (8.9) below[152]. Note that lower case θ and φ represent the *calculated* angles from these equations, while capital Θ and Φ represent the *actual* dipole angle adopted by the molecule with respect to the excitation light, as stated earlier.

$$\phi = \frac{1}{2}\tan^{-1}\left\{\left[I_{45}(\Theta,\Phi) - \frac{I_o(\Theta,\Phi)+I_{90}(\Theta,\Phi)}{2}\right]\left[\frac{I_o(\Theta,\Phi)-I_{90}(\Theta,\Phi)}{2}\right]^{-1}\right\} \tag{8.7}$$

$$I_{tot}(t,t+\tau) = \frac{1}{2A}\left[\left(1-\frac{B}{C\cos 2\Phi}\right)I_o + \left(1+\frac{B}{C\cos 2\Phi}\right)I_{90}\right] \tag{8.8}$$

$$\theta = \sin^{-1}\left\{\left[\frac{I_o(\Theta,\Phi)-I_{90}(\Theta,\Phi)}{2I_{tot}(t,t+\tau)C\cos 2\Phi}\right]^{1/2}\right\} \tag{8.9}$$

Figure 8.2 shows the calculated θ/φ space from equations (8.7) to (8.9) as a function of Θ and Φ. The surfaces in Figure 8.2 demonstrate the degeneracy of the

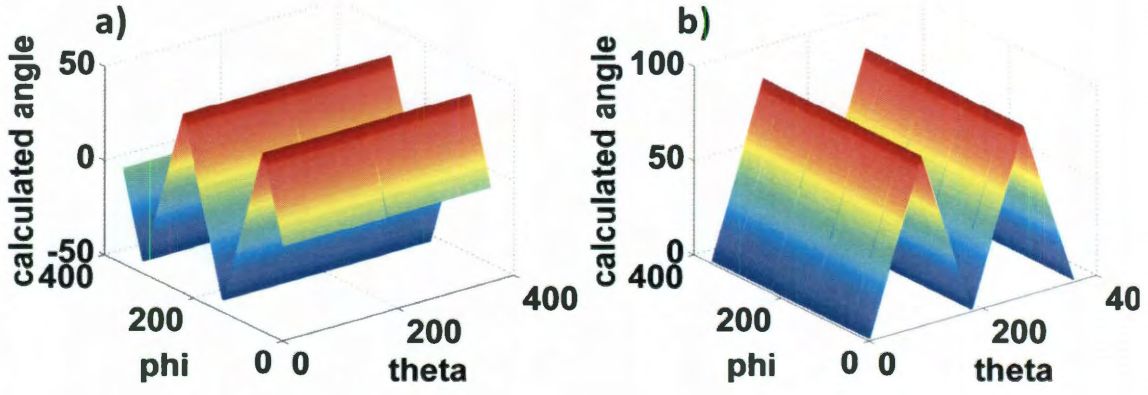

Figure 8.2: Angles calculated from analytically derived intensity traces, using equations (8.7) through (8.9). a) Azimuth angles (φ), b) Polar angles (θ).

angle functions over the entire set of spherical coordinates. This degeneracy affects the reported angles such that a molecule oriented with $\Theta = 0 \pm 30°$ or $270° \pm 30°$ will present as a polar angle, θ, of 30° in the calculated space. In addition, when evaluating the intensity achieved on the individual detectors (see Figure 8.3), it is evident that for values of $\Theta = 0°$ (modulus 180° due to the symmetry of the physical system), the intensity profile is equal on all three detectors (inside shot noise limits for experimental data). An equal intensity profile is also recovered for dipoles rotating significantly faster than the 2 ms time resolution of the data collection because of averaged orientation, as discussed in Chapter 7. Thus, it can be seen that the 3D orientational analysis is not particularly useful for analysis of freely rotating dipoles, or for samples with orientation axes that fall along the optical axis. However, this type of analysis proves to be very informative for systems exhibiting slow translational diffusion with oriented transport.

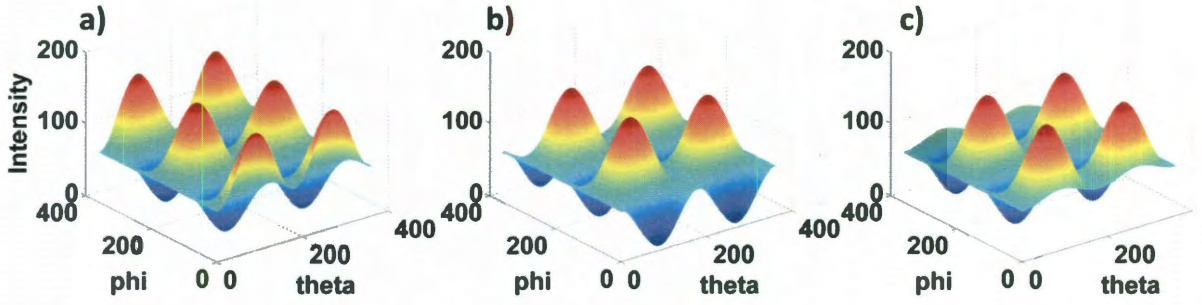

Figure 8.3 Intensity profile across the three individual detectors: a) I_o, b) I_{90}, c) I_{45}.

It is important to note here, that in evaluation of the total detected intensity summed over the three detectors, for $I_{tot} = 600$, the modulation depth, $I_{TLmax} - I_{TLmin}$ at the detectors, does not extend from zero to 600 counts as would be calculated from a straight $\cos^2\Theta$ dependency, but is only equal to ~160 counts for these conditions, because of this high NA rotation of excitation light.

8.3.3 Corrections To The Equations

With respect to applying the algorithms given in equations (8.7) to (8.9) to convert intensities to angles, simulations reveal that meaningful conversion requires careful evaluation of relative intensity strengths at each data point. In Figure 8.4, actual angles, Φ, (part a) and Θ, (part b) sampled during a 5000 step random rotational walk (in blue) are shown, along with a plot of the angles calculated after creating a 3-angle intensity trajectory and converting to φ and θ (in green).

With respect to calculating azimuthal angles, rotation past ± 45 (modulus 90) returns an angle value with opposite sign, which represents as a jump in the angle trajectory, as can be seen for the green trajectory in the highlighted region of part a of Figure 8.4. For determinations based on trajectory behavior then, this angle trajectory needs to be transmuted to a smooth walk using a least-rotation algorithm in which angles

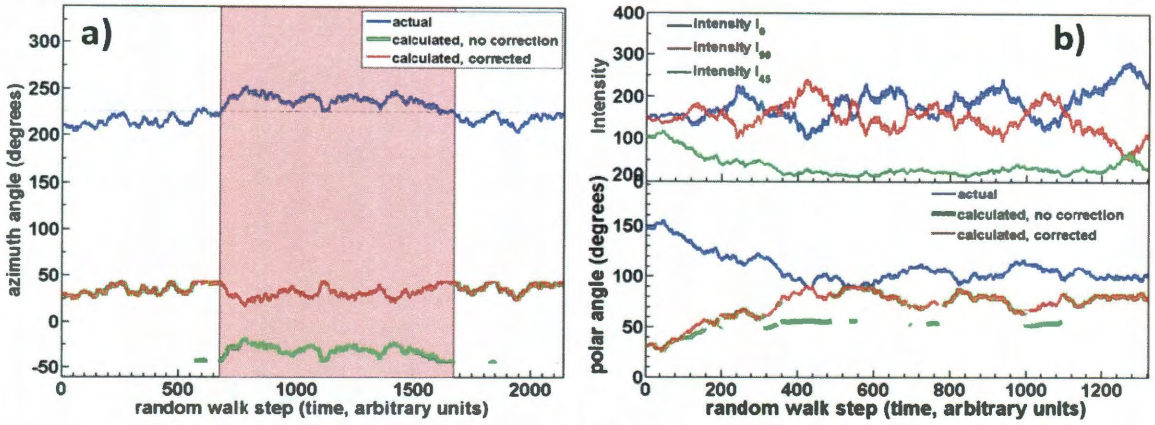

Figure 8.4: Performance of equations in converting from intensities to angles. Actual angle trajectories for simulated rotations are shown in dark blue (bottom panel for the right graph). Calculated angle trajectories are shown in bright green. Corrected angles are shown in red. In a) A least rotation algorithm is applied to calculation of azimuthal angle trajectories to produce corrected angles, and in b) Polar angle traces are corrected by adjusting the input for I_0 and I_{90} for equations (8.7) to (8.9), as described in the text below.

are reflected at the discontinuity rather than passed through[174]. Using this technique the trajectory shown in red can be generated, which represents a smooth walk that reflects the actual walk shown in blue. The least-rotation algorithm moves the calculated angle space to 0 to 90°, from -45 to 45°. For plots of angle trajectories, such as those shown in Figure 8.4, angles are calculated using the least rotation adjustment. Histograms displayed in this chapter, however, are reported using the angles as calculated directly from equations (8.7) through (8.9).

In the case of polar angle calculations, it is apparent from the simulated trace shown in 8.4.b, that the calculations fail for certain regions of the walk (again, shown by the green regions that do not overlay the red). These regions occur under two conditions: 1) when the signal for I_{90} exceeds I_0, and 2) when the polar angle transitions across the 45° value. θ trajectories can be accurately recovered, however, through creation of false trajectories, I_{90F} and I_{0F}. I_{0F} consist of the regions of signal from both I_{90} and I_0 that are the greatest at each time bin, and I_{0F} consists of the regions that are lowest. Using this substitution, correct values of θ are returned, as shown in green in 8.4.b.

As discussed previously, the total intensity of fluorophore emission is dependent upon the location of the fluorphore within the focal volume. A fluorphore near the fringes of the focal volume will have low emission intensity because of the low excitation intensity at the edges of the Gaussian excitation profile. Because of this, it is important to establish the limit for total intensity that is required for accurate conversion of intensities to angles. With respect to these limits, the analytical equations are quite robust. The limits were determined by establishing the intensity at which the equations begin to produce unphysical results. For this purpose, the angle data as shown in Figure 8.2, was

reproduced with varied input intensity values. At the input intensity used to generate the plots in Figure 8.2, where total intensity at the detectors reaches a minimum of 174 counts, angles are accurately reconstructed and only 1.9% of points (2515 out of 130321 total points) cannot be calculated due to values approaching zero in the denominator of equation (8.7). This remains true for values all the way to ~ 12 counts in minimum total intensity at the detectors. Below this limit, while the calculated angles remain accurate, the number of points that cannot be calculated begins to increase slightly (e.g. when a minimum of 7 counts is reached, the number of points that cannot be calculated rises to 2547). The 3D angle expressions are therefore reliable to well below the intensity thresholding limits established for event identification.

8.3.4 Shot Noise and Standard Deviation

Previous work by the groups of David Vanden Bout and Christian Hübner, addresses the affect of shot-noise induced standard deviation in intensity trajectories on the returned angle measurements, θ and φ, as determined via equations (8.7) to (8.9)[173-174]. These groups establish that due to noise in the intensity trajectories, equations become non-convertible for a certain percentage of points, the percentage being dependent on the values of Θ and Φ. For input values of Θ near 0, measured φ values become unstable, with a mean value of around 45° and significant standard deviation. In Figure 8.5, we plot over the entire function space, the standard deviation in calculated angles, θ, and φ, as a function of input angels, Θ, Φ. To generate this plot, input angle vectors are converted to intensity trajectories using equations (8.1) through (8.3), and shot noise is added to the intensity trajectories. Shot noise at each point is calculated as: noise = $I^{1/2} * r$, with r being a random number generated by Matlab's normally distributed

random number generator. θ standard deviation due to shot-noise is < 10% over all space, approaching ~10% only for a limited region of the angle space, while for φ, standard deviation due to shot noise exceeds 20% when Θ is less than or equal to 23°, and for when $\Phi = 45 \pm 2$.

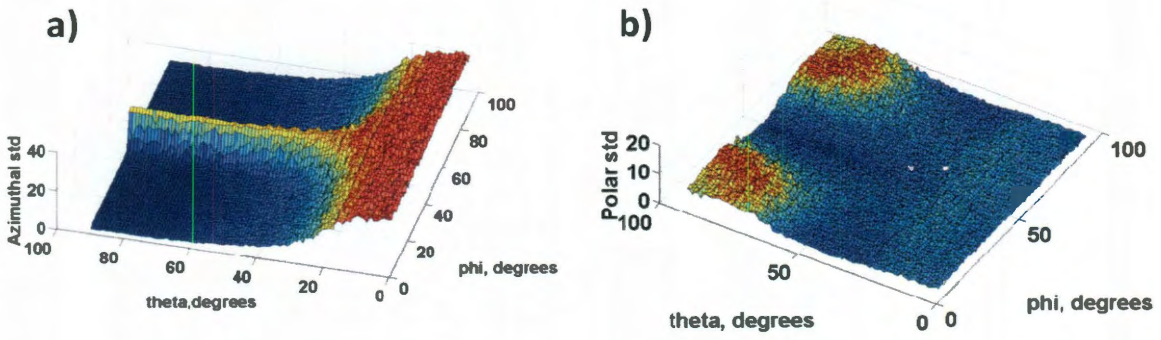

Figure 8.5: Plots of standard deviation in calculated angles derived from intensity trajectories with shot noise added. a) std for calculated azimuthal angles, φ, b) std for calculated polar angles, θ.

8.3.5 Algorithm For Identifying Event Type

An automated algorithm was developed to search for and distinguish oriented diffusion events from non-oriented events in the acquired diffusion traces. The algorithm searches for events by searching for time bins that exceed a total intensity threshold of 3x the mean background level in the samples, providing > 99% confidence that an identified bin is an event and not noise due to background. A time threshold of 5 ms is then used to search for series of bins that are long enough to qualify as an event. When an event is identified using these two thresholding values, the difference in intensity on each set of the detectors is then determined at each successive bin-time within the event time-frame as: absolute value of I_o-I_{90}, I_{90}-I_{45}, and $I_{45} - I_o$. If the value of any one of these differences exceeds the noise-threshold of the estimated shot-noise level of the mean signal strength, the bin-time is classified as oriented, or a Type 2 event, as described in

the subsequent section and identified in Figure 8.6. Angle distributions for the identified oriented and non-oriented events are then evaluated seperately to produce the histograms in Figure 8.6.

8.3.6 Data Binning

Binning of sampled trajectories by a factor of 2 or more reduces the effects of shot-noise by increasing the total signal intensity, however, there is a trade off in reduced time resolution of the data. For slow dynamic processes that occur on time scales exceeding the binned data, this does not pose a significant disadvantage. For our experimental data, data was collected with 1 ms time resolution, and binned by a factor of 2, to 2 ms. This allowed some improvement in signal to noise, without excessive loss of time resolution.

8.4 Results and Discussion

8.4.1 Molecules show preferential orientation in the brush

As discussed in Chapter 7, examination of molecular transport in PSS brushes using a charged molecular dye reveals both heterogeneous diffusion mechanisms as well as strong local interactions with PSS[59]. Diffusion constants in the brush for cationic R6G at neutral pH are ~10^{-14} m^2/s[16,59], and of particular interest, single molecule blip analysis reveals periods of very slow rotation/reorientation, as well as periods of molecular rotation occurring on a time scale faster than the data collection[59].

Data acquired from the 3-detector analysis of transport in the polymer brush is shown in Figure 8.6, with several single molecule diffusion events evident in 8.6.a), which is a data trajectory consisting of photon counts vs time. In 8.6.b) an expanded single event is shown. In this chapter, fast rotation/reorientation, as marked by equal

signal on all three channels is termed 'Type 1,' (as shown in 8.6.b), and oriented periods with restricted rotation, marked by significant inequality among the three channels, is termed 'Type 2.' Type 1 traces here arise from freely rotating molecules and, within this 3-detector method, also result from molecules that are *oriented*, but with Θ close to 0°, while Type 2 events consist of both moving and adsorbed molecules, and are strongly suggestive of Coulombic interactions between the cationic probe and the polyanionic PSS[59].

Using the automated algorithm described in section 8.3.5 to isolate Types 1 and 2 diffusion, it is possible to separate the distribution of angles occupied during these two distinctive transport regimes. Figure 8.6.c shows histograms of calculated spherical coordinates for these two populations over a representative 5 minute diffusion trace, with the purple and red histograms indicating the distribution of Type 1 orientation and Type 2 orientation respectively. The azimuthal angle distribution (left histogram) for Type 1 diffusion shows a relatively smooth profile with peaks at ±45°, and a polar angle distribution centered around low angles peaking at ~23° (right histogram). These values are typical of free diffusional/rotational transport, reflecting angles that correspond to dipole orientations near 0° Θ (recalling that the distribution arises from actual occupation of orientations near $\Theta = 0°$, and also from fast rotation presenting the same intensity profile).

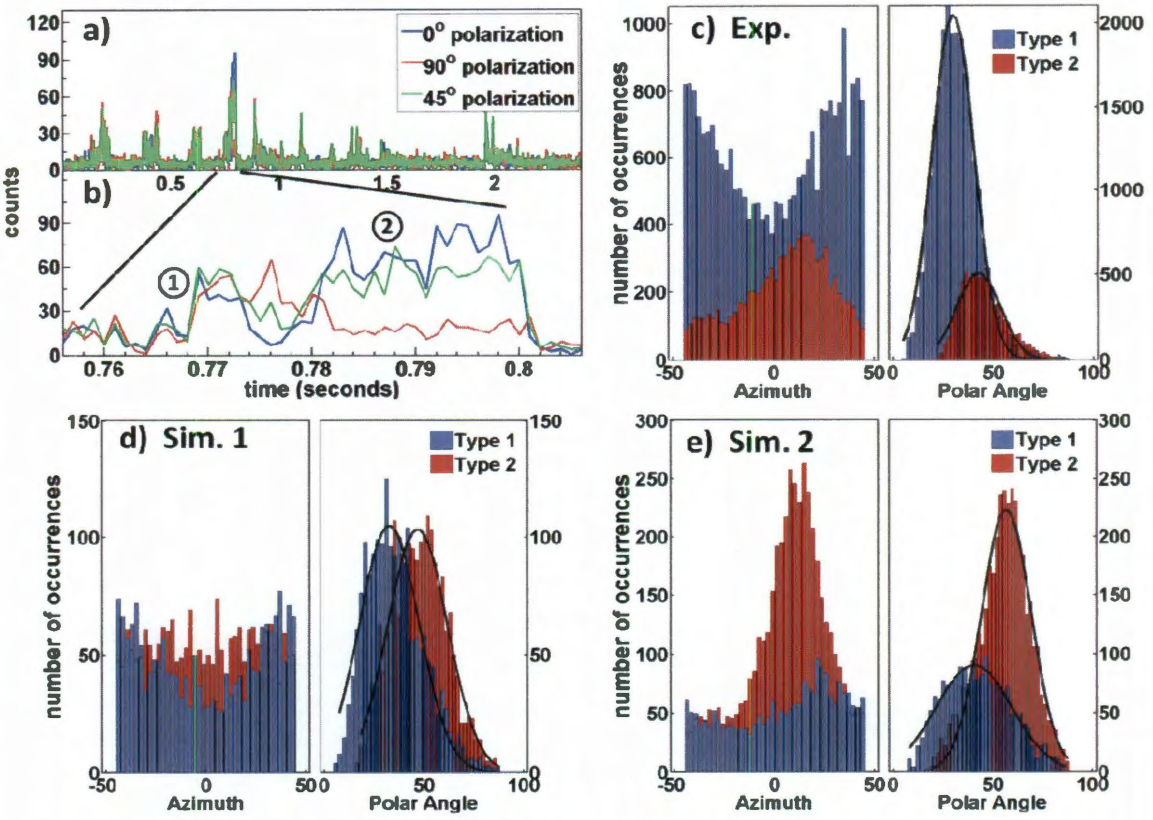

Figure 8.6: a) A fluorescence trace with several single molecule diffusion events for R6G in a polymer brush. b) A close-up of a single molecule transition through the laser focal volume, showing the intensity traces acquired from the three detectors. Region labeled Type 1: Nonoriented diffusion with rotation. Region labeled Type 2: Oriented diffusion with restricted rotation. c) Distribution of R6G azimuthal and polar angles, respectively, sampled in the polymer brush, measured over all diffusion events during a 5 minute period. The two types of diffusion, non-oriented, signified as Type 1, and oriented, Type 2, are shown in the separate purple and red histograms respectively. The polar angle distributions are well fit by a Gaussian. The azimuthal angle distributions hint at a number of subpopulations and fits with up to 4 Gaussians do not converge. d) Distribution of angles calculated for a random walk simulation in which *oriented* transport occurs *without* a preferred orientation vector. e) distribution of angles calculated for a simulation in which preferred orientations of 12° Φ and 65° Θ are introduced. Amplitudes of the histograms are a measure of the number of oriented/non-oriented events in a trace.

In contrast, the distributions obtained for Type 2 diffusion show a distinct, non-uniform profile, with an azimuthal distribution centered at 12° for this brush sample, and a shifted polar angle distribution centered at 39°. This clustering of angle values around

specific values as measured over all *oriented* events suggests a strong preferential orientation for R6G dye molecules that are interacting strongly with the PSS brush. In an isotropic environment, this kind of preferential orientation would not be expected, however, an orientation preference for this particular system can be understood by considering the anisotropic shape of R6G around the transition dipole (Figure 3.5), and the oriented nature of the polymer brush. Both steric and Coulomb interactions between the brush and dye become potential contributors to alignment, on average, of R6G with the brush orientation vector. These interactions can give rise to confined diffusion within naturally formed aqueous channels[29,37], or to strong Coulomb driven alignment of the dye with oriented polymer strands.

To investigate the hypothesis that these results arise from a preferred orientation of the molecules in the brush, experiments were run in a simulated experimental environment, which is discussed in detail in Chapter 9, section 4. Briefly, the simulated space allows both Markovian translational and rotational diffusion, and incorporates an adjustable strength bias to the orientation that can be varied from no bias to 100% biased orientation. Results from these random walk simulations in which there is slow/restricted rotational diffusion are shown in Figure 2.d and e. Results for a simulated system that exhibits restricted rotational diffusion but no *preferred* orientation are shown in 2.d. In this case, Type 2 azimuthal histograms present a flat distribution across all angles, as would be expected, with a population identified by the automatic algorithm as Type 1 diffusion as well.

In 2.e, data is shown for a simulated experiment in which a preferred dipole orientation of 12° Φ, and 65° Θ is introduced. In this case, clear resolution of these

orientation preferences for both azimuthal (φ = 12°), and polar angles (θ = 60°) is observed. Azimuthal angle identification is accurate, with the polar angle distribution shifted by 5°, due to partial limitation in the function space[174], and shot-noise as discussed previously. The results of these simulations support a hypothesis that Type 2 transport in the brush occurs in the presence of an orienting potential.

Figure 8.7 shows angle histograms obtained for a representative sample from each of two brush syntheses evaluated in this work. Manual evaluation of the distributions of azimuthal angles show populations centered at 15° for Brush 1, (in a) and 3° and 15° for Brush 2 (in c).

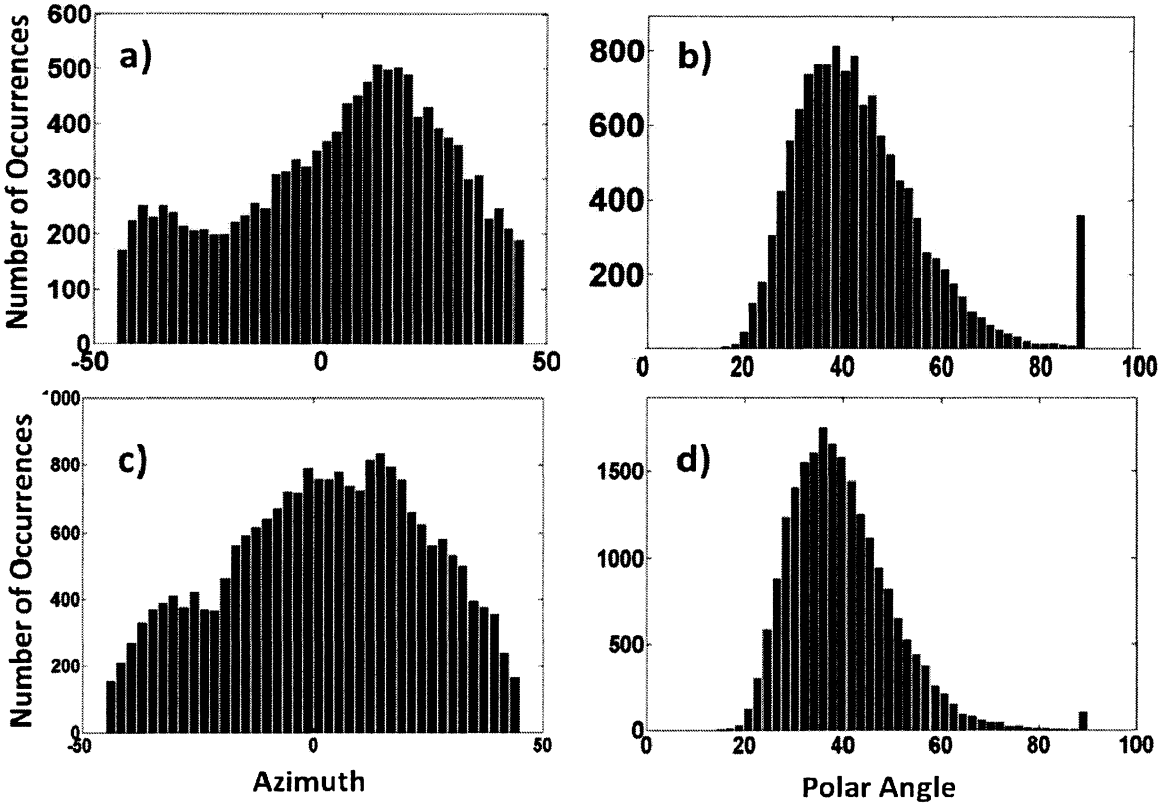

Figure 8.7: Histograms showing distributions of oriented azimthal and polar angles for a) and b) brush sample 1 (trial 3), and c) and d) brush sample 2 (trial 2).

The distributions hint at several subpopulations, however the resolution of the histograms prohibits a quantitative determination of these from a Gaussian model. Fits to models of from 1 to 4 Gaussians do not converge.

To determine the mean location of polar angle distributions, the histograms can be approximated with a Gaussian fit. The mean location for the polar angle distributions do not show significant changes over all experimental measurements taken, however, as is evident here, the width of the measured distribution is significantly smaller for the second brush sample in 8.7.d. The width of the polar angle histograms over all of the Brush 1 trials is 29 ± 1° and for Brush 2 is 21 ± 1°.

Table 8.1 summarizes the statistics and angle preferences measured for the 2 brush syntheses evaluated, over multiple sampling periods/locations on the brush surfaces. The data demonstrate the ability of the method to identify significant variance in transport characteristics in the two brushes.

Sample	trial	# event bins	% Oriented	Num oriented bins	Preferred ϕ		Preferred θ
Brush 1	1	68221	23%	15691	12	—	40
	2	51887	24%	12453	15	—	39
	3	49948	25%	12487	12	—	38
	4	62013	22%	13643	15	—	37
Brush 2	1	163191	4%	6528	6	—	39
	2	132168	8%	10573	8	—	35
	3	275139	8%	22011	3	14.6	36

Table 8.1: Oriented diffusion statistics over two brush syntheses. For Brush 1 (48 hour monolayer), on average, 24% of events were oriented, while for Brush 2 (32 hour monolayer), fewer than 10% of events were oriented. The mean angle locations in Brush 1 are 14° (azimuth), and 39° (polar angle), and for Brush 2, are 6° (azimuth), and 37° (polar angle). Locations across the brush surfaces were selected from within a 10 μ area.

8.4.2 Time-dependent 3D orientations

The 3-detector method enables exploration of the time progression of rotational diffusion. In evaluation of time-dependent behaviors, it is possible to resolve

reorientation characteristics of translating molecules in comparison to stationary molecules, and in doing so, periods of slow oscillation during single molecule diffusion events are revealed.

Time progressions for several events in the PSS brush are shown in Figure 8.8, as well as for stationary molecules embedded in spin-cast PMMA. Molecules in the PMMA film are translationally stationary at room temperature and exhibit only very slow rotation[149]. Traces for PMMA (left) and PSS (right) are shown in Figure 8.8, a and d. The histograms, (b, e), show polar and azimuthal angle distributions measured over each

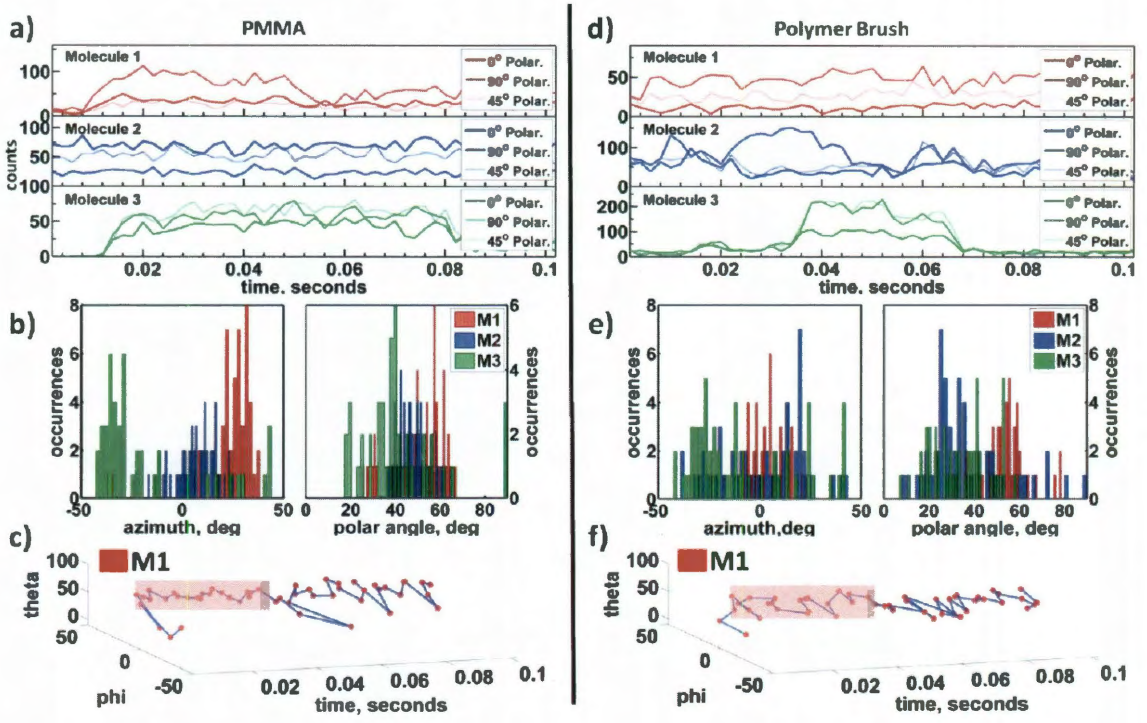

Figure 8.8: (left) Data for 3 different single molecule events for R6G embedded in PMMA is shown, a) intensity traces, b) distributions of sampled angles for the three molecules, c) a scatter plot for the top trace in a over the time course shown. (right) Data for R6G single molecule events in polymer brush, with intensity traces, angle distributions and scatter plots in d-f). The highlighted region in part c) shows a portion of the trajectory from which the maximum standard deviation due to instrument noise can be estimated. The highlighted region in part f) shows a region of oscillation.

of the events. As expected, the angle distributions are narrower for the highly rotationally-restricted individual molecules in PMMA, than for the diffusing molecules in the PSS brush. The PMMA control experiments demonstrate the ability of the optical system to resolve azimuthal angles over the entire 90° range. The range of polar angles returned, evaluated over 28 PMMA single molecules (data not shown) extends across a range of $\sim 10 < \theta < \sim 75$.

Parts c and f of Figure 8.8 show time progressions of molecular orientation for the traces in the top panels. From the PMMA time progression in c (highlighted region), a 56 ms span is observed during which the probe is stationary, and θ and φ fluctuate by ~ 5% (mean values: $\langle\theta\rangle = 6.2°$, $\langle\varphi\rangle = 56.9°$). Over several ~ stationary rotation regions in multiple PMMA embedded molecules, the experimental noise limits of our angle resolution can be obtained, and was calculated to be ± 5° for angles from $-45° < \varphi < 45°$ and $23° < \theta < 75°$.

Regions of dipole movement that extend beyond noise limited fluctuations can be attributed to dipole re-orientation. In the case of the PSS measurements, multiple instances were observed in which there is transient oscillation of dipole orientation in theta/phi space during strong interactions, as illustrated in the highlighted region in f. This region shows a period of 56 ms over which oscillations occur with an approximate period of 9 ms. A possible origin for such transient oscillation may be transient occupation of local energy 'metabasins' in the structure.[175-176]

This kind of behavior is evident in a subpopulation of diffusion events, and can be illustrated more clearly within Figure 8.9 where the polar and azimuthal angle axes are separated. Here intensity traces are in the top panel, azimuth angles in the center panel,

and polar angles in the bottom panel. A shaded region for each angle trajectory which highlights an area that is 2* the shot noise limit of 5° (establishing 95% confidence bounds), centered around the mean value is also plotted. For the two different examples shown here, oscillation of the polar angle around the mean value, outside the 95% confidence bounds shown by the shaded area, is clearly evident.

Periodicity for these two regions can be estimated at ~ 9 ms and 14 ms for a) and b) respectively. Noise dominates discrete FFT analysis of the individual events due to the short trajectories, making an analytical evaluation unavailable for individual events.

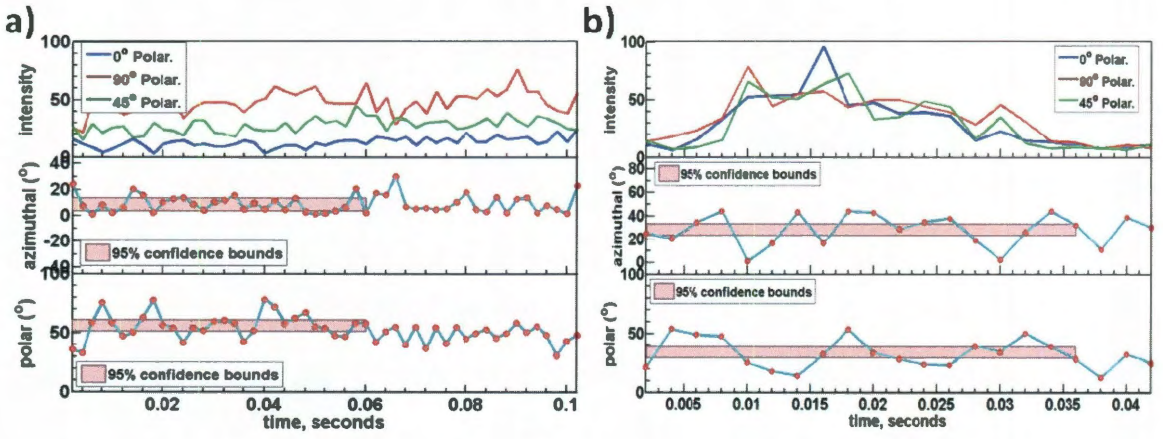

Figure 8.9: Two single molecule diffusion events, with associated polar angle, θ, and azimuthal angle, φ, shown. The shaded region isolates 2*shot noise limited detection around the mean angle values over the region. In both of these examples, periodic polar reorientations around the mean are evident.

8.4.3 Molecular motion during strong interactions: Translation with restricted rotation

Detection over three polarization angles also allows clarification of the mechanisms underpinning Type 2 transport of oriented molecules. This information

arises from evaluation of the total detected fluorescence intensity at each time bin, $I_{tl,em}(t) = I_0 + I_{90} + I_{45}$. As discussed previously, $I_{tl,em}(t)$ is a function both of location within the Gaussian intensity profile of the excitation volume, and dipole orientation with respect to the propagation direction of excitation light. Time dependent changes in intensity can thus arise from either translation or slow rotation within the excitation volume. These dependencies, and equations expressing them, are illustrated in Figure 8.10.a and b. A careful evaluation of concurrent time dependence of polar angle and total intensity reveals oriented translational transport within this system. This is possible to discern because there is a limit to the possible magnitude of change in total intensity due to rotation only.

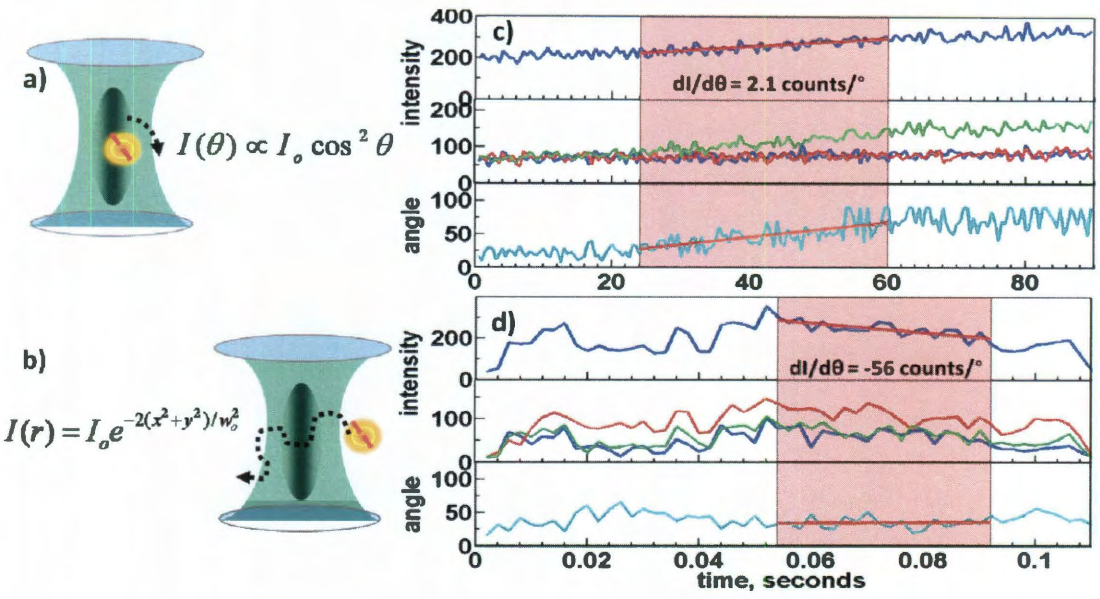

Figure 8.10: Evaluation of change in intensity with respect to changes in polar angle. a) and b) are representations of the separate processes upon which intensity is dependent: a) rotational diffusion within the focal volume, b) translational diffusion through the focal volume. c) analytically generated traces for a rotating dipole moving in 0.5 degree steps from $\Theta = 0$ to $\Theta = 90$. The top panel shows the summed intensity measured over the three detectors. The center panel shows the individual detector signal (shot noise has been added), and the bottom panel shows the θ calculated from the traces shown in the center panel. d) Intensity profiles and calculated θ for experimental data, with a region of ~ continuous intensity change highlighted in both the total intensity and polar angle plots.

This limit to the magnitude of change in $I_{tl,em}(t)$ that can be attributed to rotation only can demonstrated with simulated traces. Plotted in Figure 8.10.c are intensity traces (center panel), polar angle (bottom) and a total intensity (top) for a model dipole rotating smoothly in 0.5 degree steps from $\Theta = 0°$ to $\Theta = 90°$, with shot noise added[152]. This trace is generated with $\Phi = 45°$ and with summed intensity at the detectors of ~ 200 counts, to match experimental intensity. A linear fit to the highlighted region of the trace yields $dI/dt =$ 2.3 counts/s and $d\theta/dt$ = 1.1 °/s. Taking the ratio of the two derivatives yields change in intensity with respect to changing polar angle: $dI/d\theta$ = 2.1 counts/°. This is thus the maximum change in intensity achievable due to rotation. Note, that Figure 8.10.c (top panel) illustrates the feature of the high NA optics that even for Θ = 0°, significant excitation still occurs[152,161-162], resulting in reduced modulation depth and limiting the maximum value of $dI/d\theta$[152,161-162]

Figure 8.10.d shows representative results for an R6G diffusion event in polymer brush. In this example I identify a region in which there is a largely continuous drop in total intensity (top panel) accompanied by significant orientation (center). The $dI/d\theta$ for this region is -56 counts/°, significantly higher than the maximum $dI/d\theta$ that can be attributed to rotation only. This measured change in intensity in excess of that arising from rotation can be attributed to translational motion within the focal volume during this strong, oriented interaction.

In this case, enhanced translational diffusion with respect to rotational diffusion within a single event is witnessed, which is a strong indicator of dynamic heterogeneity[20,175,177] or spatially confined diffusion[29,35,37]. Data evaluating multiple oriented single molecule events reveals that ~¼ exhibit translation without significant

reorientation. This analysis can be found in table 8.2 were evaluation of the first 30 consecutive events for which the intensity threshold exceeded 30 counts in the diffusion trace for polymer brush synthesis 1, sample 1 is compiled. The analysis yields 14 events that contain significant periods of measurable orientation. Six of the fourteen events show $dI/d\theta > 6$ counts/°, which is ≈ 3* the value of $dI/d\theta$ that can be expected for a rotation only mechanism. Five show $dI/d\theta \leq 6$ counts/°, with three showing an effective change in total intensity ≈ shot noise. These last three may be classified as adsorption events because there is no discernible change in intensity. Values for the remaining three events could not be calculated due to discontinuity in calculated theta values.

Oriented Event Number	Intensity Trend Time Span	dI/s	dtheta/s	di/dtheta	Int change/shot noise	Note
1	18	-7	1	-5	-8	
2	8	-13	0	-213	-7	
3	10	18	3	12	12	
4	12					cannot calculate
5	6	-2	-2	2	-1	adsorption
6	8					cannot calculate
7	12					cannot calculate
8	22	0	1	1	1	adsorption
9	8	16	5	-7	0	
10	26	-3	0	-6	-6	
11	8	0	-2	0	0	adsorption
12	14	6	3	4	6	
13	16	-4	1	-8	-5	
14	12	7	1	12	8	

Table 8.2: Tabulation of $dI/d\theta$ evaluation for 14 single molecule diffusion events that show regions of oriented transport.

8.5 Conclusions

In summary, the use of three angle polarization resolved fluorescence detection, combined with simulations of the experimental milieu makes possible the identification, quantification, and classification of oriented translational diffusion mechanisms occurring

in strongly interacting systems. This analysis has revealed the existence of oriented translational movement within a PSS polymer brush, and identified a global orientation parameter defining a preferred orientation for guest molecules in the membrane. Having demonstrated that it is possible to quantify decoupled rotation/translation in ordered polyelectrolyte membranes, future efforts can be directed to developing an understanding of the relationship between this decoupling and the local order within the brush system.

8.6 Acknowledgements

I acknowledge the NIH for funding for this project through Molecular Biophysics Training Grant (T32 GM008280). I also thank the following individuals for providing insight and productive conversation with respect to this work: Dr. Stephan Link, Dr. Anatoly Kolomeisky, Dr. Wei-Shun Chang, and Alexei Tcherniak.

CHAPTER 9

MONTE CARLO SIMULATIONS*

9.1 Abstract

Simulations of random walk processes have been established as an excellent model for real world diffusion processes,[108-109,117-118] and have thus been employed in this work to help provide physical insight into the factors affecting transport in the polymer brushes. Random walk models were utilized in the work of Chapter 5 (*FCS: Criteria for Analysis in Multi-Species Systems*), Chapter 6 (*Diffusive Transport in Poly(Styrene Sulfonate) Polymer Brushes*), and Chapter 8, (*Transient 3-Dimensional Orientation of Molecular Ions in an Ordered Polyelectrolyte Membrane*). The details of all three random walk simulations are included in this chapter as important background, however it is the random walk models of sections 9.2 from Chapter 6, and 9.4 from Chapter 8 that comprise my thesis contribution.

All of the simulations were constructed to mimic fluorescence spectroscopy experiments by insertion of diffusing particles in a sample volume in which a laser focal volume was also placed. This allowed generation of intensity traces for analysis by the methods of Chapters 5, 6 and 8. In the cases covered in sections 9.2 and 9.4, the random walk models were constructed with a tunable diffusion bias by including the presence of external fields.

In the case of section 9.2, (Chapter 6), the random walk model was constructed to investigate the effect of a spatially periodic Coulomb field on a translational random walk and the resulting FCS autocorrelation function. The simulations demonstrate that

*Much of the content of this chapter has been published as Supporting Information for the articles published from chapters 6 and 8.

stronger Coulomb fields slow diffusion significantly, and that this can be resolved via autocorrelation analysis. In section 9.4 (Chapter 8), the random walk model is constructed with an orientation dependent bias, and is used to investigate the hypothesis that the experimental results arise from the existence of a preferred orientation for diffusing dye molecules within the brush.

All programs were written in Matlab, using versions R2006a and higher.

9.2 Details of the Random Walk in a Spatially Periodic Potential Field

This model was constructed as a 2-dimensional random walk in a spatially periodic potential field. The potential field experienced by each particle during a random walk was constructed from a series of point charges placed on a grid with a spacing of 1 arbitrary unit. The potential field was of the form:

$$u(r_{ij}) = \begin{cases} \xi_i \dfrac{Z_j}{r_{ij}}, r_{ij} \le r_{\text{lim}} \\ \\ 0, r_{ij} > r_{\text{lim}} \end{cases}, \qquad (9.1)$$

where ξ is an interaction constant that includes terms for charge on the diffusing particle, solute dielectric constant and temperature; Z is the variable field strength; and r_{lim} is a cut-off radius limiting the electrostatic field due to point charges far away from the regions through which the counterion diffuses. Distances traveled by a particle were proportional to the magnitude of the force experienced by the particle at each step. This was equal to:

$$F_i^{total} = F_i^B + F_i^{PF}. \qquad (9.2)$$

F^B was a constant magnitude random Brownian force proportional to a 0.24 unit step, and F^{PF} was the total force due to the potential field at position i: $F_i^{PF} = \sum_j^n \frac{du(r_{ij})}{dx}$. The summation was made over all potential well points within a radius equal to r_{lim}, which was set equal to 2.1 units. Drag and excluded volume effects were neglected.

The direction of each step was randomized by selecting a random angle in the range from 0 to 2π to define the step vector direction. This random angle was generated using the uniformly distributed 'rand' function in Matlab to generate a random number which was multiplied by 2π.

Potential field forces approach infinite magnitude at distances very close to an individual potential well. Motion of the particle was stopped at the potential well when forces resulted in steps exceeding the distance between the particle and the well. In this circumstance, the random walk was continued from the location of the well with contribution from a random Brownian step only, since all potential field forces sum to zero at the position of the well.

The entire field was 16 units in diameter. Signal trajectories were recorded for particle motions occurring within a 10.4 unit diameter area centered in the field. The presence of a particle in this modeled focal volume contributed a constant signal value. Up to 6 random walk particles were followed at once. Random walks were conducted over 200,000 steps.

Autocorrelation analysis was subsequently performed on the generated signals.

9.3 Details of the 3 Dimensional Random Walk with Two Species

In this model, diffusion was modeled via a random walk in 3 dimensions.[108-109,117-118] At each time step, particle position was moved a random and uncorrelated distance along each of the x, y and z-axes. The magnitude of the step in each direction was selected from a uniformly distributed range defined using the Matlab R2006 built-in random number generator, that extended over ± a maximum specific step size. The simulated sample volume consisted of a rectangular box, extended along the *z*-axis, with periodic boundary conditions. A 3D Gaussian intensity profile was used to model the focal volume of the laser, with a ratio, r_0/z_0, of 0.1, to approximate experimental conditions (see Figure 5.4).

At the beginning of each simulation, 10 particles were randomly distributed throughout the sample volume. For two species simulations, two kinds of particles were defined by establishing a different maximum step length value within the uniform step-length distribution. For the work presented in this thesis, these step lengths were 25 nm and 79 nm for the slow and fast diffusing particles, respectively. These step lengths were chosen because of the clear visual effects apparent in the autocorrelation function as parameters were varied. Additional simulations conducted over a variety of step length values confirm the effects on autocorrelation function fitting throughout the lag time regions covered.

Simulated fluorescence from each particle was computed as the value of the Gaussian intensity profile at the position of the particle:

$$F(x,y,z) = a \cdot \exp(-\frac{2(x^2+y^2)}{r_0^2}) \cdot \exp(-\frac{2(z^2)}{z_0^2}), \qquad (9.3)$$

where $r_0 = 2\sigma_1$ (2 times the standard deviation of the Gaussian in the xy-plane), and $z_0 = 2\sigma_2$ (2 times the standard deviation of the Gaussian along the *z*-axis). The focal volume r_0 value was set to 250 nm. The overall fluorescence signal trajectory as a function of step was computed as the sum of individual particle fluorescence values at each step of the simulation. These fluorescence signals were created assuming no photophysics and 100% fluorescence quantum yield. To better approximate the experimentally observed conditions, random noise was added to the random walk fluorescence transient after the transient was generated.

Simulated trajectories were run for 10^6 steps, yielding the equivalent of a 10 second trace, assuming a 10 us bin time. Ten trajectories were collected to allow

adequate averaging of the autocorrelation functions calculated over these 10 second traces, yielding a 100 s sampling time. It was verified that the fit quality of the autocorrelation function averaged over 100 seconds was sufficient by comparing the quality of the fit to curves constructed from over 100 averaged trajectories, or 1000 seconds. The fit quality was equivalent. It is thus confirmed that for sample volume dimensions of 6 times the $1/e^2$ intensity radius of the Gaussian signal, and for 10 particles, averaging over 10 trajectories was sufficient for the autocorrelation function to converge to a constant value that was well-fit by the standard autocorrelation expression. On the other hand, it was observed that for both too small sample volume dimensions and inadequate averaging times, the autocorrelation fitting at large lag times showed a faster decay region that could not be well fit[117].

Having the complete fluorescence transient from the simulation, subsequent autocorrelation analysis was carried out in the same manner as described for the experimental data in Chapter 5.

9.4 Details of the Translational/Rotational Random Walk with Preferred Orientation

This Markovian random walk simulation of the experimental milieu was written in MatLab R2009b. This simulation was designed to take into account three processes occurring in the sample:

1) Time dependent kinetic transitions back and forth from strongly associated to weakly associated states, according the scheme:

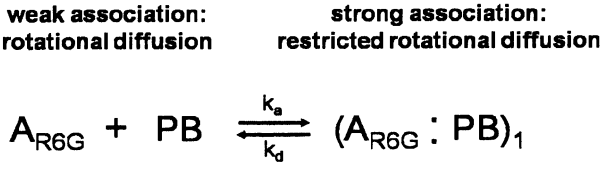

2) Translational diffusion, and consequent interaction with a modeled laser focal volume.

3) Rotational diffusion, also with interaction with the laser focal volume.

The simulation was constructed to enable both translational and rotational diffusion rates to be dependent on the kinetic state occupied by each simulated molecule at each time step.

At initiation, a variable number of single molecule dipoles (6 for the simulations reported for the work of Chapter 8) were established at random locations and with random orientations within a rectangular sample volume. In the center of the sample volume, a region over which a 3D Gaussian intensity profile extended was established to serve as a laser focal volume, see equation (9.3), and Figure 5.4.a. The number of molecules was selected with the same consideration as applied to experimental conditions: this number was selected to assure enough diffusion events through the focal volume to acquire good statistics, given established diffusion rates (as described below), while maintaining less than one molecule on average in the focal volume at a time. At the initial time step, the active kinetic state was set to the weakly interacting state indicated in the scheme above, with corresponding factors in the translational and rotational diffusion terms.

Each following random walk step, step(t_{i+1}) was preceded by a kinetic transition query according to $P_{tr} = 1 - e^{-kt}$, where P_{tr} is the probability of a transition, k is the kinetic rate constant, and t is the simulation time bin[178]. The kinetic rate constant for this determination is dependent on the identity of the state occupied at step (t_i), according to the scheme shown in step 1 above. A state transition was executed for $P_{tr} > rand$, with

rand being a random number drawn from MatLab's uniformly distributed random number generator[178].

The probability of a rotation was determined sequentially for Θ and Φ, the spherical angle coordinates representing the angle adopted by the molecular dipole. A directed impact at each step was first established with 50% probability of being directed to positive or negative rotation (via generation of a random number drawn from a uniform distribution). The kinetic energy level of the impact was drawn from a Boltzmann distribution (equation (9.4)) by generating an exponentially distributed random number as a probability measure.

$$P_{thermal,i} = g_i e^{-E_i / K_B T} . \qquad (9.4)$$

Here, g_i is taken as = 1. Potential energy in the system to express a preferential alignment was also introduced, with an exponentially decaying probability function dependent on orientation of a dipole with respect to an adjustable orientation direction, Γ, according to the following, with OC being an order constant expressing the strength of the alignment field:

$$P_{PE,i} = \frac{e^{-(1-\cos^2 \gamma_i)_i * OC * \sin \gamma}}{\sum_i e^{-(1-\cos^2 \gamma_i)_i * OC * \sin \gamma}} . \qquad (9.5)$$

In equation (9.5), $\gamma = |\Gamma - \Theta|$.

At the outset of each simulated experiment, an adjustable measure, $P_{thresh,}$ representing the threshold of a barrier to rotational movement for the system was set. This term represents forces hindering rotation, arising from effective solvent viscosity.[179-180] Ranges for the value taken by this term were established empirically from the

performance of the simulations. Finally, for $|P_{thermal,i} * P_{PE,i} > P_{thresh}$, a rotation was executed. Rotations occurred in discrete steps, which were set to 1° for the simulations presented here.

The time step in the simulation was set to 10 μs, with data subsequently binned to 2 ms for analysis. The time resolution of the steps was selected so that upon binning to experimental time resolution, signal for molecules with fast rotation rates could be well averaged, resulting in equal signal on the three channels outside of noise limits. Unbiased rotation could be established by setting $OC = 0$. The fastest rotation rates were established by setting P_{thresh} equal to 1. An example of an event from a trajectory generated from the fast rotation of an unbiased rotating dipole, binned to 2 ms is shown in Figure 9.1.a. Note that noise has been added to the trajectory.

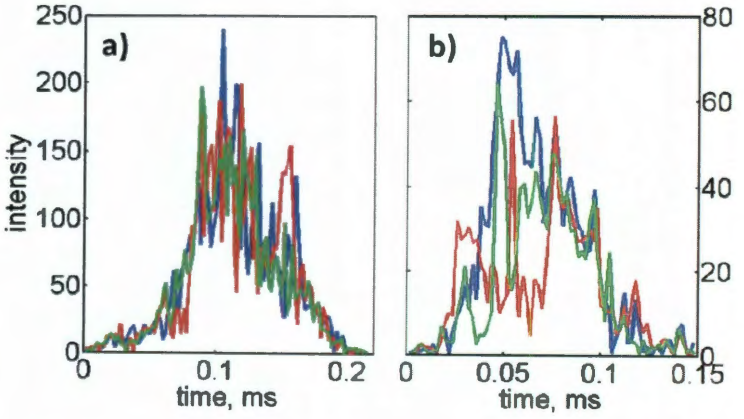

Figure 9.1: Trajectories of events generated by the random walk simulations. a) fast reorientation, b), slow reorientation.

Adjusting the values of OC and P_{thresh} allowed introduction of preferred orientations and rotational viscosity, respectively, for the dipoles in the sample volume. Part b of Figure 9.1, shows an event from a trajectory generated from a random walk with

$OC = 30$ and $P_{thresh} = 10$. The relative intensities on the three channels change only very slowly, reflecting very slow reorientation. Note that if either OC is set = 0 or P_{thresh} is set = 1, then dipoles rotate without an orientation preference: setting $P_{thresh} = 1$ corresponds physically to an absence of a barrier to thermally induced rotation, so that any impact will have enough energy to rotate the dipole, and setting $OC = 0$ corresponds to a uniform orientation preference across all angles.

Translational diffusion was executed using the random walk parameters established in section 9.3.[15] A translational step was taken at each time step, after rotation was executed. Upon completion of re-orientation and translation, intensity values at each time bin were calculated according to equation (9.3).[107]

Total intensity trajectories constructed for each particle trajectory were summed and saved at the end of the random walk, and actual sampled orientation trajectories in phi and theta were saved as well. The angle values and total intensity values were then used to compute measured intensity traces for the three detectors using equations (8.1) – (8.3).

Trajectories for data reported here were created from 5,000 runs of 10,000 steps. Data for each run was saved and the next run started from the orientation and position occupied by a dipole at the end of the previous run. Matlab's speed decreases as the number of steps/run increases, and by breaking the walk into multiple runs, larger data sets, and thus longer trajectories, could be acquired.

Post processing of the data by concatenating all the data files into one trace was executed, and these trajectories were then evaluated by the same analysis programs written to evaluate the experimental data.

CHAPTER 10

CONCLUSIONS AND FUTURE DIRECTIONS

10.1 Conclusions

The growth in global energy demand drives increased interest in new materials that can serve as the building blocks for effective electrochemical storage and conversion devices. Advancing ability to impose molecular level structural order in synthesized materials, and the new functional properties observed as a result of this structural order provides a new and powerful variable for development of effective devices. The rational design of the next stage of materials is already incorporating both chemically and structurally designed details, with the goal of tailored dynamics. This effort requires a detailed understanding of the heterogeneous processes contributing to the observed charge and mass transport characteristics of these molecularly ordered materials. With this in mind, this thesis work has focused on two fronts:

1) Providing a single molecule description of charge and mass transport in a class of ordered, structurally responsive polymer thin films known as polymer brushes; and
2) developing improved understanding of the strengths and practical limitations of established techniques along with further extending and developing single molecule experimental techniques.

With respect to the first goal, I have focused on the transport properties of strong polyelectrolyte thin-films, which have both charge transport and stimulus-responsive characteristics. The work of this thesis has demonstrated that FCS is able to clearly

resolve charge transport characteristics within strongly charged polymer brush thin films, and in Chapter 6, I further reported that while there are both charge-charge interactions and steric interactions occurring in the strong polyelectrolyte poly(styrene sulfonate) (PSS) brushes evaluated, it is the charge-charge interactions have a predominant impact on the diffusional dynamics. Furthermore, in Chapter 7, using polarization resolved spectroscopy, heterogeneous diffusion mechanisms were identified and quantified. Observed modes of diffusive transport included periods of significantly restricted rotational motion; periods of fast molecular rotation; and occasional adsorption of fluorescent probe molecules in the brush. The quantitative analysis of state occupation times provided the rate constants for transitions from weakly associated to strongly associated states. Generally, the results demonstrated the presence of dynamic, anisotropic interactions between the charged molecular probe and the polymer brush.

In Chapter 8, by employing 3-angle polarization resolved detection, it was possible to furthermore provide a 3-dimensional description of the transport occurring within the PSS brushes used in this work. The experiments, supported by simulations, revealed the existence of a global orientation parameter for transport within the films, tracked coherent dipole angle progressions over time, and identified a unique transport mechanism: translational diffusion with restricted orientation.

With respect to the second goal, both FCS and the 3-D orientation techniques were evaluated /developed for use to monitor transport characteristics of translating molecules in solvated polymer brush thin film environments. It is not a trivial matter to extract an accurate description of the multiple dynamic processes occurring in the heterogeneous brush systems using FCS. To clarify accurate use of FCS in this kind of

system, it was established in chapter 5 that, among other considerations addressed in the literature, appropriate limits for the analysis parameters used must be met. Specifically, minimum lag times (τ_{min}) need to be 2/3 or less the value of the shortest characteristic diffusion time reported. It was also established that in the case of multiple diffusing species not all of which are fully time resolved, the accuracy of the recovered diffusion constant for a fully time-resolved species is unaffected by the behavior of the autocorrelation function in the lag time region exhibiting decay due to a second non time-resolved species. This remains true in spite of the uncertainty in fitting that arises in this unresolved lag time region.

Analysis of rotational diffusion for translationally mobile molecules had not previously been evaluated using the relatively fast time resolution 3-detector method utilized in Chapter 8. This experimental method and meaningful data analysis was therefore developed and used to extract the information mentioned above, namely, the existence of a global orientation parameter for transport within the films, and the decoupling of rotational and translational diffusion in these thin films.

10.2 Future Directions

As evidenced by the current literature references cited throughout this thesis, the single molecule evaluation of transport in structurally ordered materials is of great current interest. Indeed, the work of this thesis has itself served to generate several new directions for investigation, a number of which will be pursued in the Landes lab.

10.2.1 Temperature Control

There are currently under development and analysis, experiments to investigate diffusion in temperature controlled samples. Preliminary results using molecules with varied charge identity and structure indicate it might be possible using FCS and temperature control to identify the existence of different molecular transport mechanisms for these varied molecules in the brush. The ability to apply a temperature *gradient* and evaluate transport using wide field techniques is also being developed.

10.2.2 Effect of Electric Fields on Electroactive Materials

As a means to explore the potentially switchable transport properties of electroactive polymer brush thin films, preliminary work has been conducted to develop interdigitated array electrodes on which polymer brush thin films are synthesized. Successful implementation of this technique would enable introduction of electric fields to the electroactive brush films and allow evaluation of changes in transport characteristics as a function of adjustable/switchable field strengths.

10.2.3 Bio-Membrane Studies Utilizing 3 Detector Method

Lipid bi-layer membranes share the ordered nature of polymer brush membranes, and the 3 Detector polarization resolved method discussed in Chapter 8 should therefore lend itself to the study of transport in these kinds of biological materials.

REFERENCES

(1) Mazurek, J. *Making Microchips: Policy, Globalization, and Economic Restructuring in the Semiconductor Industry*; MIT Press, 2003.

(2) Manthiram, A.; Murugan, V. A.; Sarkar, A.; Muraliganth, T. *Energ. Environ. Sci.* **2008**, *1*, 621.

(3) Simon, P.; Gogotsi, Y. *Nat. Mater.* **2008**, *7*, 845.

(4) Stuart, M. A. C.; Huck, W. T. S.; Genzer, J.; Muller, M.; Ober, C. K.; Stamm, M.; Sukhorukov, G. B.; Szleifer, I.; Tsurkruk, V. V.; Urban, M.; Winnik, F.; Zauscher, S.; Luzinov, I.; Minko, S. *Nat. Mater.* **2010**, *9*, 101.

(5) Zhou, F.; Huck, W. T. S. *Phys. Chem. Chem. Phys.* **2006**, *8*, 3815.

(6) Chang, W.-S.; Slaughter, L. S.; Khanal, B. P.; Manna, P.; Zubarev, E. R.; Link, S. *Nano Lett.* **2009**, *9*, 1152.

(7) Zrazhevskiy, P.; Sena, M.; Gao, X. H. *Chem. Soc. Rev.* **2010**, *39*, 4326.

(8) El-Ashry, M., Chair; al., e. *Renewables 2010 Global Status Report*, Renewable Energy Policy Network for the 21st Century, 2010.

(9) Verbruggen, A.; Marchohi, M. A. *Energy Policy* **2010**, *38*, 5572.

(10) Wilkinson, P. *Public Health* **2008**, *122*, 664.

(11) Kone, A. C.; Buke, T. *Renew. Sust. Energ. Rev.* **2010**, *14*, 2906.

(12) Solomon, S.; Qin, D.; Manning, M.; Chen, Z.; Marquis, M.; Averyt, K. B.; Tignor, M.; Miller, H. L. *Climate Change 2007: The Physical Science Basis*, Intergovernmental Panel on Climate Change, 2007.

(13) Bian, Z.; Dong, J.; Lei, S.; Leng, H.; Mu, S.; Wang, H. *Environ. Geol.* **2008**, *58*, 625.

(14) Earle, A. R.; Robert, E. *Environmental effects of mining*; St. Lucie Press, 1996.

(15) Tcherniak, A.; Reznik, C.; Link, S.; Landes, C. *Anal. Chem.* **2009**, *81*, 746.

(16) Reznik, C.; Darugar, Q.; Wheat, A.; Fulghum, T.; Advincula, R. C.; Landes, C. *J. Phys. Chem. B* **2008**, *112*, 10890.

(17) Reznik, C.; Estillore, N.; Advincula, R. C.; Landes, C. F. *J. Phys. Chem. B* **2009**, *113*, 14611.

(18) Saxena, A.; Tripathi, B. P.; Shahi, V. K. *J. Phys. Chem. B.* **2007**, *111*, 12454.

(19) Zhou, F.; Zheng, Z.; Yu, B.; Liu, W.; Huck, W. T. S. *J. Am. Chem. Soc.* **2006**, *128*, 16253.

(20) Jagannathan, K.; Sung, B. J.; Yethiraj, A. *Phys. Rev. Lett.* **2006**, *97*, 145503.

(21) Jacobsen, M. Z.; Colella, W. G.; Golden, D. M. *Science* **2005**, *308*, 1901.

(22) Schultz, M. G.; Diehl, T.; P., B. G.; Zittel, W. *Science* **2003**, *302*, 624.

(23) Teki, R.; Datta, M. K.; Krishnan, R.; Parker, T. C.; Lu, T.-M.; Kumta, P. N.; Nikhil, K. *Small* **2009**, *5*, 2236.

(24) Pech, D.; Brunet, M.; Durou, H.; Huang, P.; Mochalin, V.; Gogotsi, Y.; Taberna., P. L.; Simon, P. *Nat. NanoTech.* **2010**, *18*, 3168.

(25) Rudge, A.; Davey, J.; Raistrick, I.; Gottesfeld, S. *J. Power Sources* **1993**, *47*, 89.

(26) Wautersen, S.; Bakker, H. *Phys. Rev. Lett.* **2006**, *96*, 138305.

(27) Choe, Y.-K.; Tsuchida, E.; Ikeshoji, T.; Yamakawa, S.; Hyodo, S.-a. *J. Phys. Chem. B* **2008**, *112*, 11586.

(28) Norsten, T. B.; Guiver, M. D.; Murphy, J.; Astill, T.; Navessin, T.; Holdcroft, S.; Frankamp, B. L.; Rotello, V. M.; Ding, J. *Adv. Funct. Mater.* **2006**, *16*, 1814.

(29) Schmidt-Rohr, K.; Chen, Q. *Nat. Mater.* **2008**, *7*, 75.

(30) Pagliaro, M.; Ciriminna, R. *J. Mater. Chem.* **2005**, *15*, 4981.

(31) Pharoah, J. G.; Karan, K.; Sun, W. *J. Power Sources* **2006**, *161*, 214.

(32) Chen, S.; Krishnan, L.; S., S.; Benziger, J.; Bocarsly, A. B. *J. Membrane Sci.* **2004**, *243*, 327.

(33) Huang, X.; Solasi, R.; Zou, Y.; Feshler, M.; Reifsnider, K.; Condit, D.; Burlatsky, S.; Medden, T. *Journal of Polymer Science, Part B: Polymer Physics* **2006**, *44*, 2346.

(34) Ho, P. K. H.; Kim, J.-S.; Burroughes, J. H.; Becker, H.; Sam, F. Y. L.; Brown, T. M.; Cacialli, F.; Friend, R. H. *Nature* **2000**, *404*, 481.

(35) Wang, B.; Anthony, S. M.; Bae, S. C.; Granick, S. *Proc. Natl. Acad. Sci.* **2009**, *106*, 15160.

(36) Kirstein, J.; Platschek, B.; Jung, C.; Brown, R.; Bein, T.; Brauchle, C. *Nat. Mater.* **2007**, *6*, 303.

(37) Jung, C.; Hellriegel, C.; Platschek, B.; Wohrle, D.; Bein, T.; Michaelis, J.; Brauchle, C. *J. Am. Chem. Soc.* **2007**, *129*, 5570.

(38) Branden, M.; Sanden, T.; Brzezinski, P.; Widengren, J. *Proc. Natl. Acad. Sci. U.S.A.* **2006**, *103*, 19766.

(39) Modesti, G.; Zimmermann, B.; Borsch, M.; Herrmann, A.; Saalwachter, K. *Macromolecules* **2009**, *42*, 4681.

(40) Argun, A. A.; Ashcraft, N. J.; Hammond, P. T. *Adv. Mater.* **2008**, *20*, 1539.

(41) Advincula, R. C.; Brittain, W. J.; Baster, K. C.; Ruhe, J. *Polymer Brushes: Synthesis, Characterization, Applications*; Wiley, 2004.

(42) Whiting, G. L.; Snaith, H. J.; Khodabakhsh, S.; Andreasen, J. W.; Breiby, D. W.; Nielsen, M. M.; Greenham, N. C.; Friend, R. H.; Huck, W. T. S. *Nano Lett.* **2006**, *6*, 573.

(43) Bittrich, E.; Kuntzsch, M.; Eichhorn, K.-J.; Uhlmann, P. *J. Polym. Sci.* **2009**, *48*, 1606.

(44) Wang, S.; Chang, H.-C.; Zhu, Y. *Macromolecules* **2010**, *43*, 7402.

(45) Liu, X.; Ye, Q.; Yu, B.; Liang, Y.; Liu, W.; Zhou, F. *Langmuir* **2010**, *26*, 12377.

(46) Moerner, W. E.; Fromm, D. P. *Review of Scientific Instruments* **2003**, *74*, 3597.

(47) Kulzer, F.; Orrit, M. *Annu. Rev. Phys. Chem.* **2004**, *55*, 585.

(48) Xu, W.; Kong, J. S.; Yeh, Y.-T. E.; Chen, P. *Nat. Mater.* **2008**, *7*, 992.

(49) Ha, T.; Ting, A. Y.; Liang, J.; Caldwell, W. B.; Deniz, A. A.; Chemla, D. S.; Schultz, P. G.; Weiss, S. *Proc. Natl. Acad. Sci. USA* **1999**, *96*, 893.

(50) Weiss, S. *Nat. Struct. Biol.* **2000**, *7*, 724.

(51) Woll, D.; Braeken, E.; Deres, A.; DeSchryver, F.; Uji-i, H.; Hofkens, J. *Chem. Soc. Rev.* **2009**, *38*, 313.

(52) Moerner, W. E. *Proc. Natl. Acad. Sci.* **2007**, *104*, 12596.

(53) Schuler, B.; Lipman, E. A.; Steinbach, P. J.; Kumke, M.; Eaton, W. A. *Proc. Natl. Acad. Sci. USA* **2005**, *102*, 2754.

(54) Cosa, G.; Zeng, Y.; Liu, H.-W.; Landes, C. F.; Makarov, D. E.; Musier-Forsyth, K.; Barbara, P. F. *J. Phys. Chem. B.* **2006**, *110*, 2419.

(55) Jung, C.; Kirstein, J.; Platschek, B.; Bein, T.; Budde, M.; Frank, I.; Mullen, K.; Michaelis, J.; Brauchle, C. *J. Am. Chem. Soc.* **2008**, *130*, 1638.

(56) Zondervan, R.; Kulzer, F.; Berkhout, G. C. G.; Orrit, M. *Proc. Natl. Acad. Sci. U.S.A.* **2007**, *104*, 12628.

(57) Dieterich, D. C.; Hodas, J. J. L.; Gouzer, G.; Shadrin, I. Y.; Ngo, J. T.; Triller, A.; Tirrell, D. A.; Schuman, E. M. *Nat. Neurosci.* **2010**, *13*, 897.

(58) Kulzer, F.; Xia, T.; Orrit, M. *Single Mol.* **2010**, *49*, 854.

(59) Reznik, C.; Estillore, N.; Advincula, R. C.; Landes, C. F. *J. Phys. Chem. B* **2010**, *113*, 14611.

(60) Sanabria, H.; Kubota, Y.; Waxham, M. N. *Biophys. J.* **2007**, *92*, 313.

(61) Wawrezinieck, L.; Rigneault, H.; Marguet, D.; Lenne, P.-F. *Biophysical Journal* **2005**, *89*, 4029.

(62) Burgos, P.; Zhang, Z.; Golestanian, R.; Leggett, G. J.; Geoghegan, M. *ACS Nano* **2009**, *3*, 3235.

(63) Elson, E. L.; Madge, D. *Biopolymers* **1974**, *13*, 1.

(64) Haustein, E.; Schwille, P. *Methods* **2003**, *29*, 153.

(65) Wirth, M.; Ludes, M.; Swinton, D. *Appl. Spectrosc.* **2001**, *55*, 663.

(66) de Santo, I.; Causa, F.; Netti, P. A. *Anal Chem* **2010**, *82*, 997.

(67) Ries, J.; Yu, S. R.; Burkhardt, M.; Brand, M.; Schwille, P. *Nature Methods* **2009**, *6*, 643.

(68) Wohland, T.; Shi, X.; Snankaran, J.; Stelzer, E. H. K. *Opt. Express* **2010**, *18*, 110627.

(69) Haustein, E.; Schwille, P. *Annu. Rev. Biophys. Biomol.* **2007**, *36*, 151.

(70) Dertinger, T.; Pacheco, V.; von der Hocht, I.; Hartmann, R.; Gregor, I.; Enderlein, J. *ChemPhysChem* **2007**, *8*, 433.

(71) Ries, J.; Bayer, M.; Csucs, G.; Dirkx, R.; Solimena, M.; Ewers, H.; Schwille, P. *Opt. Express* **2010**, *18*, 11073.

(72) Persson, G.; Thyberg, P.; Sanden, T.; Widengren, J. *J. Phys. Chem. B* **2009**, *113*, 8752.

(73) Wennmalm, S.; Thyberg, P.; Widengren, J. *Anal. Chem.* **2009**, *81*, 9209.

(74) Gennerich, A.; Schild, D. *Biophys. J.* **2000**, *79*, 3294.

(75) Ries, J.; Chiantia, S.; Schwille, P. *Biophys. J.* **2009**, *96*, 1999.

(76) Kim, S. A.; Heinze, K. G.; Schwille, P. *Nature Methods* **2007**, *4*, 963.

(77) Cherdhirankorn, T.; Harmandaris, V.; Juhari, A.; Voudouris, P.; Fytas, G.; Kremer, K.; Koynov, K. *Macromolecules* **2009**, *42*, 4858.

(78) Yameen, B.; Ali, M.; Neumann, R.; Ensinger, W.; Knoll, W.; Azzaroni, O. *Chem. Comm.* **2010**, *46*, 1908.

(79) Daiguji, H.; Adachi, T.; Tatsumi, N. *Phys. Rev. E.* **2008**, *78*, 026301.

(80) Lakowicz, J. R. *Principles of Fluorescence Spectroscopy*; Third ed.; Springer: Baltimore, MD, 2006.

(81) Schob, A.; Cichos, F.; Schuster, J.; von Borczyskowski, C. *Eur. Polymer J.* **2004**, *40*, 1019.

(82) Advincula, R. C. *Polymer brushes : synthesis, characterization, applications* 2006 ed.; Weinheim : Wiley-VCH, 2004.

(83) Prucker, O.; Ruhe, J. *Macromolecules* **1998**, *31*, 602.

(84) Prucker, O.; Ruhe, J. *Langmuir* **1998**, *14*, 6839.

(85) Limpoco, F. T.; Advincula, R.; Perry, S. S. *Langmuir* **2007**, *23*, 12196.

(86) Chen, Z.; Tang, Y.-J.; Xie, T.-T.; Chen, Y.; Li, Y.-Q. *J. Fluoresc.* **2008**, *18*, 93.

(87) Paschotta, R. 2010; Vol. 2010.

(88) Hess, S. T.; Webb, W. W. *Biophys. J.* **2002**, *83*, 2300.

(89) Marrocco, M. *Chemical Physics Letters* **2007**, *449*, 227.

(90) Ries, J.; Schwille, P. *Phys. Chem. Chem. Phys.* **2008**, *10*, 3487.

(91) Benda, A.; Benes, M.; Marecek, V.; Lhotsky, A.; Hermens, W. T.; Hof, M. *Langmuir* **2003**, *19*, 4120.

(92) Koppel, D. E.; Axelrod, D.; Schlessinger, J.; Elson, E. L.; Webb, W. W. *Biophys. J.* **1976**, *16*, 1315.

(93) Hecht, E. *Optics*; 4th ed.; Pearson Education, Inc., 2002.

(94) Adkins, E. M.; Samuvel, D. J.; Fog, J. U.; Eriksen, J.; Jayanthi, L. D.; Bjerggaard Vaegter, C.; Ramamoorthy, S.; Gether, U. *Biochemistry* **2007**, *46*, 10484.

(95) Dauty, E.; Verkman, A. S. *J. Mol. Recognit.* **2004**, *17*, 441.

(96) Posokhov, Y. O.; Rodnin, M. V.; Lu, L.; Ladokhin, A. S. *Biochemistry* **2008**, *47*, 5078.

(97) Braenden, M.; Sanden, T.; Brzezinski, P.; Widengren, J. *Proc. Natl. Acad. Sci.* **2006**, *103*, 19766.

(98) Gennerich, A.; Schild, D. *Biophys. J.* **2002**, *83*, 510.

(99) Gosch, M.; Blom, H.; Holm, J.; Heino, T.; Rigler, R. *Anal. Chem.* **2000**, *72*, 3260.

(100) Foquet, M.; Korlach, J.; Zipfel, W. R.; Webb, W. W.; Craighead, H. G. *Anal. Chem.* **2004**, *76*, 1618.

(101) Grabowski, C. A.; Mukhopadhyay, A. *J. Chem. Phys.* **2007**, *127*, 171101/1.

(102) Schuster, J.; Cichos, F.; Wrachtrup, J.; Von Borczyskowski, C. *Single Mol.* **2000**, *1*, 299.

(103) Wang, W.; Zhang, C.; Wang, S.; Zhao, J. *Macromolecules* **2007**, *40*, 9564.

(104) Enderlein, J.; Gregor, I.; Patra, D.; Dertinger, T.; Kaupp, U. B. *ChemPhysChem* **2005**, *6*, 2324.

(105) Enderlein, J.; Gregor, I.; Patra, D.; Fitter, J. *Curr. Pharm. Biotechnol.* **2004**, *5*, 155.

(106) Rigler, R.; Mets, U.; Widengren, J.; Kask, P. *Eur. Biophys. J.* **1993**, *22*, 169.

(107) Aragon, S.; Pecora, R. *J. Chem. Phys.* **1976**, *64*, 1791.

(108) Wohland, T.; Rigler, R.; Vogel, H. *Biophys. J.* **2001**, *80*, 2987.

(109) Meseth, U.; Wohland, T.; Rigler, R.; Vogel, H. *Biophys. J.* **1999**, *76*, 1619.

(110) Gell, C.; Brockwell, D. J.; Beddard, G. S.; Radford, S. E.; Kalverda, A. P.; Smith, D. A. *Single Mol.* **2001**, *2*, 177.

(111) Wei, C.-Y. J.; Lu, C.-Y.; Kim Yeon, H.; Vanden Bout David, A. *J. Fluoresc.* **2007**, *17*, 797.

(112) Lu, C.-Y.; Vanden Bout, D. *J. Chem. Phys.* **2006**, *125*, 124701.

(113) Magatti, D.; Ferri, F. *Appl. Opt.* **2001**, *40*, 4011.

(114) Wahl, M.; Gregor, I.; Patting, M.; Enderlein, J. *Opt. Express* **2003**, *11*, 3583.

(115) Coriell, S. R.; Jackson, J. L. *J. Chem. Phys.* **1963**, *39*, 2418.

(116) Magde, D.; Elson, E. L.; Webb, W. W. *Biopolymers* **1974**, *13*, 29.

(117) Culbertson, M. J.; Williams, J. T. B.; Cheng, W. W. L.; Stults, D. A.; Wiebracht, E. R.; Kasianowicz, J. J.; Burden, D. L. *Anal. Chem.* **2007**, *79*, 4031.

(118) Nie, S.; Chiu, D. T.; Zare, R. N. *Anal. Chem.* **1995**, *67*, 2849.

(119) Biesheuvel, P. M. *Journal of Colloid and Interface Science* **2004**, *275*, 97.

(120) Kumar, N. A.; Seidel, C. *Macromolecules* **2005**, *38*, 9341.

(121) Ahrens, H.; Forster, S.; Helm, C. A. *Phys. Rev. Lett.* **1998**, *81*, 4172.

(122) Pristinski, D.; Kozlovskaya, V.; Sukhishvili, S. A. *J. Chem. Phys.* **2005**, *122*, 014907/1.

(123) Zhou, F.; Huck, W. T. S. *Phys. Chem. Chem. Phys.* **2006**, *8*, 3815.

(124) Cayre, O. J.; Chang, S. T.; Velev, O. D. *J. Am. Chem. Soc.* **2007**, *129*, 10801.

(125) Banerjee, S.; Curtin, D. E. *J. Fluorine Chem.* **2004**, *125*, 1211.

(126) Choi, E.-Y.; Azzaroni, O.; Cheng, N.; Zhou, F.; Kelby, T.; Huck, W. T. S. *Langmuir* **2007**, *23*, 10389.

(127) Milner, S. T. *Science* **1991**, *251*, 905.

(128) Pincus, P. *Macromolecules* **1991**, *24*, 2912.

(129) Fytas, G.; Anastasiadis, S.; Seghrouchni, R.; Vlassopoulos, D.; Li, J.; Factor, B.; Theobald, W.; Toprakcioglu, C. *Science* **1996**, *274*, 2041.

(130) Filippidi, E.; Michailidou, V.; Loppinet, B.; Ruehe, J.; Fytas, G. *Langmuir* **2007**, *23*, 5139.

(131) Michailidou, V. N.; Loppinet, B.; Prucker, O.; Ruehe, J.; Fytas, G. *Macromolecules* **2005**, *38*, 8960.

(132) Hunter, C. A.; Sanders, J. K. M. *J. Am. Chem. Soc.* **1990**, *112*, 5525.

(133) Lu, C. Y.; Vanden Bout, D. A. *J. Chem. Phys.* **2006**, *125*, 124701.

(134) Mohanty, P. S.; Harada, T.; Matsumoto, K.; Matsuoka, H. *Macromolecules* **2006**, *39*, 2016.

(135) Mao, Z.; Ma, L.; Gao, C.; Shen, J. *J. Control. Release* **2005**, *104*, 193.

(136) Kaewsaiha, P.; Matsumoto, K.; Matsuoka, H. *Langmuir* **2007**, *23*, 7065.

(137) Lifson, S.; Jackson, J. L. *J. Chem. Phys.* **1962**, *36*, 2410.

(138) Adelroth, P.; Brzezinski, P. *Biochim. Biophys. Acta* **2004**, *1655*, 102.

(139) Braenden, M.; Sanden, T.; Brzezinski, P.; Widengren, J. *Proc. Natl. Acad. Sci. U.S.A.* **2006**, *103*, 19766.

(140) Eikerling, M.; Kornyshev, A. A.; Kuznetsov, A. M.; Ulstrup, J.; Walbran, S. *J. Phys. Chem. B.* **2001**, *105*, 3646.

(141) Liao, K.-S.; Fu, H.; Wan, A.; Batteas, J. D.; Bergbreiter, D. *Langmuir* **2009**, *25*, 26.

(142) Sung, B. J.; Yethiraj, A. *Phys. Rev. Lett.* **2006**, *96*, 228103.1.

(143) Fu, G. D.; Xu, L. Q.; Yao, F.; Zhang, K.; Wang, X. F.; Zhu, M. F.; Nie, S. Z. *Appl. Mater. Interfaces* **2009**, *1*, 239.

(144) Ionov, L.; Bocharova, V.; Diez, S. *Soft Matter* **2009**, *5*, 67.

(145) Yamamoto, S.-i.; Pietrasik, J.; Matyjaszewski, K. *Macromolecules* **2008**, *41*, 7013.

(146) Fulghum, T.; Taranekar, P.; Advincula, R. *Macromolecules* **2008**, *41*, 5681.

(147) Zhulina, E. B.; Birshtein, T. M.; Borisov, O. V. *Macromolecules* **1995**, *28*, 1491.

(148) Kitano, H.; Kago, H.; Matsuura, K. *J. Colloid Interf. Sci.* **2009**, *331*, 343.

(149) Bartko, A.; Xu, K.; Dickson, R. M. *Phys. Rev. Lett.* **2002**, *89*, 026101.

(150) Gelin, M. F.; Kosov, D. S. *J. Chem. Phys.* **2006**, *125*, 054708.

(151) Ha, T.; Laurence, T. A.; Chemla, D.; Weiss, S. *J. Phys. Chem. B.* **1999**, *103*, 6839.

(152) Fourkas, J. T. *Opt. Lett.* **2001**, *26*, 211.

(153) Gilliland, J. W.; Yokoyama, K.; Yip, W. T. *Chem. Mater.* **2004**, *16*, 3949.

(154) Dedecker, P.; Muls, B.; Deres, A.; Uji-i, H.; Hotta, J.-i.; Sliwa, M.; Soumillion, J.-P.; Mullen, K.; Enderlein, J.; Hofkens, J. *Adv. Mater.* **2009**, *21*, 1079.

(155) Uji-i, H.; Melnikov, S. M.; Deres, A.; Bergamini, G.; DeSchryver, F.; Herrmann, A.; Mullen, K.; Enderlein, J.; Hofkens, J. *Polymer* **2006**, *47*, 2511.

(156) Macklin, J. J.; Trautman, J. K.; Harris, T. D.; Brus, L. E. *Science* **1996**, *272*, 255.

(157) Lebold, T.; Muhlstein, L. A.; Blechinger, J.; Riederer, M.; Amenitsch, H.; Kohn, R.; Peneva, K.; Mullen, K.; Michaelis, J.; Brauchle, C.; Bein, T. *Chem. Eur. J.* **2009**, *15*, 1661.

(158) Deniz, A. A.; Laurence, T. A.; Dahan, M.; Chemla, D. S.; Schultz, P. G.; Weiss, S. *Annu. Rev. Phys. Chem.* **2001**, *52*, 233.

(159) Dahan, M.; Deniz, A.; Ha, T.; Chemla, D.; Schultz, P.; Weiss, S. *Chem. Phys.* **1999**, *247*, 85.

(160) Hinze, G.; Diezemann, G.; Basche, T. *Phys. Rev. Lett.* **2004**, *93*, 203001.

(161) Axelrod, D. *Biophys. J.* **1979**, *78*, 557.

(162) Forkey, J. N.; Quinlan, M. E.; Goldman, Y. E. *Prog. Biophys. Mol. Biol.* **2000**, *74*, 1.

(163) Wei, C.-Y. J.; Vanden Bout, D. *J. Phys. Chem. B* **2009**, *113*, 2253.

(164) Wei, C.-Y. J.; Kim, Y. H.; Darst, R. K.; Rossky, P. J.; Vanden Bout, D. A. *Phys. Rev. Lett.* **2005**, *95*, 173001/1.

(165) Osborne, M. A.; Balasubramanian, S.; Furey, W. S.; Klenerman, D. *J. Phys. Chem. B.* **1998**, *102*, 3160.

(166) Spears, K. G. *Rotational Dynamics of Small and Macromolecules: Rotation of large molecular ions and transient dielectric relaxation effects*; Springer-Verlag, 1987; Vol. 293.

(167) Wiemers, K.; Kauffman, J. F. *J. Phys. Chem. A.* **2000**, *104*, 451.

(168) Schoch, R. B.; Han, J.; Renaud, P. *Rev. Mod. Phys.* **2008**, *80*, 839.

(169) Nahas, M.; Wilson, T.; Hohng, S.; Jarvie, K.; Lilley, D. M. J.; Ha, T. *Nat. Struct. Mol. Biol.* **2004**, *11*, 1107.

(170) Shi, J.; Palfey, B.; Dertouzos, J.; Jensen, K.; Gafni, A.; Steel, D. *J. Am. Chem. Soc.* **2004**, *126*, 6914.

(171) Slota, J.; He, X.; Huck, W. T. S. *nanoToday* **2010**, *5*, 231.

(172) Bureekaew, S.; Horike, S.; Higuchi, M.; Mizuno, M.; Kawamura, T.; Tanak, D.; Yanai, N.; Kitagawa, S. *Nat. Mater.* **2009**, *8*, 831.

(173) Hohlbein, J.; Hubner, C. G. *J. Chem. Phys.* **2008**, *129*, 094703.

(174) Lu, C.-Y.; Vanden Bout David, A. *J. Chem. Phys.* **2008**, *128*, 244501.

(175) Adhikari, A. N.; Capurso, N. A.; Bingemann, D. *J. Chem. Phys.* **2007**, *127*, 114508.

(176) Doliwa, B.; Heuer, A. *Phys. Rev. E.* **2003**, *67*, 030501.

(177) Blackburn, F. R.; Wang, C.-Y.; Ediger, M. D. *J. Phys. Chem.* **1996**, *100*, 18249.

(178) Lu, H. P.; Xun, L.; Xie, S. *Science* **1998**, *282*.

(179) Saffman, P. G.; Delbruck, M. *Proc. Natl. Acad. Sci.* **1975**, *72*, 3111.

(180) Landau, L. D.; Lifshitz, E. M. *Fluid Mechanics, Second Edition*; Second ed.; Reed Educational and Professional Publishing, Ltd, 2000; Vol. 6.